UNIVERSITÄT PADERBORN
Die Universität der Informationsgesellschaft

FAKULTÄT FÜR
ELEKTROTECHNIK,
INFORMATIK UND
MATHEMATIK

Low Pressure Chemical Vapor Deposition of Silicon Nitride and Silicon Oxynitride Layers and their Application in Optical Waveguide based Chemical Sensors

Zur Erlangung des akademischen Grades

DOKTORINGENIEUR (Dr.-Ing.)

der Fakultät für Elektrotechnik, Informatik und Mathematik
der Universität Paderborn
genehmigte Dissertation
von

M.-Eng. Ahmed Tamim
Paderborn

Referent: Prof. Dr.-Ing. U. Hilleringmann
Korreferent: apl. Prof. Dr. rer. nat. Reinhart Job

Tag der mündlichen Prüfung: 24.08.2007

Paderborn, den 05.09.2007

Diss. EIM-E/SEN

UNIVERSITÄT PADERBORN
Die Universität der Informationsgesellschaft

FAKULTÄT FÜR
ELEKTROTECHNIK,
INFORMATIK UND
MATHEMATIK

Low Pressure Chemical Vapor Deposition of Silicon Nitride and Silicon Oxynitride Layers and their Application in Optical Waveguide based Chemical Sensors

A Thesis Submitted to the Faculty of Electrical Engineering, Computer Science and Mathematics – University of Paderborn in Partially Fulfillment of the Requirements for the Degree of

Doctor-Engineer (Dr.-Eng)

In

Electrical Engineering

By

M.-Eng. Ahmed Tamim

Reviewers:

Prof. Dr.-Eng. Ulrich Hilleringmann

apl. Prof. Dr. rer. nat. Reinhart Job

Date of Thesis Submission: 30.05.2007

Date of Defence Examination: 24.08.2007

Paderborn, Germany

Acknowledgement

I would like to express my deepest gratitude towards my supervisor Prof. Dr.-Eng. Ulrich Hilleringmann, for his guidance, moral support, assistance and encouragement during my study here in Paderborn.

I would also like to thank apl. Prof. Dr. rer. nat. Reinhart Job for acting as second reviewer, and Prof. Dr. techn. F. Gausch, Prof. Dr.-Eng. R. Noe, Prof. Dr.-Eng. U. Rückert and Prof. Dr.-Eng. A. Thiede for being in my examination committee.

I would also like to thank also Dr.-Eng. Christoph Pannemann and all my colleagues in sensor technology department for their help and friendship.

Finally I would like to thank my parents, my wife, my children and my brothers.

Abstract

This work involves optimization and characterization of low pressure chemical vapour deposition (LPCVD) of silicon nitride and silicon oxynitride layers. The optimized parameters of this deposition were used in fabricating the guiding layer of an optical Mach-Zehnder interferometer which was used as a transducer for a waveguide based sensor used to detect chemical gases such as ammonia. In this sensor a titanium heater with aluminium contacts was integrated near to the reference arm in order to increase the sensitivity of the sensor by using the thermo-optical effect. A chemo-optical sensitive material to ammonia (its refractive index changes with changing the amount of ammonia that diffuses into it from the ambient air) was spin coated on a sensing window in the sensing arm.

The work in this thesis is split into three main areas of study. The first is designing a monomode silicon oxynitride waveguide using the imaginary distance beam propagation method (ID-BPM), also a design of waveguide parameters which increase the sensitivity, designing the Mach-Zehnder interferometer and the heater. The masks for the whole structure were designed using the Cadence program.

In the second area, LPCVD of silicon nitride and silicon oxynitride films were optimized by the adjustment of the deposition temperature and the gases flow rate. The homogeneity of the deposited layers, the deposition rate and the thickness variations along the wafers and the boats were discussed.

In the third area, the detailed fabrication procedures of the sensor are discussed including several important standard processes such as the thermal oxidation of the silicon substrate, the low pressure chemical vapour deposition (LPCVD), the photolithography for mask transfer, the reactive ion etching for a ridge waveguide formation, the metal evaporation and wet etching. Also the characterizations of the sensor were carried out. The waveguide was analyzed to make sure that the sensor is working as expected. The heater also was tested to see how much dissipated power the resistor can withstand during its heating, the heating effect on its resistance and the heating effect on the transmission intensity were checked too. Finally, the refractive index change in the sensitive layer during exposure to ammonia was measured. Also the sensor response, the response time and sensitivity of the sensor were discussed.

Zusammenfassung

In dieser Arbeit wurden die Abscheidung von Siliziumnitrid Und Siliziumoxynitridfilmen nach dem Low Pressure Chemical Vapor Deposition (LPCVD)-Verfahren zur Integration eines optischen Gassensors optimiert und die resultierenden Schichten optisch charakterisiert. Mit den gewonnenen Abscheideparametern wurden die Wellenleiter eines Mach-Zehnder-Interferometers hergestellt, das als Signaltransformator in einem Ammoniaksensor dient. Dieser Sensor nutzt ein Heizelement aus Titan mit Aluminiumkontakten, integriert neben dem Referenzarm, um die Empfindlichkeit des Interferometers durch Ausnutzung des thermo-optischen Effekts auf das Maximum abzugleichen. Ein chemo-optisch mit Ammoniak reagierendes Material wurde im Spincoating-Verfahren auf die Sensorfläche im Messzweig aufgetragen.

Im ersten Teil dieser Arbeit wurde ein Monomode-Siliziumoxynitrid-Wellenleiter mit der Imaginary-Distance-Beam-Propagation-Methode (ID-BPM) entworfen. Die Wellenleiterparameter wurden entsprechend gewählt, um das Mach-Zehnder-Interferometer mit dem Heizelement zu optimieren. Die Masken für die vollständige Struktur wurden mit dem Programm Cadence entworfen. Im zweiten Teil wurde die Abscheidung von Siliziumnitrid und Siliziumoxynitrid im LPCVD-Verfahren anhand von 45 Testwafern bezüglich der Abscheidetemperatur und der Gasströmungsgeschwindigkeit optimiert. Die Homogenität der abgeschiedenen Schichten, die Abscheiderate und die Schichtdickenvariationen wurden untersucht. Im dritten Teil wurde die Herstellung des Sensors einschließlich der wichtigsten Prozessschritte behandelt. Ebenso wurden die Wellenleiter sowie der gesamte Sensor charakterisiert. Der Heizer wurde hinsichtlich der maximal zulässigen Leistung analysiert, insbesondere die Auswirkung der Erwärmung auf den elektrischen Widerstand getestet. Schließlich wurde die Änderung des Brechungsindexes in der empfindlichen Schicht in Abhängigkeit von der Ammoniakkonzentration bestimmt. Ebenso wurden das Sensorübertragungsverhalten, die Ansprechzeit und die Empfindlichkeit des Sensors untersucht.

Contents

Introduction

The main goal of this thesis work is the optimization of LPCVD to find the deposition parameters such as deposition temperature, deposition pressure and gases flow rate which will be used in fabricating the guiding layer of the MZI waveguide. This layer will be used to verify the design requirements such as refractive index value, thickness and optical properties which will make the designed waveguide monomode and will result in high surface sensitivity. This waveguide will be used as a transducer for a waveguide based sensor used to detect chemical gases such as ammonia. In this sensor a titanium heater with aluminium contacts will be integrated near to the reference arm of the MZI in order to increase the sensitivity of the sensor by using the thermo-optical effect. For ammonia sensing a chemo-optical material sensitive to ammonia will be placed at a sensing window in the sensing arm. The processing facilities in our research laboratory were employed throughout the study. This thesis is consisting of five chapters;

Chapter one includes background on silicon technology, low pressure chemical vapor deposition, the optical guiding materials such as silicon nitride and silicon oxynitride, the optical waveguides and chemical sensors.

Chapter two concerns the sensor design including the design of the waveguide in order to verify two conditions: it has to be monomode and it should show a high surface sensitivity. It explains the design of the Mach-Zehnder interferometer and the design of the heater.

In chapter three the optimization of low pressure chemical vapor deposition for silicon nitride and silicon oxynitride is presented. The gases flow rate, the deposition temperature, the thickness variation along the wafers, the deposition rate and the homogeneity of the deposited layers were discussed.

Chapter four describes the process steps applied in the fabrication of the silicon oxynitride waveguide based ammonia sensor and the characteristics of the sensor such as total losses, light modulation and ammonia sensing.

Finally, in chapter five the conclusions that are drawn from this study are presented.

1 Processing of waveguide sensors

1.1 Silicon technology

Silicon technology still remains the most dominant force in electronic integrated circuits and it seems that it will continue in the near future. The work towards implementation of silicon technology in the integrated optics area started ever since the notion of integrated optics was introduced. There are several key factors for this application to be successful. First of all, any candidate technology must provide waveguide structures with low propagation losses. Moreover, it should be compatible with microelectronics device processing and provide a high reproducibility at reasonably low cost. The coupling between optical integrated circuits (OIC) and other elements such as optical waveguides, light sources, and photodetectors is another important issue of consideration. Si-based technologies offer crucial advantages on all these points, which make it more attractive than other competing technologies.

In order to look for silicon compatible materials, one of the requirements is the availability of thin dielectric films with a large refractive index difference between the core material and the cladding material. In fact, the device size scales down with increasing the refractive index difference. Unfortunately, it is quite difficult to achieve low propagation losses for large refractive index differences and the scattering losses increase as the square of the refractive index difference, and therefore high index core waveguides are very sensitive to interface roughness. A second requirement on the materials is the compatibility with the conventional silicon technology. The materials have to withstand the process conditions such as purity, temperature, compatibility, stability, functionality and should be processable with the tools already common in the microelectronics industry. Low pressure chemical vapor deposition (LPCVD) is a very important process for silicon technology.

1.2 Low pressure chemical vapor deposition (LPCVD)

Chemical vapor deposition (CVD) is defined as the formation of a non-volatile solid film on a substrate by the reaction of vapor phase chemicals (reactants) that contain the required constituents.

A CVD process can be summarized as consisting of the following sequence of steps:

- A given composition (and flow rate) of reactant gases is introduced into a reactant chamber
- The gas species move to the substrate
- The reactants are absorbed on the substrate

- The atoms undergo migration and film-forming chemical reactions
- The gaseous by products of the reaction are desorbed and removed from the reaction chamber

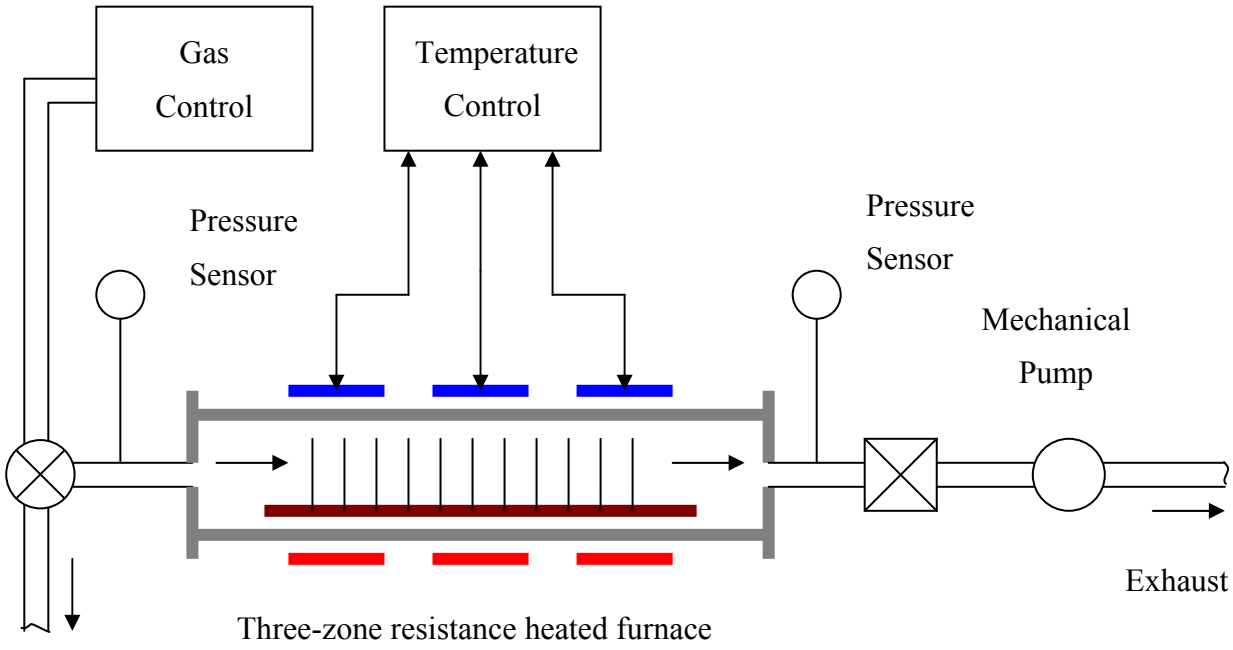

Figure (1-1): Block diagram of a low pressure chemical vapor deposition system

LPCVD can be used for deposition of silicon nitride (Si_3N_4) and silicon oxynitride (SiON). The low pressure chemical vapor deposition (LPCVD) process shown in figure (1-1) deposits the films at relatively high temperatures and low pressures and depends upon four critical parameters which are the total flow rate of the gasses, gas ratio of ammonia (NH_3), oxygen (O_2) and triethylsilane ($C_6H_{16}Si$), chamber pressure and chamber temperature. The most significant factor in the (LPCVD) silicon nitride furnace is the gas ratio. By modifying the ratio at which gases enter the gas chamber one can drastically change the film properties obtained at a specified point within the chamber. By increasing the amount of ammonia that is in the chamber, the film stress becomes increasingly tensile, whereas, by a decrease of the amount of ammonia in the chamber the stress of the film becomes increasingly compressive. By balancing these two extremes, one can create a point in the chamber that closely approximates zero stress.

The second significant factor in a LPCVD silicon nitride furnace is the chamber pressure. By increasing the pressure of the chamber, the extent of the reaction is not allowed to move too far down the chamber (towards the vacuum). Hence by increasing the pressure of the chamber for a fixed gas ratio, total flow and temperature, the resulting film will become more compressive. On the other hand, by decreasing the

pressure within the chamber, the extent of the reaction will migrate further down the chamber and the resulting thin films will be more tensile.

A similar relationship is involved with the total flow rate of the furnace. By increasing the total flow, the reactions can be pushed further down the chamber (with high flow rates) or keep them confined to the point of entry (with low flow rates). By increasing the flow rates, the film will be more tensile, and by decreasing the flow rates, the film will be more compressive [1]. Reduced pressures tend to reduce unwanted gas-phase reactions and improve film uniformity across the wafer. Increasing the chamber temperatures tend to increase the deposition rate.

1.3 Silicon nitride (Si_3N_4)

Bulk silicon nitride (Si_3N_4) is a hard, dense, refractory material. Its structure is quite different from that of silicon dioxide: instead of flexible, adjustable Si-O-Si bridge bonds, the Si-N-Si structure is rendered rigid by the necessity of nitrogen forming three rather than two bonds. CVD silicon nitride is generally amorphous, but the material is much more constrained in structure than the oxide. As a consequence, the nitride is harder, has higher stress levels, and cracks more readily.

The dense structure of silicon nitride does not provide the open channels found in oxide structures; thus, the nitride is widely employed in electronics as a barrier material. Even hydrogen diffuses slowly in the nitride film, and other small positive ions (Na^+ or K^+) are effectively blocked by thin nitride layers. Since oxygen diffuses very slowly through the nitride, deposited nitride can prevent an oxidation of the underlying silicon: this property is exploited in local-oxidation-of-silicon (LOCOS) transistor isolation. Nitride layers are also employed as etch stop layers both for wet etching and plasma etching.

Deposited nitrides almost always contain hydrogen, typically much more than in the comparable oxide films. The source of the hydrogen is the silane precursor and possibly also the ammonia oxidant employed in most deposition schemes, but the presence of hydrogen in the film is a consequence of the nitride structure. It is very difficult for the atoms in an amorphous but constrained film like silicon nitride to occupy all positions allowing the valence of each silicon and nitrogen atom to be filled: that is, a lot of broken bonds are present. These bonds are readily occupied by hydrogen atoms. The amount of hydrogen and the bonding (Si-H or N-H) can be measured by infrared spectroscopy, and are important in characterizing the properties of plasma nitrides. The stoichiometry of nitride films also varies widely so that the refractive index can vary from about 1.8 to 2.2. This is another useful control parameter for nitride deposition.

Silicon nitride thin films have been extensively used in various technological areas, especially in microelectronic devices such as passivation layers, interlevel insulators, and dielectrics. All these applications are due to silicon nitride’s remarkable

physical properties such as a high dielectric constant, high insulation strength, low creepage, and good resistance against sodium as well as water vapor. In addition, they also have excellent mechanical properties and stability. In addition to the above physical and mechanical properties, silicon nitride films have another special characteristic, namely the spectral selectivity, which can be used in optical coatings, used as a diffusion mask for local oxidation of silicon in MOS processing and used as a guiding layer in optical waveguides [2].

1.4 Silicon oxynitride (SiON)

There are some strong requirements for the devices for optical communication such as low propagation loss, efficient fiber-to-chip coupling, low insertion loss, small bend radii, and low fabrication cost that should be met for successful realization of the technology.

Most of the materials used in integrated optics so far are classified as either low contrast (e.g. silica, $LiNbO_3$, polymers) or high contrast (e.g. InP, silicon on insulator). The satisfaction of all of the above mentioned requirements simultaneously for both of these systems is rather difficult if not impossible. In the low contrast systems the fiber-to-chip coupling efficiency is excellent due to the large size of the single mode waveguides, but they have a low integration density since large bend radii (10-30 mm) are required for low loss operation. On the other hand, high contrast systems allow very small bending radii (down to 0.15 mm) with low losses, but efficient fiber-to-chip coupling is difficult to obtain due to small waveguide dimensions.

The commercially planar waveguide technology is typically based on low-index contrast (0.7 %) silica material. This technology platform ensures planar waveguide components with low propagation loss (less than 0.05 dB/cm) and low fiber-to-chip coupling losses. However, to increase the level of functional integration and reduce the fabrication cost, it is necessary to decrease the component size. Therefore core materials with higher refractive index have become the center of attention in the field of integrated optics devices for telecommunication. The propagation loss of high refractive index contrast waveguides is influenced by the material absorption loss and scattering by surface roughness of the waveguide core.

In recent years, growing attention has been paid to silicon oxynitride (SiO_xN_y or SiON for short) as a potential material for integrated optics. This attention has been motivated mainly by its excellent optical properties such as low absorption losses in the visible and near infrared, a large refractive index range and compliance with standard CMOS technology. SiON combines the dielectric properties of SiO_2 together with good chemical inertness and low permeability of Si_3N_4. In addition, the index of refraction of SiON layers can be easily adjusted continuously over a wide range between 1.45 (SiO_2) - 2.0 (Si_3N_4) which comes to be a very attractive property that allows fabrication of

waveguides with desired characteristics of fiber match and compactness. Moreover, the growth of SiON layers on silicon substrate is done by well established standard silicon integrated circuit processing technology which is also a key point towards a low cost mass production.

In addition, after the optimization of the processes it has become a well-controlled technology with small technological tolerances. The relatively high index contrasts which can be obtained enable a high functional density on the chip. It is quite natural to apply in this technology the layer stack on the top of a silicon wafer which has several advantages. The SiON technology is also used for integrated optical telecom devices. The high contrast pure silicon technology using SOI wafers has only recently reached a state in which it can be applied in practice; because of the high refractive index contrast which can be obtained it might be most useful for circuits in which high compactness is required such as in sensor arrays.

Amorphous silicon oxynitride layers are deposited by various techniques. The most used growth technologies are plasma enhanced chemical vapor deposition (PECVD) and low pressure chemical vapor deposition (LPCVD). The PECVD process is found to be more efficient in controlled deposition of films with refractive indices below 1.7. The deposited layers have good uniformity of the refractive index and in layer thickness with run-to-run reproducibility [41].

1.5 Optical waveguides

Integrated optical systems generally consist of an optical chip which is provided with a network of optical waveguides. The light is propagating through these waveguides according to certain field patterns (the guided modes).

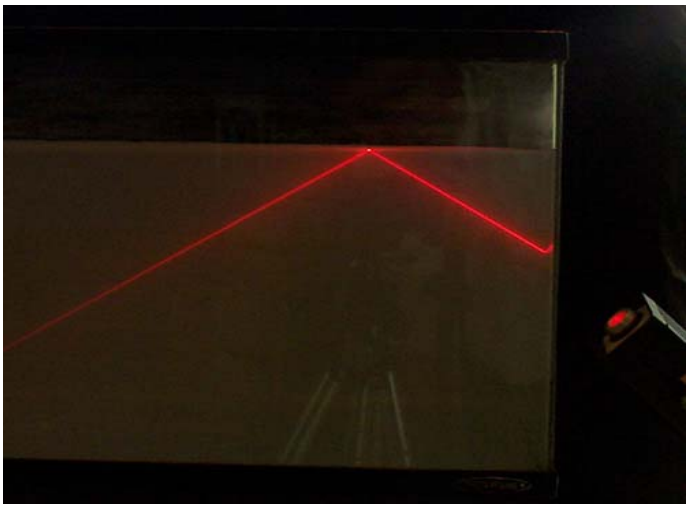

Figure (1-2): Total internal reflection of light [3]

Just as in optical fibers light is confined to the waveguide as a result of total internal reflection (TIR) against material boundaries. This happens when light arrives through an optically dense medium of refractive index n_1 at its boundary with an optically rarer medium of refractive index n_2 (i.e., $n_1 > n_2$) and the angle of incidence θ_i is greater than the critical angle θ_c where, $\sin \theta_c = n_2 / n_1$, as shown in figure (1-2) [3] and figure (1-3).

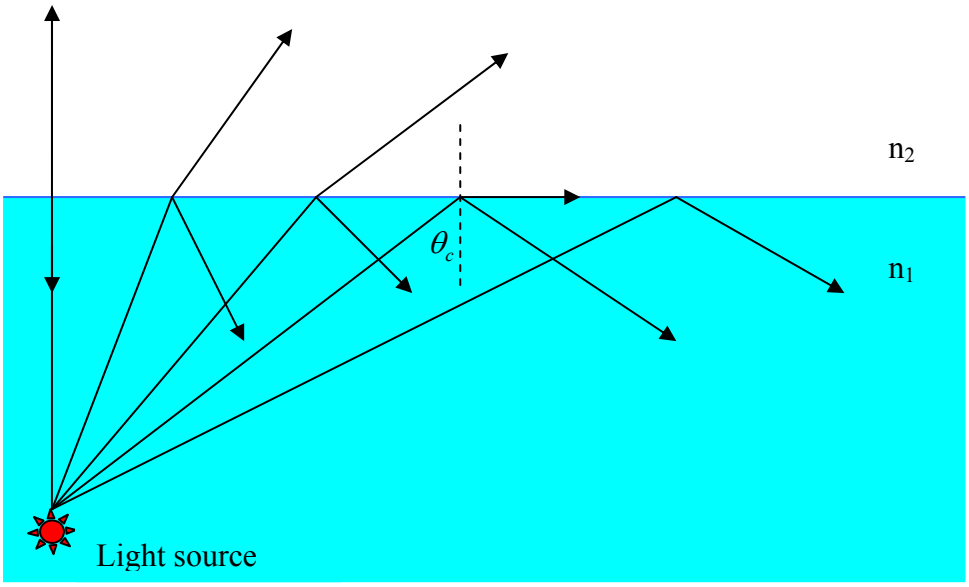

Figure (1-3): Different light rays with different incidence angles are arriving to the boundary of two mediums from a higher refractive index medium to a lower refractive index medium where the total internal reflection occurs when the angle of incidence is greater than the critical angle

Light in optical fibers is exposed to multiple total internal reflections which may occur as a consequence of the core layer having a higher value of refractive index than the cladding layer as shown in figure (1-4).

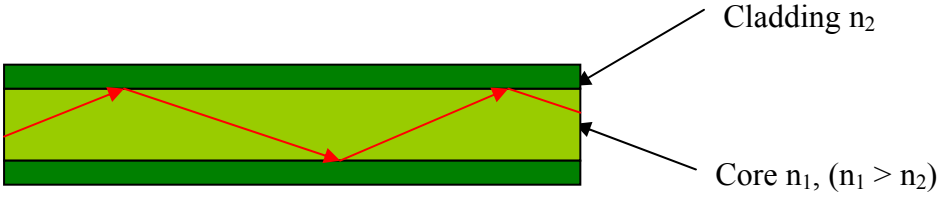

Figure (1-4): Multiple total internal reflections in an optical fiber

Most IO systems are structured as a planar multilayer stack deposited on top of a substrate (e.g. a glass slide or a silicon wafer). Sometimes the higher index core is defined by locally implementing (mostly by diffusion) ions. Layer thicknesses are on the order of magnitude of 0.1–10 μm just as the cross sectional dimensions of the core. Lateral dimensions of a functional optical chip are in between some millimeters and some centimeters.

In some IO systems there is no lateral patterning; in these systems, called slabguides, the light is confined in the transverse direction only and not in the lateral direction. These slabguides are useful for straightforward propagation of relatively wide beams (hence with a low lateral divergence) only. They are seldom applied in integrated optics, but nevertheless they will be met in several sensors. Mostly used are the channel-type waveguides in which the light is also confined in the lateral direction [4].

Waveguides typically consist of a core with a higher refractive index n_1 than the surrounding cladding layer n_2. This structure is transferred to the planar technology for silicon wafer processing using different types of anorganic films, which are standard materials in MOS technology. Silicon technology offers different transparent materials with a wide range of refractive indices which can be used for light guiding films and waveguide structures. The most common material for the cladding layers is silicon dioxide (SiO_2). It is normally used as a dielectric layer in MOS transistors. The refractive index is about 1.46, and the absorbance rate is extremely low in the visible spectral range. SiO_2 can be deposited by thermal oxidation of silicon or by chemical vapor deposition (CVD) using low pressure (LPCVD) or plasma enhanced CVD (PECVD).

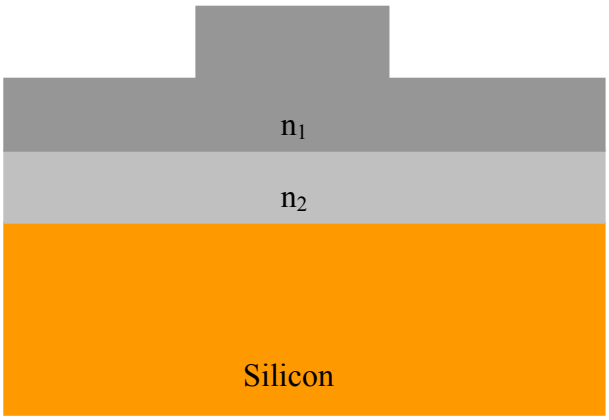

Figure (1-5): The rib waveguide

Optical waveguides on silicon can use different types of setup. Figures (1-5), (1-6) and (1-7) depicts the most common structures of waveguides suitable for monolithic integration.

The rib waveguide [figure (1-5)] consists of a low refracting layer which is covered by a layer with a higher refractive index as the light guiding film. The top layer is partly etched to form a rib. The electromagnetic wave can only propagate in the area of the rib, outside the rib no mode can exist due to the reduced film thickness. Because of the roughness of the etched surface the propagation loss of this kind of waveguide is large.

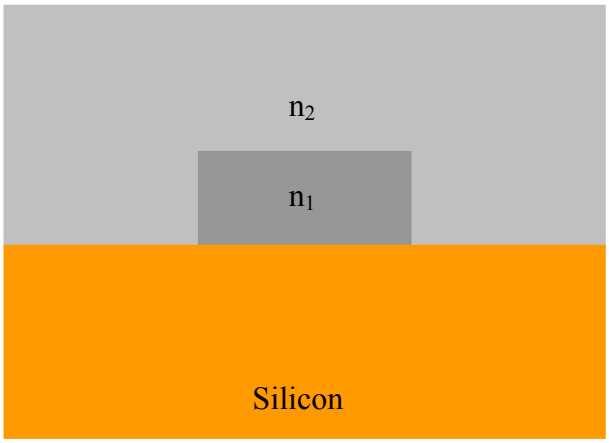

Figure (1-6): The channel waveguide

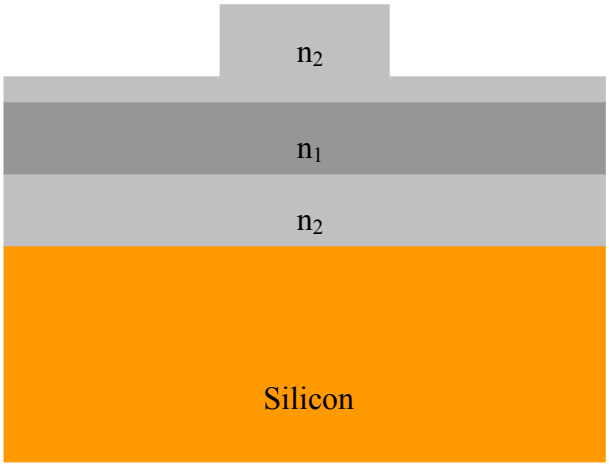

Figure (1-7): The strip loaded waveguide

Types of figure (1-6) waveguides (channel waveguides) depict less propagation loss. This kind of waveguide can easily be integrated on silicon, but propagation loss is not optimized due to the roughness of the vertical rib side walls caused by dry etching.

The strip loaded film waveguide shown in figure (1-7) exhibits very low propagation loss. The surface cladding layer is deposited on top of the light guiding film, and the etching process to form the strip does not affect the quality of the light guiding layer, so propagation loss is very low. The integration process is as simple as in case of the rib loaded waveguide.

In channel and rib waveguides, monomode behavior depends on the thickness, the width and depth of the core and on the difference between the core and cladding refractive indices. If the difference between the refractive index of the core and cladding is large (higher than 10 %), monomode behavior is achieved with a core thickness of hundreds of nanometers. The cladding thickness is a few micrometers due to the small penetration of the evanescent field into the cladding. However, the rib depth must be around several nanometers for monomode waveguides.

As shown in figure (1-8), the modes are in different locations for the rib and strip loaded waveguides. For rib waveguides, the mode is confined just below the rib, which gives a symmetric mode profile. In practice, it is difficult to produce such devices with smooth rib sidewalls and since the mode is confined just below the rib, there will be significant scattering loss. With strip loaded geometry, the mode is confined to the higher index core below a lower index loading strip layer. Since the mode is not contained in the strip, this configuration is insensitive to sidewall roughness.

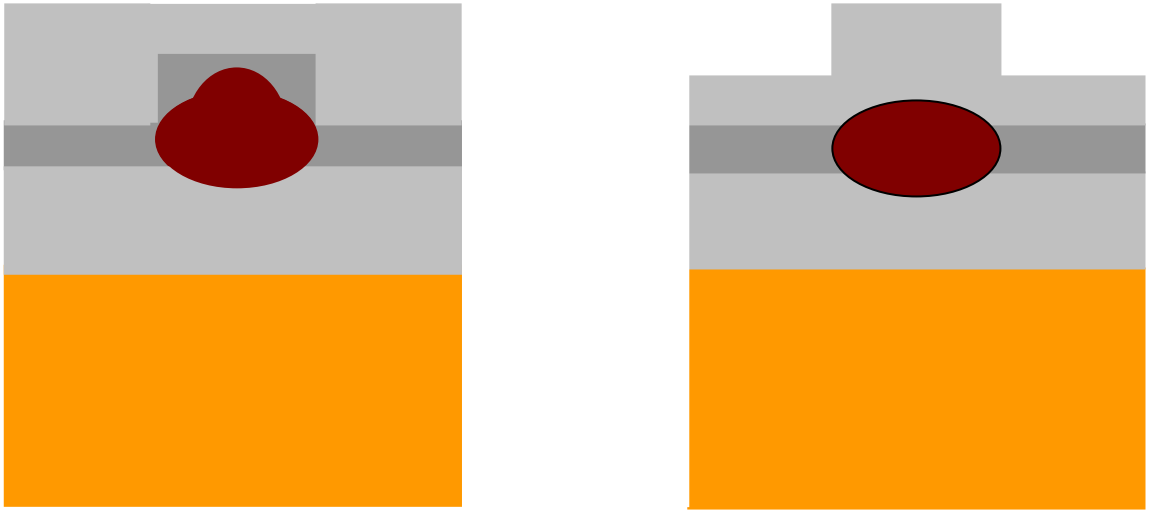

(a) (b)

Figure (1-8): Schematic cross-section of waveguide structures with the location of the mode in each case (a) Rib waveguide (b) Strip loaded waveguide

The difficulty in designing strip loaded waveguides is that their fundamental modes are inherently elliptical, making them difficult to couple to optical fibers. It

requires much effort to obtain circular mode profiles suitable for coupling to optical fibers.

The propagation of light through the waveguides is formally described by Maxwell theory. It can be derived that for each wavelength, λ, the guided light propagates as a running wave in certain patterns of the electro-magnetic field, each pattern with its own specific velocity; one speaks about guided modes. The number of guided modes which can propagate through the waveguide depends on the values of the refractive indices, the geometry of the channel structure and the wavelength used. Structures through which one mode can propagate at only a given wavelength are easily designed and realized. These monomodal waveguides are required by most IO sensing principles. When lowering the cross sectional dimensions or the refractive index of the core a state can be reached such that at lower values of these parameters no guided mode can be supported anymore. This state is called the cut-off.

Generally, the electro-magnetic field of the modes consists of three electrical and three magnetic field components. If one (for slab modes) or two (for channel modes) of them are known Maxwell theory delivers some simple relations for calculating from the known components all other ones. From Maxwell theory it can also be derived that in a good approximation for most waveguide types the guided modes can be classified into two groups: TE-modes and TM-modes, where the electrical, respectively the magnetic, field has a dominant component along the lateral direction only as shown in figure (1-9) [5]. Three of the field components are zero leaving for TE-modes H_y and H_z and for TM-modes E_x and E_z only. Generally, the component of the field along the propagation direction (defined as the *z*-axis) is relatively small. The approximation is exact for slab modes and is very good for the commonly used rib-type channel modes.

From Maxwell theory it can be shown that for a given vacuum wavelength of the light, λ_0, the i^{th} TE mode can be mathematically described by:

$$E^i{}_y(\lambda_0, x, y, z, t) = E^i{}_y(x, y, \lambda_0)\exp j\left[N^i{}_{eff}(\lambda_0)k_0 z - \omega t\right] \tag{1-1}$$

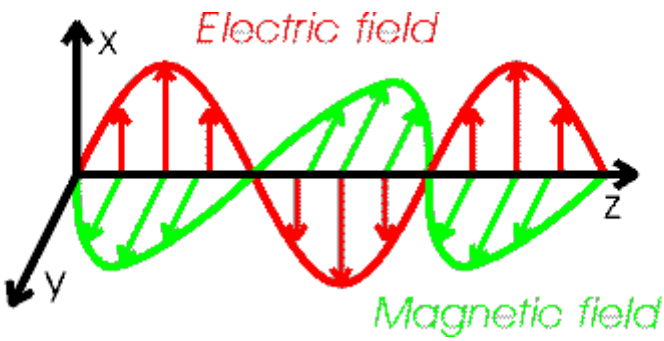

Figure (1-9): The propagation of light as a running wave of the electro-magnetic field [5]

The formula shows a harmonic wave running in the Z-direction, with an angular frequency ω. Here $k_0 = 2\Pi / \lambda_0 = \omega / c$, where c is the vacuum velocity of light. $E^i_y(x, y, \lambda_0)$ is called the i^{th} field profile of TE-mode. Note that not all optical power propagates through the core layer, but that parts of it propagate through the outer layers (the cladding layers). In these layers the field strength decays exponentially with the distance to the boundary with a decay length (1/e value) in medium i with refractive index n_i being:

$$\frac{1}{k_0\sqrt{N_{eff}^{\ 2} - n_i^{\ 2}}} = \frac{c}{\omega\sqrt{N_{eff}^{\ 2} - n_i^{\ 2}}} \tag{1-2}$$

For most systems this decay length is on the order of magnitude of 0.1–1 μm. These fields outside the core layer are called the evanescent fields of the mode. These evanescent fields play an essential role in most IO sensors.

The propagation velocity of the mode is equal to c / N_{eff}, where N_{eff}, the so-called effective refractive index, being limited to the range $n_{core} > N_{eff} > (n_c, n_b)$, has taken the place of the refractive index of a homogeneous medium, through which a planar electromagnetic wave propagates. Modes are numbered according to their N_{eff}-values, the highest N_{eff} corresponding to the lowest mode number. In the case that the structure is lossy (e.g. due to some absorption or scattering) the losses are expressed by adding an imaginary component to N_{eff}.

The number of guided modes that can propagate through the waveguide, their field profiles and their N_{eff}-values depend on the refractive index distribution (meaning the values of the refractive indices of all relevant materials and the geometry of the cross section of the straight waveguide) and the wavelength used. Structures are possible through which for a given wavelength one TE mode (and often one TM mode) can propagate only: a monomodal waveguide.

1.5.1 Light coupling into waveguides

There are various ways of coupling light from the outside world into a guided mode of the chip (excitation of a guided mode): selective excitation using prisms [6] as shown in figure (1-10) or gratings [7] as shown in figure (1-11) for coupling the power of collimated free space beams into a specific waveguide mode or butt-end coupling using fibers [8] or (especially in the laboratory) free space beams focused on the entrance plane of the waveguide.

The first two methods are also utilized for the sensing itself. Because of reciprocity of light all these methods can also be used for coupling light out of the chip.

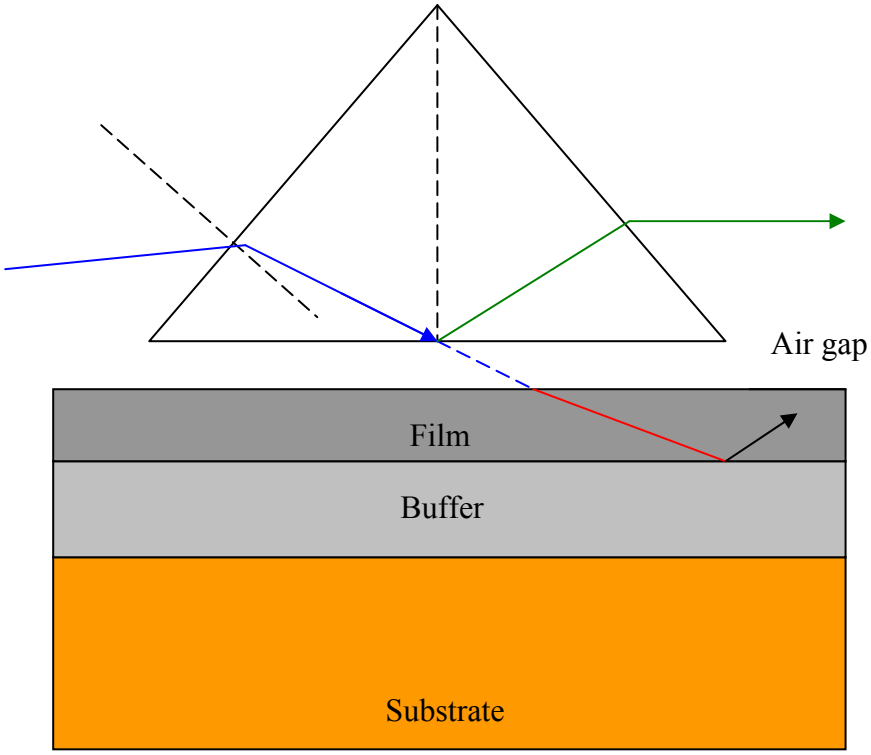

Figure (1-10): Prism coupler

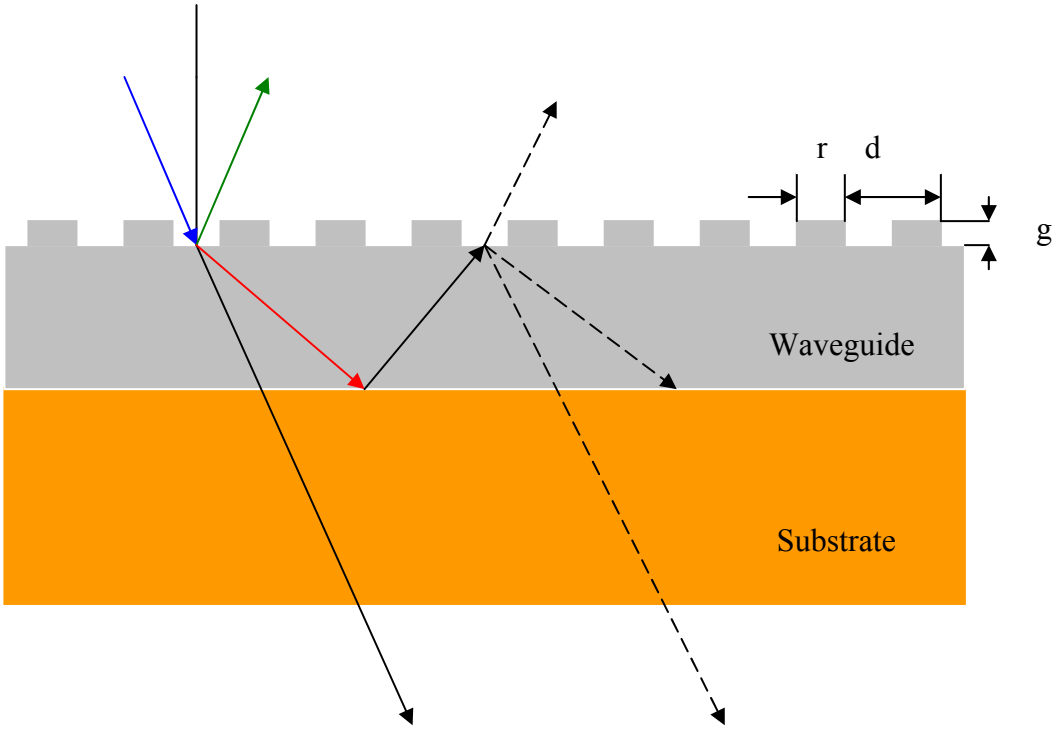

Figure (1-11): Grating coupler

1.5.2 Optical losses

The most important characteristic with the modal properties of a waveguide is its attenuation or loss, that a guided mode experiences as it travels through the waveguide. The loss arises mainly due to intrinsic material properties or imperfections that may come during the fabrication processes. A common measure of the optical loss is dB/cm and it is defined as the logarithm of the power (intensity) ratio as:

$$Loss\left(dB/cm\right)=\frac{10\log\frac{P_{in}}{P_{out}}}{l} \tag{1-3}$$

Where l, P_{out} and P_{in} are the waveguide length, output and input power, respectively. The measured total loss is the sum of the individual losses due to different mechanisms.

A mode traveling in the waveguide experiences a scattering loss, in case of facing imperfections with index fluctuations of the order of the wavelength of light. According to the location of occurrence, the scattering losses in a waveguide can be divided into two as volume and surface scattering. In general, volume scattering results from imperfections such as voids or particle contaminations. The loss due to them is proportional to the total number of scattering centers per unit length and is negligible compared to surface scattering loss.

The surface scattering loss might be of much more importance since the propagating wave interacts strongly with the surfaces that are more imperfect in terms of roughness. Namely, as the ridge waveguide is defined by etching, the surface may experience damage, in addition to which the side walls of the rib itself can be rather rough. In order to avoid these complications, a careful optimization of the reactive ion etching (RIE) process applied for the waveguides, has to be worked out.

Although both types of scattering occur at different locations, they result from the same physical process of scattering of light. The power radiated as a result of this mechanism is given by the well-known expression of Rayleigh scattering

$$P_{rad}=\frac{\omega^4\left(\Delta\varepsilon\right)^2E^2}{12\pi\varepsilon_0c^3}=\frac{4\pi^3c\left(\Delta\varepsilon\right)^2E^2}{3\varepsilon_0\lambda^4} \tag{1-4}$$

where $\Delta\varepsilon$ is the excess polarizability and E is the electric field component of light. The important feature of the equation is that the radiated power is inversely proportional to the fourth power of the wavelength.

Another type of energy loss in waveguides is in the form of the loss of the optical power from the mode into the media surrounding the waveguide. It can be observed in both slab and ridge waveguides in terms of leakage of the mode into the substrate or air. In fact, scattering losses may be included in this category, too. Radiation losses can also take place in the waveguides having sharp bend or curvature, but this is not an issue for our case. The SiO_2 lower cladding thickness of $2\ \mu$m ensures no radiation leakage in the substrate [41].

1.6 Chemical sensors

1.6.1 Background

Sensors technology has been identified as one of the most important technologies for the 21st century. Sensors are important components in quality control as well as for online control of different processes in industry.

Sensors are usually designed to monitor one thing at a time and are generally devices which transduce a physical or chemical parameter into an electrical or optical signal. Physical parameters which are commonly monitored with sensors are temperature, pressure, force, magnetic field, etc, while chemical parameters of interest most often are the concentrations of chemical substances.

A sensor can be described by the:

- detection mechanism
- parameters it is sensitive for, selectivity
- concentration range, sensitivity
- speed of response
- operation temperature
- life time

Physical sensors are different than chemical sensors. Physical sensors are normally influenced by one or very few parameters only but chemical sensors might be influenced by hundreds of parameters.

Sensor technology in general is multidisciplinary and this is particularly true for chemical sensors, simply because knowledge in physics and electronics has to be combined with knowledge in disciplines such as electrochemistry, biochemistry, etc. This is an inhibiting factor in the development of chemical sensors but more and more

scientists are now crossing discipline boundaries and new multidisciplinary research groups are being set up.

Chemical sensors usually consist of a sensitive layer or coating and a transducer [9], [10]. Upon interaction with a chemical species (absorption, chemical reaction, charge transfer, etc.), the physicochemical properties of the coating, such as its mass, volume, optical properties, or resistance, etc. reversibly change. These changes in the sensitive layer are detected by the respective transducer and translated into an electrical signal such as frequency, current, or voltage, which is then read out and subjected to further data treatment and processing.

Various inorganic materials serve as chemically sensitive layers that can be coated onto the different transducers [11]. The different sensitive materials and their operation conditions, such as elevated temperature, impose certain requirements on the transducer design [12].

The large amount of parameters that influence the sensor signal of a chemical sensor gives a lot of effects that has to be taken into account when using chemical sensors:

- Chemical sensors are normally non-specific sensors, there are very few 100 % selective chemical sensors
- Cross-sensitivity: some chemicals may interact to give a different signal from the component in a mixture compared to the single component
- Temperature sensitivity, chemical reactions, adsorption, desorption, and diffusion processes have a large temperature dependence, and temperature control is crucial
- Memory effects: the history of the sensor influences the response to a certain chemical component, so frequent recalibration is necessary or advanced signal processing
- Drift problems related to the sensor technology in use, e.g. MOSFET sensors, SAW sensors or conducting polymers may have electronic drift not related to chemical interaction
- Other drift problems, that is, chemical sensors in general suffer from long term stability problems

Hence, there are some special measurement techniques used for chemical sensors:

- Twin sensors are used to get rid of drift problems not caused by the chemical species to be measured
- Recalibration normally has to be used frequently. Special calibration algorithms for chemical sensors are being developed
- Regeneration of the sensor by heating might reduce memory effects
- Short test gas pulses might reduce memory effects
- Scanning of the temperature enhances selectivity

- Large areas of catalytic metal influences selectivity
- Advanced signal processing enhances the sensitivity
- Sample handling and sample treatment, e.g. to keep a constant temperature and humidity of the samples

The response of a sensor to a certain chemical component can be measured in different ways [13]:

- The difference in sensor signal between a reference and the test species
- The ratio between the sensor signal at a reference related to the test species
- The derivative of the initial change of the signal due to a chemical species
- The integral of the change of the signal due to a chemical species

Semiconductors play an important role in sensor technology because of their variable conductivity. The concentration as well as the mobility of charge carriers in a semiconductor is sensitive not only to physical parameters such as temperature, light and mechanical tension but also to chemical parameters.

Integrated optical (IO) devices are increasingly used as transducers for optochemical sensing applications [14], [15]. The utilization of microtechnology for the integration of these devices offer some advantages as a better control of the light path by the use of optical waveguides, high sensitivity, mechanical stability, miniaturization, and the possibility of mass production [16]. The use of standard silicon microelectronics technology for the fabrication of these devices allows a high homogeneity of the waveguide material and the possibility of final integration of optical and electrical functions on the same chip [17].

In general, integrated optical sensors make use of the evanescent field detection principle. In an optical waveguide, confined light travels within the core layer. However, part of the guided mode (evanescent field) travels through a region that extends outward into the media surrounding the waveguide. When there is a change in the optical characteristics of the outer medium (i.e., refractive index change), a modification of the optical properties of the guided mode is induced via the evanescent field. To detect this variation, Mach-Zehnder Interferometer (MZI) can be used. The refractive index change is evaluated by the intensity modulation produced by the interference of light traveling through the two branches of the interferometer, one of which is exposed to the refractive index variations of the outer medium.

To obtain an efficient transducer for detecting molecular interactions, the optical waveguides of the sensor should have a high surface sensitivity. The strength and distribution of the evanescent field in the outer medium need to be maximized in order to assure a high response for changes in the optical properties of the surrounding medium.

For sensing applications, the optical waveguides that form the MZI sensor must have two features: monomode behavior and a high surface sensitivity. Optical waveguides based on Total Internal Reflection (TIR) have been experimentally proved to have high surface sensitivity [18]. For implementation in a MZI, these waveguides should have monomode behavior that, assuming a fixed wavelength, can be controlled with a proper design of the thicknesses and refractive indices of the waveguide layers. Finally, a rib structure is designed to achieve lateral light confinement. Width and depth of this rib are also essential for assuring a single-mode optical waveguide.

There has been extensive research reported using optical fibers and planar waveguides for chemical sensors and optical guided-wave chemical sensing is an extremely promising and fast growing technology. However, planar waveguide devices utilizing modern microfabrication technologies facilitate monolithic integration of several components in a single chip for simultaneous multiagent detection. These compact integrated optical devices are robust, give much flexibility in material selection to optimize the sensitivity and have the potential for low-cost manufacturing [19].

Since so many different sensors are found one can ask: which one is the best? There are so many different sensing situations and criteria to be considered that the general answer is: the sensor which will do the job. There is, however, one characteristic of a chemical sensor which sets it apart from the others and that is ruggedness. This term describes the ability of the device to maintain its performance specifications even under adverse operating conditions. In a pragmatic sense it is understood as reliability.

Ruggedness may have different meanings; a mechanically rugged device is able to withstand mechanical shock, vibrations, mechanical stresses, and so on. Chemical ruggedness has a slightly more subtitle meaning. It is related to selectivity and means that the output of the sensor is unaffected by unforeseen chemical changes in the operating environment. Generally speaking, rugged sensors are those commercially most successful because they are reliable or because they are the only ones which can provide information under conditions in which other sensors would be unable to operate.

It is generally possible to distinguish two types of interaction of the chemical species with the sensors: a surface interaction in which the species of interest is adsorbed at the surface, and a bulk interaction in which the species of interest is absorbed and partitions between the sample phase and the sensor.

1.6.2 Historical Perspective of chemical sensors

Classical solutions to chemical sensing tasks have been dominated by complex, expensive laboratory methods such as gas chromatography and ion-mobility

spectroscopy. Although these methods are accurate for detecting chemical concentrations and in discriminating among chemicals, their cost is often prohibitive for many low-end, chemical sensing applications ranging from residential sensing of toxic chemicals to the detection of seafood freshness and breath alcohol analysis. To lower the cost of chemical sensing systems sufficiently to compete in these low-cost markets, a new approach to chemical sensing needs to be adopted.

In order to address the needs for chemical sensing systems in consumer and other low-end markets, it has been useful to use miniaturization techniques that perhaps sacrifice some of the accuracy of laboratory methods for lower cost, faster response times and greater accessibility. Since the early 1970's, the microelectronic chemical sensor has been investigated as this low-cost, miniaturized alternative to laboratory chemical sensing methods. However, the miniature chemical sensor has been plagued by problems with:

- Reproducibility: inconsistent responses to the same chemical over time
- Selectivity: difficulty in discriminating among chemicals
- Sensitivity: difficulty in detecting low concentrations of particular chemicals
- Stability: difficulty in detecting chemicals of interest across changes in ambient conditions
- Response time: typically on the order of tens of seconds to minutes

Chemical sensing systems that overcome some or all of these problems have had difficulty in keeping system cost down at a manageable level for the corresponding market for particular sensing applications. However, some progress has been made in the research community since the 1970's in addressing this delicate balance between cost and robustness of viable chemical sensing systems. There are three general tasks of interest in these systems: concentration detection, chemical discrimination, and response time optimization. Most microelectronic chemical sensors are able to detect concentrations reasonably well at medium to high concentrations.

Since the 1970's, the microelectronic chemical sensor has been explored as a low-cost alternative to laboratory chemical sensing methods. Many of the microelectronic sensor technologies are based simply on conductivity changes in a material in response to chemicals in the environment. The simplest of these conductivity-based sensors, the thin-film sensor, was first introduced into the research community in the early 1970's. As shown in figure (1-12) the thin-film sensor is simply a film of chemically sensitive material, such as tin oxide [20] or polypyrrole [21] whose conductivity changes in response to reducing chemicals in the sensing environment. The thinness of the film is required, because these conductivity changes are primarily based on surface interactions and the surface must be a significant part of the entire sensor in order to detect these changes. The output of the sensor may be read either as a current or as a voltage.

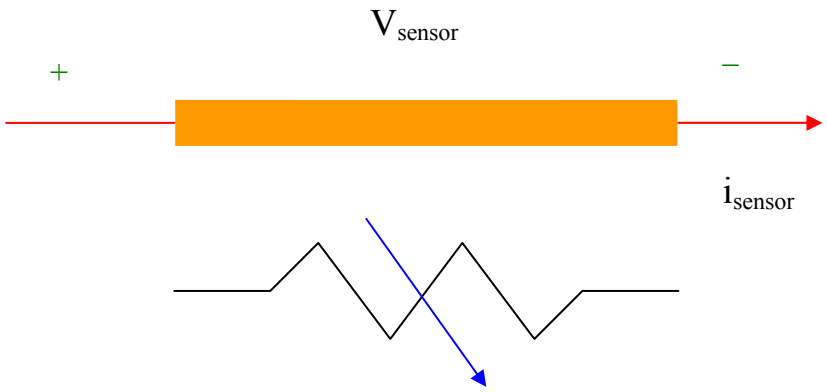

Figure (1-12): Basic structure of the thin-film sensor

The metal-oxide, thin-film sensors are the only miniaturized chemical sensors that have had significant impact in commercial markets. For example, tin oxide (SnO_2) and iron oxide (Fe_2O_3) [22] have frequently been used to detect hydrocarbons and combustible gases in a variety of applications. By far, the most popular of these sensors has been the Taguchi-type sensor, manufactured by Figaro Engineering in Japan; these sensors are made up of primarily tin oxide modified with various catalysts and additives to detect particular hazardous gases such as carbon monoxide and methane [23].

Perhaps the most important promise of these thin-film sensors for the development of viable chemical microsystems is their compatibility with standard integrated circuit fabrication processes. Metal oxides and conducting polymers can be deposited onto standard integrated circuit substrates, often after circuits have already been fabricated on the same substrate.

Also, in the early 1970's, the ion sensitive field effect transistor (ISFET) was developed in the research community. As shown in figure (1-13) an ISFET is simply a MOSFET without a gate. The oxide layer of the FET is replaced with an insulating, chemically sensitive membrane. Charges from sensitive chemicals accumulate on top of this insulating membrane and are amplified through the operation of the FET [24]. Although the amplification properties of the transistor in these devices seem very attractive for sensing chemicals, the vulnerability of the insulating membrane to environmental poisoning and subsequent transistor breakdown has prevented the ISFET from gaining popularity in commercial markets.

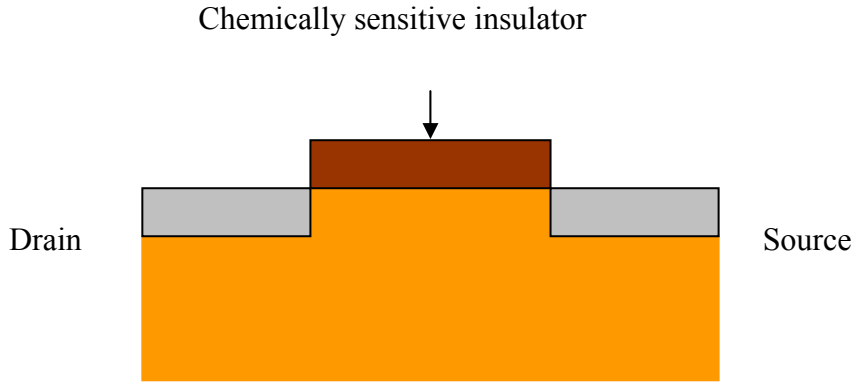

Figure (1-13): ISFET (ion selective FET)

Since the insulator layer provides no optical shielding from the surrounding FET device, light sensitivity has also proven to be a problem with these devices. As a result, the ChemFET has demonstrated more potential for integration into practical chemical sensing applications although it is less selective and chemically sensitive than the ISFET as shown in figure (1-14). Unlike the ISFET, the ChemFET uses a standard oxide layer as the insulator and a chemically sensitive metal, such as palladium, as the gate [25]. The addition of the gate minimizes light sensitivity problems that are a problem in ISFETs. Likewise, potential poisoning of the oxide layer is minimized not only by the inherent physical barrier provided by the metal gate but also by the fact that the silicon dioxide is fairly resilient to environmental poisoning.

Modifications and hybrids of the ChemFET and the ISFET such as the surface accessible FET or SAFET [26] [see figure (1-15)] and the Suspended Gate FET or SGFET [27] [see figure (1-16)] were also introduced into the research community in the 1970's; despite the enhanced selectivity and sensitivity of these devices over the ChemFET, however, they share the common flaw of a short lifetime due to the accelerated degradation of the partially or completely exposed oxide layer. Because of its relative low sensitivity to environmental degradation, the ChemFET is thought to be the most promising of the MOSFET-based chemical sensors in spite of its relatively low selectivity compared to other chemically sensitive FETS.

The ChemFET sensors are also well suited to monolithic integration onto standard integrated circuit substrates. Although fabrication of these devices on standard substrates is more complex and slightly less advanced than that of the thin film devices, the technology for integration is nevertheless currently available in the research community.

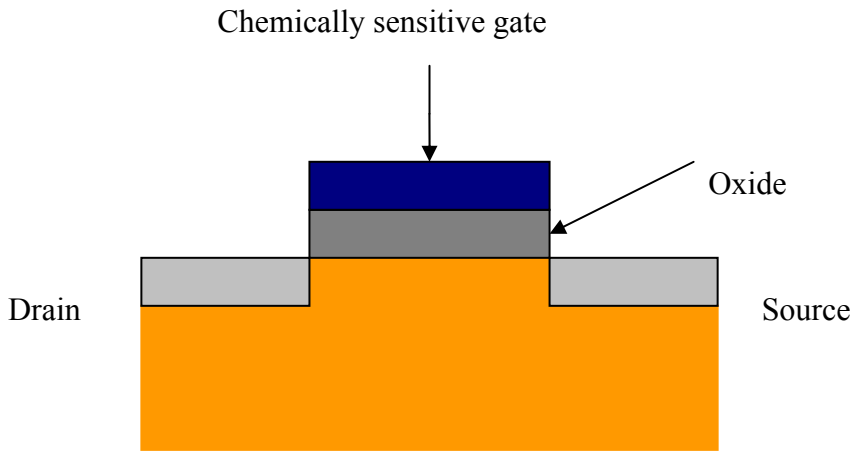

Figure (1-14): ChemFET Structure

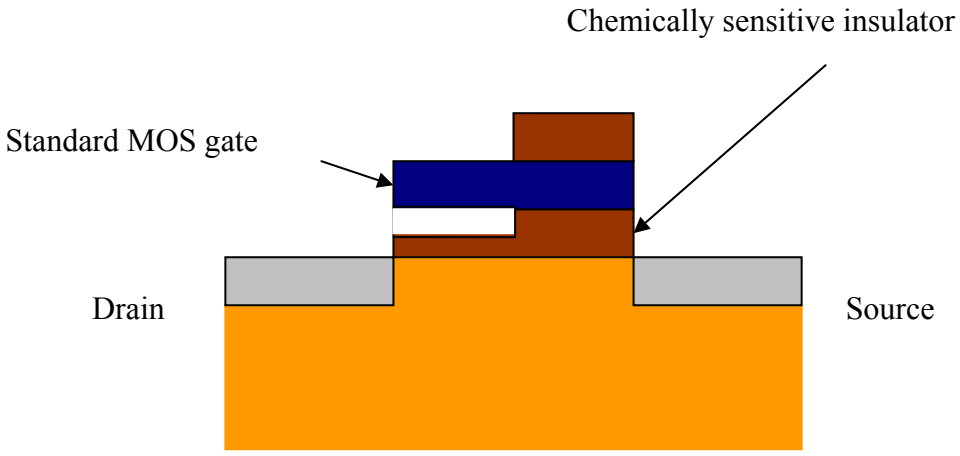

Figure (1-15): SAFET structure

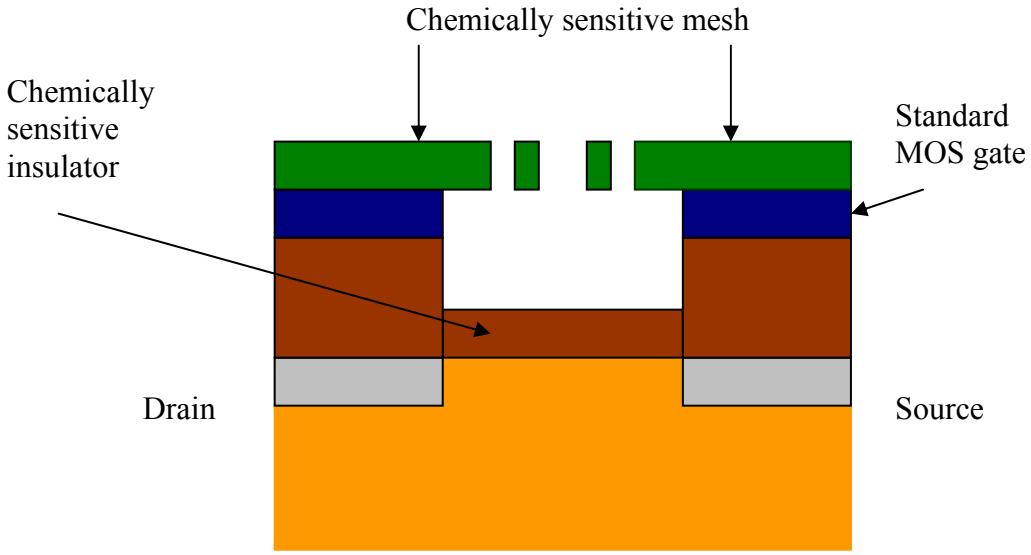

Figure (1-16): SGFET structure

The MOS-based and conductivity based devices described above belong to the largest class of microelectronic chemical sensors: those based on a single stage of transduction between chemical input and electrical output signal. Significant improvements in the sensor response times are attained as a result of this single level of transduction. Furthermore, the cost of implementing and manufacturing systems that use single transduction stage devices for chemical sensing is minimized by the fact that standard microfabrication techniques are frequently sufficient to produce many of the MOS-based and conductivity based sensors.

Although the ChemFET and thin-film sensors are undoubtedly the most popular of the single transduction-stage chemical sensors, a variety of other chemical sensors have also been explored in the last three decades for accomplishing chemical analysis tasks. Chemically sensitive MOS capacitors are similar to ChemFETs; however, since they lack the source and drain of the Chem-FET, their capacitive output is difficult to capture and to process for chemical analysis. Chemically sensitive Schottky barrier diodes contain a chemically sensitive metal as the top layer of the diode [28]; the diode barrier height alters in the presence of a reducing chemical; however, as in the case of the MOS capacitor, this change in barrier height is difficult to measure in a reliable and reproducible manner. The solid electrolyte has also shown potential for improved performance over ChemFET and thin-film sensors, since many of the available electrolytes that are chemically sensitive have an ionic sensitivity that is highly selective to particular chemicals [29], [30]. However, fabrication difficulties involved in bulk micromachining and establishing a reference electrode for these devices have prevented most electrolyte-based devices from becoming commercially viable [31].

Multiple stage transduction devices have demonstrated use for chemical sensing applications. The thermal sensor uses a thermistor to measure the heat generated by reactions between particular chemicals and the chemically selective layer coating the temperature sensors. However, the low efficiency of these devices in capturing reaction heat limits their suitability for the low concentration limits required for many chemical sensing applications. The mass sensors, on the other hand, suffer from the opposite problem. Based on sensing the added mass of a chemical reacting with the sensor surface, these devices are extremely sensitive, making them also very noisy and inherently vulnerable to interference. The piezoelectric sensors which sense the added force of an additional mass on the sensor surface have very broad selectivity. The surface acoustic wave SAW devices have improved selectivity over their piezoelectric counterparts and can often be made using standard IC fabrication techniques. In these sensors, a chemical reacts with a chemically selective layer on the sensor surface, causing a frequency, phase, or amplitude shift in the acoustic wave traveling across the device. Finally, the optical sensor has two advantages over all other types of chemical sensors. These sensors are selective and the sensing environment is not required to interact physically with the sensor. This characteristic makes optical sensors well suited to remote sensing and applications where electricity in the sensing environment can be hazardous.

1.6.3 Applications of chemical sensors

The applications for chemical sensors are innumerable. Chemical analysis is presently carried out, or should be carried out, in almost all areas of technology. Obvious is the use of chemical sensors in laboratories, in medical clinics, industrial processes and bioreactors but there is, most certainly, a number of other places where these devices can find applications [32]. Conceivable applications might be for food freshness monitoring in shops, field analysis of plants and soil, portable air pollution monitors and many more.

In the medical area there is a pronounced need for chemical sensors. Medical diagnosis makes significant use of chemical analysis and incredible numbers of tests are carried out in clinical laboratories. The costs for these activities are very high and there is a significant time delay involved.

New sensors that enable rapid analysis will significantly reduce the costs and will also enable appropriate treatment to be set in at an earlier stage. Sensors which are cheap and easy to use will also facilitate decentralization of the chemical analysis to the hospital wards and to the general practices. Even sensors which can be used at home e.g. by chronically ill patients can be conceived.

Another important opportunity for chemical sensors is continuous monitoring of chemical parameters during intensive care. This is an area which is subject to a lot of research. Equipment for monitoring blood gases such as oxygen and carbon dioxide are

used today. Sensors for these as well as sensors for monitoring of potassium, calcium etc. are at present being developed further, especially with respect to miniaturization and biocompatible encapsulation. Silicon technology has opened up new possibilities for miniaturization but the delicacy and sensitivity to moisture and ionic contaminations of silicon devices emphasis the importance of good encapsulation.

In industrial processes there are a number of chemical parameters which should be measured in order to optimize the processes both with respect to efficiency and quality. Looking closer into different industrial processes one finds that surprisingly few parameters are actually measured. With some exceptions the few analyses which are undertaken are done so by bringing samples to a chemical laboratory. This is not only expensive but also includes a time delay which quite often makes the information useless for process control.

To have the ability of using modern computer technology for efficient process control, continuous on line measurements have to be done by means of chemical sensors. The reason why this is done to such a small extent today is not only the lack of sensors for many substances but also the fact that existing chemical sensors are often not sensitive, selective and stable enough for the use in industrial processes.

Factors that limit the usability of existing sensors are things like temperature and pressure, interference from other chemical parameters, fouling and mechanical shock. Many existing sensors would certainly be useful if they were further developed to withstand such conditions. The main reason why this is not done is that the demands are very diversified and the sensor needs to be designed specifically for each application. This is expensive and the market for each version of a sensor is too small to cover the development costs. A good sensor for process control purposes can be sold at very high prices but very few sensor manufacturers are prepared to take the economical risks involved. This means that the potential users of process control sensors have to undertake, or at least pay for, the development of sensors in their particular applications. This fact is slowly being accepted since improved process efficiency and quality are often the most powerful means for competition and improvements in process control can therefore be highly valuable in economic terms.

Environmental monitoring is another field of applications for chemical sensors in general and gas sensors in particular. In more and more countries people are becoming aware of environmental hazards in their lives. Long-term exposures to even trace amounts of hazardous gases have been shown to have severe medical implications. Health authorities have a demand for portable instruments for monitoring and the industry is interested in alarm systems for protection against elevated levels of toxic and explosive gases.

The most difficult task is to develop gas sensors with sufficiently high sensitivity and selectivity to measure concentrations at the very low exposure limits. This can be done, and has been done, for some of very reactive gases but is more difficult for less

reactive, but still toxic gases. The need for sensors for environmental monitoring is appreciated amongst health authorities but the markets for sensors for toxic gases are generally too small to attract commercial interest. The development of these sensors is therefore strongly dependent on governmental funding. Sensors for explosive gases have been shown to have much larger markets and have consequently attracted more commercial interest. Research on sensors for gas alarms is carried out by a large number of companies.

It is also worth bearing in mind that chemical sensors can be used, and are used, to measure nonchemical parameters. A well known example of this is leak detection by means of tracer gases. Other indirect measurements such as flow measurement using traces can be conceived and new sensors will probably give rise to such new possibilities.

1.7 Optical waveguide based chemical sensors

Sensors that can translate the concentration of various chemical compounds to the electrical domain are in great demand by industry. These sensors are required in process control, environmental monitoring, health care, biotechnology and the automotive industry for example. In some cases it is advantageous to use the optical domain as an intermediate between the chemical and electrical one. This can be useful for several reasons, amongst them are:

- The absence of electromagnetic interference
- No danger for explosions due to electrical passivity
- High sensitivity to many measurands
- Specific optical sensing mechanisms, such as chemical analysis by means of material specific absorption wavelengths

Many characteristics of light are available to carry the sensor information. For example the phase, the intensity (distribution), the direction of propagation, the polarization or the wavelength can be used. In many situations it is preferred to incorporate optical sensors in a waveguide system, either fiber or integrated optics based. Compared to the use of free space beams this guided wave approach offers the potential advantages of:

- a better control of the light path, no alignment of the experimental setup is required
- evanescent field sensing, enabling the use of thin chemo-optical interfaces since large interaction lengths can be used
- the possibility of remote sensing by the use of a fiber network
- a higher mechanical stability
- a reduced size, weight and price

Waveguide based sensors compared to integrated optics are very cheap and have the strong advantage that they can be easily applied for distributed sensing. The sensor can be incorporated into the waveguide that transports the light from the source to the detector and the different sensors can be read out. Nevertheless, waveguide sensors can not compete with integrated optics with respect to:

- Robustness
- Compact optical circuitry, enabling a higher complexity (e.g. multiple sensors on one chip)
- Design flexibility with respect to the geometry as well as the choice and combination of materials (for example active and passive materials)
- Ease of access to the optical path in evanescent-field sensing
- Potential of integration with micro-electronics, micro-mechanics and micro total analysis systems
- Potential of 'cheap' batch-wise mass production
- Benefits from the developments in guided wave devices and microsystems in optical telecommunication

The degree of integration of a sensing scheme depends entirely on the intended application. Selection criteria will for example arise from the required sensitivity, selectivity, sensing environment, size or price. On one hand very sensitive sensing systems are known where only the sensing element is a planar waveguide and where the light from a bulk laser is coupled into and out off the waveguide by means of prism-, grating- or end-fire coupling. This type of devices will be very suitable for applications in e.g. medical laboratories. On the other hand, channel waveguide based sensors where the source, a phase modulator and a detector are monolithically integrated on the chip have been reported. Due to their small size and weight these sensors might be especially suitable for applications in e.g. space or micro total analysis systems. These two examples illustrate that there is no ultimate choice for using end-fire, butt-end, grating-, prism-, hybrid- or monolithically-coupled light sources or detectors, for the use of channel or slab waveguides, or for on- or off-chip modulation, referencing and signal processing [6]–[8].

1.7.1 Refractive chemical sensors

Refractive sensing is very important because of several reasons:

- Association of a limited number of receptor–target pairs only will accomplish useful changes of absorptive and luminescent properties while the refractive index will always change
- Most physically interesting sensor principles are of the refractive type

- Measuring absorption changes by an IO sensor does not differ in essence from that of the corresponding bulky methods [33]. Also, they are less sensitive and generally show a poor selectivity
- In luminescent sensors the luminescent properties of the sensitive material are sensitive to the analyte. Up to now in luminescent sensors the IO system has been used only for propagation of a mode of a wavelength suited to excite the luminescent particles [34]; the number of luminescent particles is derived from monitoring the free space emission. The low collection efficiency of a guided mode and the lack of efficient IO filters to effectively split the weak emitted mode from the intense excitation mode hamper a complete IO luminescence based sensor. Note that as a consequence of the fact that the exciting mode propagates parallel to the thin luminescent layer, the excitation power is used much more effectively than when using a perpendicularly incident free space excitation beam. Although not treated here in full detail, luminescence sensors are often applied because of their extremely high sensitivity.

The great majority of the refractive sensors rely on the induced changes of the effective refractive index N_{eff}. In order to get large effects the wave guiding structure in the sensing region has to be optimized to maximum partial sensitivity $\partial N_{eff}/\partial n_{sensitive\ layer}$. Various papers [35], [36] have been published on how to do so, resulting e.g. in maps in which all influences on the sensitivity can be represented by a pair of normalized parameters only. Sensitivities not only depend on the geometry, but also on the choice of materials. Out of the three technologies mentioned earlier the SiON technology can result in sensitivities close to 0.25, while the sensitivities of in-diffused glasses are an order of magnitude lower, mainly as a consequence of the low index contrast between the core and the substrate layer. However, by applying in the sensing region thin high index layers on top of the structures much higher sensitivities can be obtained. Sensitivities of polymer IO waveguides are in between. In special structures and special free standing waveguides $\partial N_{eff}/\partial n_{sensitive\ layer}$ values somewhat larger than unity can be obtained [37].

In chemical sensing the cross effect arises from the in-diffusion and the subsequent capture of the target units (molecules or ions) at receptor sites in a so-called chemo-optical material. This capture-based sensing is generally called affinity sensing. Essentially during the capture of target molecules by receptor molecules a small volume of gas or solution is replaced by the target molecules, while as a consequence of their chemical bond, also their electron distribution will be changed. Both effects together always result in a change of the refractive index; for a limited number of specific receptor–analyte pairs the association also accomplishes a useful change of the absorption in the visible / near infrared or of the luminescent properties. The larger the concentration of accessible receptors in the sensitive layer, the larger are the optical changes which can be obtained.

Generally, this chemically sensitive material is applied as a cladding layer within a window obtained by removing locally the originally applied cladding layer. This

sensitive material is probed by the evanescent field of the mode: evanescent field sensing. This configuration has several advantages:

Firstly, it affords in a natural way for the realization of general IO sensing platforms which later on can be provided with a specific cladding layer which enables the capture of the target units aimed at in the specific application. Also, if required, the sensitive layer can be easily removed making room for applying another one.

Secondly in-diffusion especially of large target molecules can be a slow process; hence to obtain acceptable response times the diffusion path has to be short as can be realized by using thin chemo-optical cladding layers.

Thirdly these thin layers can be very effectively probed by the evanescent field of a guided mode. Although only a part of the modal power experiences the change of the optical properties of the cladding, the interaction length is large, sometimes even on the order of magnitude of centimeters. So the effects on the light beam properties are much larger than in the case that the thin layer were interrogated by a perpendicularly incident free space beam, for then the interaction length would be equal to the thickness of the sensitive layer.

Generally the capture of the target molecules by receptors is part of a chemical equilibrium reaction and as a consequence the fraction of filled receptors will be an S-shaped function of the logarithm of the concentration of the target molecules in the environment as shown in figure (1-17). The concentration at which half of the receptors are filled can be derived to be the reciprocal of the association or affinity constant, K_{ass}, of the target–receptor pair. Hence, large affinity constants in principle allow for measurements in low-concentration ranges. This association constant is equal to the ratio of the association rate and the dissociation rate. In practice (e.g. at immunosensing) a high association constant mostly appears to imply a very low dissociation rate and as a consequence the fraction of filled receptors can follow only an increase of the concentration of analyte with a commonly acceptable time lag, but not a decrease.

Also materials with physical/chemical adsorption of analyte molecules can be applied; for example polymer layers with some porosity or gels. Here gelatin is mentioned, a material sensitive to relative humidity, and over the 100% R.H. range the corresponding change of the refractive index is about 0.055 [38].

When measuring the concentration of a chemical compound in a solution in the absence of other dissolved substances: for the refractive index or absorption of the solution is already a measure for the concentration. There are however several reasons to use also sensitive layers in these cases. Firstly as a result of the generally high association constants the concentration of the target molecules in the sensitive layer will be much larger than that in the solution; hence, such a sensitive layer generally strongly

enhances the effects. Secondly use of a sensitive layer enables the use of structures from which also some reference signals can be obtained by which e.g. the influence of temperature changes of the solution can be strongly reduced.

If several types of target molecules are solved all with unknown concentrations, an additional requirement of the receptors arises: they have to be selective, implying that they can associate with the target molecules only and hence that any association with other types of molecules is excluded. And in fact here one arrives at one of the weak points of all chemical sensors based on association: complete selectivity can never be reached. Nevertheless, if the nature of all types of target molecules in the solution is known it is sometimes possible to obtain data on all concentrations. If the structures of all other compounds differ strongly from that of the measurand, high specificity with respect to these other compounds is feasible. Also all concentrations may be determined by using sensor arrays, each sensor supporting a layer that shows different sensitivities to all present compounds, while these sensitivities are different for different layers. By application of neural networks or chemometric methods all concentrations can be derived from the primary sensor data. In this review these aspects will not be treated any further. For example it is left up to the chemists to develop useful receptors and adequate methods for immobilizing them in a matrix material, for attaching this material to the core layer of the sensor inside the sensing window and for regeneration of filled receptors.

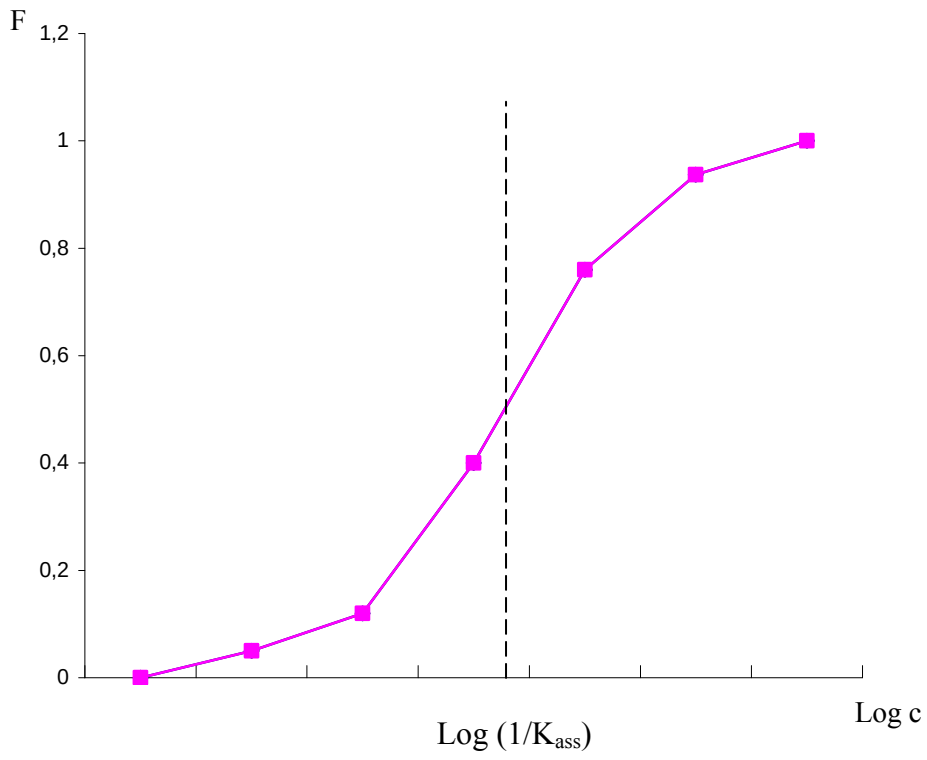

Figure (1-17): Fraction, F, of the sites which are associated with a target molecule as a function of the concentration, c, of the target molecules (K_{ass} is the affinity constant)

The response time of the sensor not only depends on the association rate but also on the time needed for the target molecules to reach the receptors (diffusion time). Under special conditions response times can be reduced appreciably by introducing kinetic measurements: not the equilibrium state is registered, but here it is sufficient to monitor the first part of the process in which the equilibrium state is reached only.

In so-called direct sensing only, the target molecules are identical to the analyte molecules. In this operation mode in principle continuous measurements are feasible and it is very effective for e.g. an alarm sensor. In indirect sensing mostly either analyte or receptor molecules are applied which are provided with optical labels.

It may be clear that these indirect formats do not allow for continuous measurements and after each measurement the receptors have to be emptied completely by adding appropriate regenerating solutions. Another drawback is the consumption of expensive labeled molecules, while also auxiliary facilities have to be added to the sensing system for providing and mixing several solutions. However their sensitivity is generally greater than obtained by direct sensing methods and both indirect formats are often applied in applications where a concentration has to be measured only once, e.g. in immunosensing. Most markets prefer application of rapid label-free methods [39] provided that their resolution is sufficient for the specific application. And in fact obtaining the high resolutions (and hence the low detection limits) required for direct assays at acceptable response times is one of the main challenges for refractive type IO sensors.

With respect to the thickness of the sensitive cladding layer one can define two extremes: in the first one the sensitive layer is thick enough that the power of the evanescent field outside the sensitive layer can be neglected; the sensor is insensitive to the refractive index of the solution and one speaks about homogeneous or bulk sensing. At the other extreme the sensitive cladding is very thin, in the limit being a monomolecular layer only; in good approximation the modal field is constant over the whole of the thickness. Association can result in both an increased average thickness of the layer and a change of its refractive index. In practice both effects can be taken into account simultaneously by approaching the effects as arising from a change of the effective thickness of the layer only. In surface sensing the N_{eff}-value is also sensitive to the refractive index of the solution and it will also experience influence of non-specific adsorption of other substances on the sensitive layer. Application of reference windows can (sometimes partly) compensate for these disturbing effects.

Optical environment sensors have recently become a fast-expanding technology where the change of the phase shift is converted into a variation of intensity. The main focus of this research is to demonstrate a chemical sensor, particularly as a sensor of gaseous species such as ammonia.

1.8 Ammonia sensors

Ammonia is widely used in the production of explosives, fertilizers and as an industrial coolant. The toxic qualities of this gas are well documented, and acute poisoning can result from inhalation of only small doses of ammonia vapor. Exposure limits of 25 ppm over an 8 h period and 35 ppm over a 10 min period have been recommended and have recently been legislated for.

Locations employing industrially sized cooling systems, such as food production and storage plants, report a number of exposure incidents every year. As industry is becoming increasingly safety conscious, efficient sensor devices to monitor personal exposure of workers undertaking any risk of contact with ammonia are desirable, as rapid evacuation of personnel from contaminated areas may be all that is required to prevent serious illness.

In the field of air quality monitoring, a wide variety of instrumentation can be employed for ammonia analysis. Devices employing spectroscopic or electrochemical methods are usually very accurate, sensitive and selective. However, they are also expensive, static instruments and requiring the presence of an experienced operator. Simpler detector systems based on the semiconductivity of SnO_2 thin films do exist for monitoring ammonia leakage in the working environment, and have been commercialized as personal monitoring systems. However, these devices come at a much higher cost, are not selective towards ammonia and display a restricted active sensor lifetime.

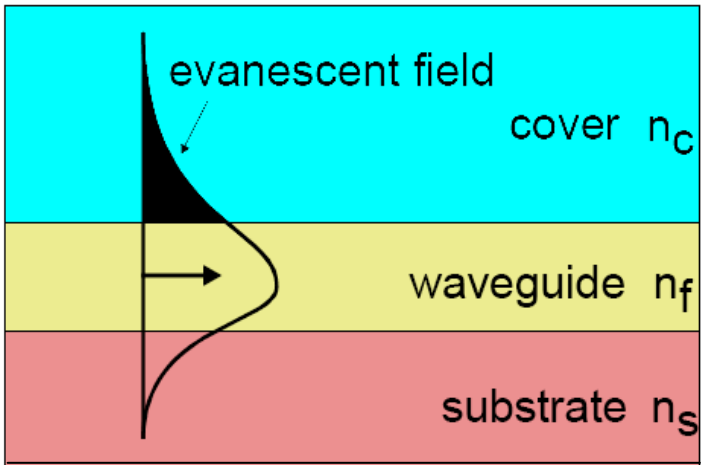

Figure (1-18): Evanescent field penetrates the cover layer

Recently a miniaturized electrochemical sensor device has become available for ammonia detection. This device uses interchangeable sensor heads biased towards detection of a specific gas, with the added requirement of peripheral filters to achieve

effective selectivity towards ammonia. A different approach can be applied when considering a dedicated ammonia sensor, which similarly takes advantage of miniaturized, low power components and selective response to ammonia in the required range. Optochemical transduction is a way to develop a non-consumptive, compact ammonia sensor device with low power demand that could be used for in real-time analysis.

A variety of optical electrode devices have been used that utilize the reaction of dissolved ammonia vapor with a pH-dependent dye material, which undergoes a suitable colour change [40]. In general, these are based on monitoring the absorption or fluorescence characteristics of indicator dyes entrapped within a membrane deposited onto a waveguide substrate. Ammonia interacts with the immobilized indicator, resulting in changes in absorbance or emission spectra, which are monitored using a suitable detector module via an optical fiber or planar waveguide. Evanescent wave absorption is an effective technique for performing such analysis. Light energy associated with the guided mode penetrates into a coating of lower refractive index than the substrate as shown in figure (1-18). This evanescent field is able to interact with dye materials contained within the coating. When there is a change in the optical characteristics of the outer medium (refractive index change), a modification of the optical properties of the guided mode is induced via the evanescent field and this can be detected by MZI.

In the Mach-Zehnder interferometer (MZI) shown in figure (1-19), the incoming coherent light wave is equally split into two channels, and after a certain distance of propagation, the waves from both channels are recombined together. One of the channels [the phase-modulating arm (sensing arm for sensing applications)] is exposed to the outer medium for a certain distance L (interaction length), while the other channel (the reference arm) is isolated from the medium. During this distance, the wave in the phase-modulating arm will experience a phase shift with respect to the wave in the reference arm. At the output port, light coming from both channels will interfere and show a sinusoidal variation corresponding to the accumulated phase difference, which is related to the change of the refractive index of the surrounding medium.

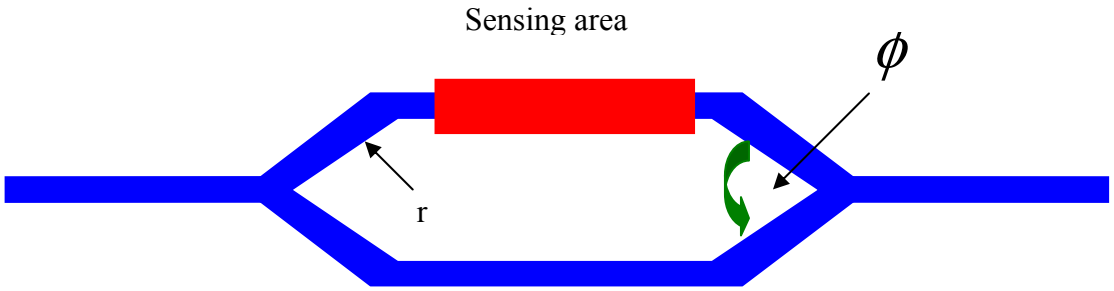

Figure (1-19): Mach-Zehnder interferometer

2 Theoretical considerations

2.1 Introduction

Optical devices based on integrated waveguides are crucial for the future development of optical communication systems. In recent years, growing attention has been paid to silicon based dielectrics such as silicon oxides, nitrides, and oxynitrides as potential materials for integrated optics [41].

There is also a growing need for sensitive chemical sensors in areas such as process technology, health care, environmental control, biotechnology, etc. For many applications these sensors should show a high resolution over a wide dynamic range, they should be very sensitive, selective, fast, small and cheap, and should be suited for remote sensing. An attractive option fulfilling all these requirements is offered by integrated optical (IO) sensors. In these optical chips the chemical parameter to be sensed, the measurand, influences the sensing region directly or by means of a chemo-optical transduction layer the propagation properties of a guided light propagating through the chip. Using appropriate optical circuitry, these changes of propagation properties can be converted into a change of the optical output power. In turn, this is measured using a photo detector and appropriate electronics.

Generally, selectivity is provided by the chemo-optical transduction layer, alternatively called sensitive layer. This layer contains receptor units that are selectively associated with the chemical entities of the measurand. In addition, this layer can concentrate the measurand molecules and enhance the optical effects of their presence.

Mostly the relevant changes of optical parameters occur in a region just outside the core layer of the waveguide, the evanescent field region. Hence, such chemical IO sensors are often called evanescent field sensors. The changing optical parameters are the refractive index (n), the absorption coefficient and luminescence parameters.

The interferometric sensors are generally supposed to have the highest sensitivity potential. This is mainly based on the possibility of using large interaction length values resulting in an enhanced sensitivity. Amongst the interferometric sensors it is only the MZI sensor that contains an easily accessible reference arm. When used properly, this reference arm can make the sensor (nearly) insensitive to many perturbing effects. The large intrinsic stability results in an improved sensor resolution, making the MZI sensor very attractive. The next task is to design an optical waveguide based chemical sensor and a heater which will be used to increase the sensitivity of the sensor.

2.2 Waveguide design

Chemical sensors are the non-communication application field where integrated optic technology is expected to play an increasing role and where it is already successful commercially. The sensing in the waveguide is performed by the evanescent tail of the modal field in the cover medium. This sensing operation consists of measuring the change of the effective index of a propagating mode when a change of the refractive index takes place in the waveguide cover. The waveguide characteristic equation or/and a calibration allows the retrieval of the index change from the measured change of the effective index. The sensitivity of the measurement of the physical or chemical quantity present in the cover depends on the strength and the distribution of the evanescent field in the cover. The main design task is therefore to find the monomode waveguide structure which maximizes the sensitivity on the quantity to be measured [42].

In the case of the rib waveguide, the geometrical parameters of the waveguide section shown in figure (2-1) are chosen in order to fulfill the monomode propagation condition. This can be achieved if the geometry of the waveguide fulfils the following relationship using the effective index method (EIM) [43].

$$t < \mathrm{c} + \frac{\mathrm{r}}{\sqrt{1 - \mathrm{r}^2}} \tag{2-1}$$

where:

$$t = \frac{w_{eff}}{H_{eff}}, \qquad r = \frac{h_{eff}}{H_{eff}},$$

$$h_{eff} = h + q, \qquad H_{eff} = H + q,$$

$$w_{eff} = w + \frac{2B_c}{k\sqrt{n_f^{\,2} - n_c^{\,2}}}, \tag{2-2}$$

$$q = \frac{B_c}{k\sqrt{n_f^{\,2} - n_c^{\,2}}} + \frac{B_s}{k\sqrt{n_f^{\,2} - n_s^{\,2}}}, \tag{2-3}$$

n_f , n_s and n_c are refractive indices of the guiding region, the substrate and the cover, respectively.

$B_{c,s} = 1$ for TE modes and $\left(\frac{n_{c,s}}{n_f}\right)^2$ for TM modes, $k = \frac{2\pi}{\lambda}$, λ is the wavelength. The factor c can be either 0 or 0.3.

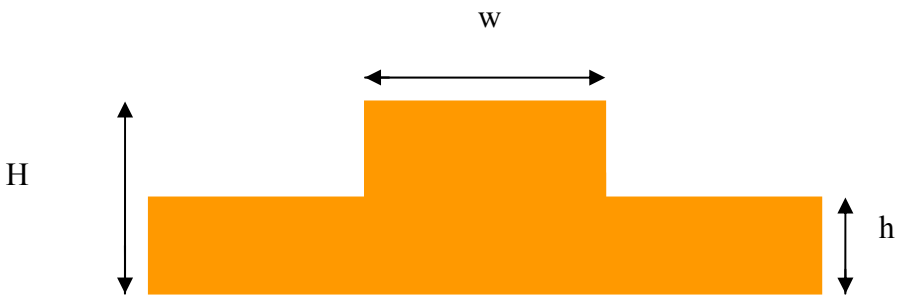

Figure (2-1): Schematic of a rib waveguide

The results of the calculations using core refractive index 1.55 are given graphically in figure (2-2). In the region below the line the structure is monomode. It is evident that according to the theory, the waveguide width is more critical parameter than the rib height.

At present, the beam propagation method (BPM) is the most widely used for the study of light propagation in waveguides and therefore it is used to calculate the thickness of the different layers. Nowadays, there are a great number of versions of BPM [44]-[48]; BPM based on the finite difference method (FD-BPM), BPM based on the fast Fourier transform (FFT-BPM), BPM based on the McKee-Mitchell Scheme and BPM based on the finite element method (FE-BPM). Especially, FE-BPM is superior to FFT-BPM in the sense that the former can be applied to strongly guiding waveguides and strongly polarization dependent waveguides. In addition, FE-BPM can arbitrarily select the order and the number of elements, depending on the required computational accuracy.

Recently, the so-called imaginary distance beam propagation method (ID-BPM) [49] has been reported as an analysis method of eigenmodes which in it the propagation direction is selected along the imaginary axis, and selecting the appropriate propagation step size, we can extract the specific eigenmode from the initial input field expressed by arbitrarily superposing the eigenmodes. The main advantages of the ID-BPM as an eigenmode solver are as follows:

- High-efficient calculation algorithms developed for the BPM analysis can be directly utilized

- Matrices derived from the BPM formulation are essentially complex, hence, lossy optical waveguides can be easily treated with no additional effort
- Eigenmodes can be obtained successively from the fundamental to higher order modes
- Employing the appropriate boundary conditions, not only guided modes but also leaky modes may be treated

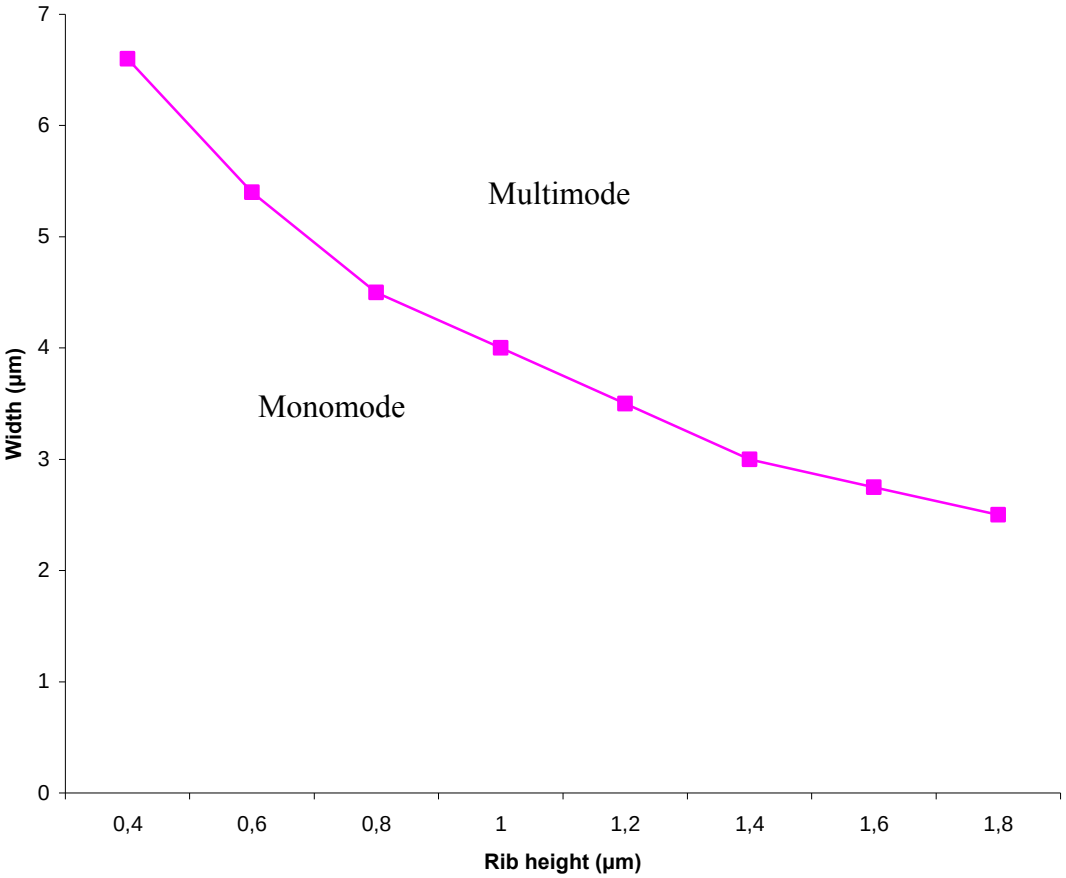

Figure (2-2): Monomode condition for SiON waveguide

Here, in order to treat leaky modes, the perfectly matched layer (PML) boundary condition, the validity of which has been already confirmed in the real distance beam propagation method, are employed as boundary conditions for artificial boundaries.

A 3-D optical waveguide surrounded by PML regions I, II, and III with thickness as shown in figure (2-3) is considered, where x and y are the transverse directions, z is the propagation direction, PML regions I and II are faced with the x and y directions, respectively, region III corresponds to the four corners, and W_x and W_y are the computational window sizes along the x and y directions, respectively.

Using the transversely scaled version of PML [49], Maxwell's equations can be written as:

$$\nabla \times H = j\omega\xi_0 n^2 sE\,, \tag{2-4}$$

and

$$\nabla \times E = -j\omega\mu_0 sH \tag{2-5}$$

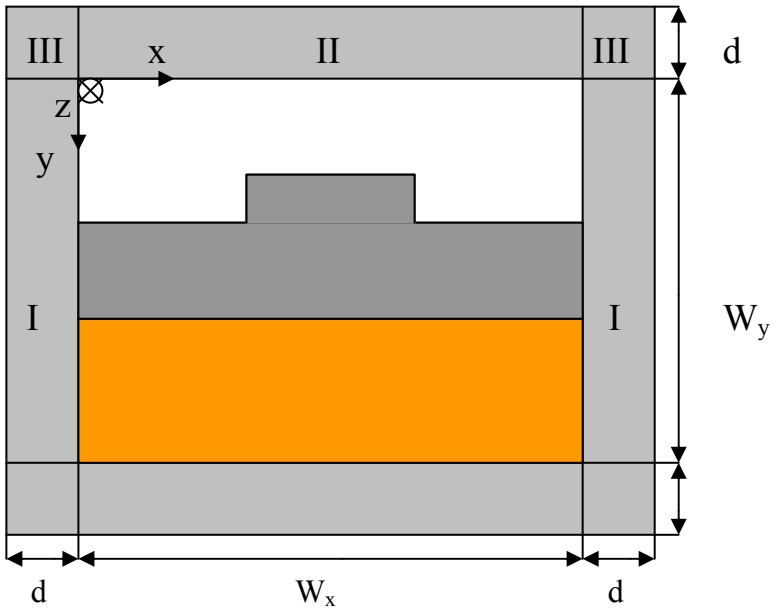

Figure (2-3): Optical waveguide is surrounded by PML regions

where,

$$\nabla = i_x s_x \frac{\partial}{\partial x} + i_y s_y \frac{\partial}{\partial y} + i_z s \frac{\partial}{\partial z}\,, \tag{2-6}$$

where i_x, i_y, and i_z are the unit vectors in the x, y and z directions, respectively, and the values of s_x and s_y are summarized in table (2-1).

Region	s_x	s_y
I	1	s
II	s	1
III	1	1

Table (2-1): The definition of s_x and s_y

with:

$$s = 1 - j\frac{\sigma_e}{\omega\xi_0 n^2} = 1 - j\frac{\sigma_m}{\omega\mu_0} \tag{2-7}$$

where:

E and H are the electric and the magnetic field vectors, respectively,

ω is the angular frequency,

ξ_0 and μ_0 are the permittivity and the permeability of free space, respectively,

n is the refractive index and

σ_e and σ_m are the electric and the magnetic conductivities of PML, respectively.

The relation (2-7) is required to satisfy the PML impedance matching condition:

$$\frac{\sigma_e}{\xi_0 n^2} = \frac{\sigma_m}{\mu_0} \tag{2-8}$$

which means that the wave impedance of a PML medium exactly equals that of the adjacent medium with refractive index n in the computational window:

$$\sqrt{\frac{\mu_0}{\xi_0 n^2}},$$

Regardless of the angle of propagation or frequency. In the PML medium, we assume a q–power profile of the electric conductivity as:

$$\sigma_e = \sigma_{\max}\left(\frac{\rho}{d}\right)^q \tag{2-9}$$

where ρ is the distance from the beginning of PML. Using the theoretical reflection coefficient R at the interface between the computational window and the PML medium:

$$R = \exp\left[-2\frac{\sigma_{\max}}{\xi_0 cn}\int_0^d\left(\frac{\rho}{d}\right)^q d\rho\right] \tag{2-10}$$

The maximum conductivity $\sigma_{\max}$ can be determined as:

$$\sigma_{\max} = \left(\frac{q+1}{2}\right)\left(\frac{\xi_0 cn}{d}\right)\ln\frac{1}{R} \tag{2-11}$$

where c is the light velocity of free space. Usually, a parabolic profile is assumed for the conductivity, q = 2, and thus, s in (2-4) and (2-5) is finally written as:

$$s = 1 - j\frac{3\lambda}{4\pi nd}\left(\frac{\rho}{d}\right)^2\ln\frac{1}{R}, \qquad \text{in the non-PML region}$$

s = 1, in the PML region

where $\lambda = \dfrac{2\pi c}{\omega}$ is the free-space wavelength.

Under the scalar approximation, from (2-4) and (2-5) the following basic equation can be obtained:

$$s_x\frac{\partial}{\partial x}\left(p\frac{s_x}{s}\frac{\partial\Phi}{\partial x}\right) + s_y\frac{\partial}{\partial y}\left(p\frac{s_y}{s}\frac{\partial\Phi}{\partial y}\right) + s\frac{\partial}{\partial z}\left(p\frac{\partial\Phi}{\partial z}\right) + k_0{}^2 gs\Phi = 0 \tag{2-12}$$

where k_0 is the free space wavenumber, and Φ, p and g are given by:

$\Phi = E_x$, $p = 1$ and $g = n^2$ for quasi-TE modes and

$\Phi = H_x$, $p = 1 / n^2$ and $g = 1$ for quasi-TM modes.

substituting a solution of the form:

$$\Phi(x,y,z) = \Psi(x,y,z)\exp(-jk_0 n_0 z) \tag{2-13}$$

into (2-12), and assuming Fresnel approximation, the following beam propagation equation for the varying complex amplitude Ψ can be obtained:

$$-2jk_0 n_0 ps\frac{\partial \Psi}{\partial z} + s_x \frac{\partial}{\partial x}\left(p\frac{s_x}{s}\frac{\partial \Psi}{\partial x}\right) + s_y \frac{\partial}{\partial y}\left(p\frac{s_y}{s}\frac{\partial \Psi}{\partial y}\right) + k_0{}^2 s\left(g - n_0{}^2 p\right)\Psi = 0 \tag{2-14}$$

where n_0 is the reference refractive index.

By solving the last equation the effective index of the desired mode can be calculated, and then the field distribution and effective index of the fundamental mode are obtained. The value of reference refractive index, n_0 may be arbitrarily chosen.

This was one mathematical way to design a monomode optical waveguide, and now the design task will be transferred to find the waveguide structure which maximizes the sensitivity on the quantity to be measured.

Figure (2-4) is representing a slab waveguide refractometric sensor in which the measurand is homogeneously distributed in the cover (homogeneous sensing) and assuming that the cover medium is a fluid, which implies that the contact zone between the cover and the waveguide is of zero thickness.

Evanescent wave sensing of a chemical quantity which is homogeneously distributed in the waveguide cover refers to a different electromagnetic condition. The sensitivity is now related to the integral of the squared evanescent field in the cover material. A waveguide refractometric sensor can be used in liquid concentration monitoring, for measuring traces of chemicals by means of a thick selective membrane and, more generally, for measuring all chemical quantities whose variation corresponds to a change of refractive index.

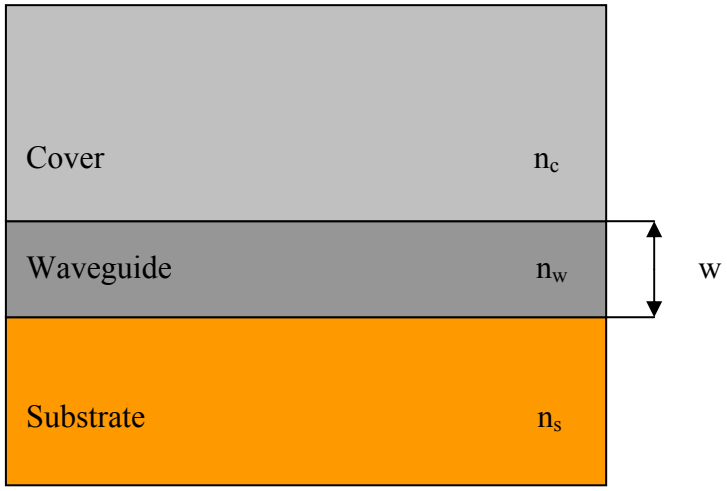

Figure (2-4): Schematic representation of a slab waveguide refractometric sensor

The sensing operation consists of the measurement of changes of the real or imaginary part of the effective refractive index caused by measurand-induced changes of the refractive index of the cladding. Hence, the sensitivity is defined as the ratio of the effective index change of the guided mode to the refractive index change of the core layer environment, i.e., both cladding and substrate. This ratio is 1 for a free-space beam.

Nevertheless, for practical application the sensitivity should be as high as possible and therefore the waveguide parameters should be chosen with care.

where:

$\varepsilon_{eff} = N_{eff}^{\ 2}$, $\varepsilon_c = n_c^{\ 2}$, $\varepsilon_s = n_s^{\ 2}$, and $\varepsilon_w = n_w^{\ 2}$

where ε_{eff}, ε_c, ε_s and ε_w are the effective, cover, substrate and waveguide permittivities respectively.

N_{eff}, n_c, n_s and n_w are the effective, cover, substrate and waveguide indices respectively.

By starting the analysis with the well-known characteristic equation for a three-layer slab waveguide [50]:

$$\frac{2\pi w}{\lambda}\sqrt{n_w{}^2 - N_{eff}{}^2} - \arctan\left[\sqrt{\frac{N_{eff}{}^2 - n_s{}^2}{n_w{}^2 - N_{eff}{}^2}}\left(\frac{n_w}{n_s}\right)^{2p}\right] -$$
$$\arctan\left[\sqrt{\frac{N_{eff}{}^2 - n_c{}^2}{n_w{}^2 - N_{eff}{}^2}}\left(\frac{n_w}{n_c}\right)^{2p}\right] - m\pi = 0 \qquad (2\text{-}15)$$

where w is the thickness of the waveguide core layer, and m is an integer defining the mode order, p = 0 for TE- and p = 1 for TM-polarization while λ is the free-space wavelength.

Let:

$$x_s = \sqrt{\frac{N_{eff}{}^2 - n_s{}^2}{n_w{}^2 - N_{eff}{}^2}} \quad , \quad x_c = \sqrt{\frac{N_{eff}{}^2 - n_c{}^2}{n_w{}^2 - N_{eff}{}^2}} \qquad (2\text{-}16)$$

and

$$\alpha_s = \frac{n_w{}^2}{n_s{}^2} \quad , \quad \alpha_c = \frac{n_w{}^2}{n_c{}^2} \qquad (2\text{-}17)$$

by using equations (2-16) and (2-17), equation (2-15) can be rewritten in a more normalized form:

$$\frac{2\pi w n_w}{\lambda}\sqrt{\frac{1-\frac{1}{\alpha_s}}{1+x_s{}^2}} - \arctan\alpha_s x_s - \arctan\alpha_c x_c - m\pi = 0 \qquad (2\text{-}18)$$

with $\alpha_s = \alpha_c = 1$ for TE modes.

The sensitivity S of homogeneous sensing is defined as the rate of change of the modal effective index N_{eff} with respect to the change in the cover index n_c.

$$S = \frac{\partial N_{eff}}{\partial n_c} = \left(\frac{\partial n_c}{\partial N_{eff}}\right)^{-1} \quad , \qquad (2\text{-}19)$$

$$S_{TE} = \sqrt{\frac{1}{\alpha_c}}\{x_c\sqrt{1+x_c^{\,2}}\sqrt{\frac{1}{\alpha_c}+x_c^{\,2}}$$

$$\left[\frac{1}{x_c}+\frac{1}{x_s}+\arctan x_s+\arctan x_c+m\pi\right]\}^{-1} \tag{2-20}$$

and,

$$S_{TM} = \frac{\dfrac{2}{\sqrt{\dfrac{1+x_s^{\,2}}{\alpha_c\left(\dfrac{1}{\alpha_s}+x_s^{\,2}\right)}}} - \sqrt{\dfrac{1+x_s^{\,2}}{\alpha_c\left(\dfrac{1}{\alpha_s}+x_s^{\,2}\right)}}}{1+x_c^{\,2}+\alpha_c x_c\left(\dfrac{1}{\alpha_c^{\,2}}+x_c^{\,2}\right)\beta} \tag{2-21}$$

where:

$$\beta = \left[\arctan\alpha_s x_s+\arctan\alpha_c x_c+m\pi+\left(\frac{1+x_s^{\,2}}{\alpha_s x_s\left(\dfrac{1}{\alpha_s^{\,2}}+x_s^{\,2}\right)}\right)\right] \tag{2-22}$$

Searching for the condition of the maximum sensitivity in a structure of constant n_w, n_s and n_c amounts one can get the exact maximum condition after some mathematical operations:

for TE modes:

$$\left[\frac{1}{x_c}+\frac{1}{x_s}+\arctan x_c+\arctan x_s+m\pi\right]\left[\frac{1}{x_c^{\,2}}+3+\frac{1-\dfrac{1}{\alpha_s}}{\dfrac{1}{\alpha_s}+x_s^{\,2}}\right]=\frac{1}{x_c^{\,3}}+\frac{1}{x_s^{\,3}} \tag{2-23}$$

and for TM modes:

$$\left(1+x_c^{\,2}+r\beta\right)\left[\frac{2x_s\left(1-\frac{1}{\alpha_s}\right)}{\theta\left(\frac{1}{\alpha_s}+x_s^{\,2}\right)^2}\left(\frac{\frac{1}{\alpha_s}+x_s^{\,2}}{1+x_s^{\,2}}+\frac{1}{2\alpha_c}\right)\right]-\left(\frac{2}{\theta}-\theta\right)$$

$$\left[2x_c t+\beta\alpha_c t\left(\frac{1}{\alpha_c^{\,2}}+3x_c^{\,2}\right)+r\left[\frac{1}{\alpha_s\left(\frac{1}{\alpha_s^{\,2}}+x_s^{\,2}\right)}+\frac{t}{\alpha_c\left(\frac{1}{\alpha_c^{\,2}}+x_c^{\,2}\right)}+\frac{\gamma}{\alpha_s}\right]\right]=0 \tag{2-24}$$

where:

$$r=x_c\alpha_c\left(\frac{1}{\alpha_c^{\,2}}+x_c^{\,2}\right) \tag{2-25}$$

$$t=\frac{1-\frac{x_s}{\alpha_c}}{1-\frac{x_c}{\alpha_s}} \tag{2-26}$$

$$\theta=\sqrt{\frac{1+x_s^{\,2}}{\alpha_c\left(\frac{1}{\alpha_s}+x_s^{\,2}\right)}} \tag{2-27}$$

$$\gamma=\frac{2x_s^{\,2}\left(\frac{1}{\alpha_s^{\,2}}+x_s^{\,2}\right)-\left(1+x_s^{\,2}\right)\left(\frac{1}{\alpha_s^{\,2}}+3x_s^{\,2}\right)}{x_s^{\,2}\left(\frac{1}{\alpha_s^{\,2}}+x_s^{\,2}\right)^2} \tag{2-28}$$

The normalized waveguide thickness achieving maximum sensitivity can be obtained by substituting the x_s solutions of equations (2-23), (2-24) into the characteristic equation (2-18) of the three layer structure for TE_0 and TM_0 modes:

$$\frac{n_w w}{\lambda} = \frac{1}{2\pi}\sqrt{\frac{1+x_s^{\,2}}{1-\frac{1}{\alpha_s}}}\left[\arctan\alpha_s x_s + \arctan\alpha_c x_c\right] \tag{2-29}$$

In the case of surface sensing the measurand in the slab waveguide refractometric sensor is an ultrathin film at the waveguide-cover interface as shown in figure (2-5). The sensitivity in surface sensing is related to the squared field magnitude at the waveguide-cover interface [50].

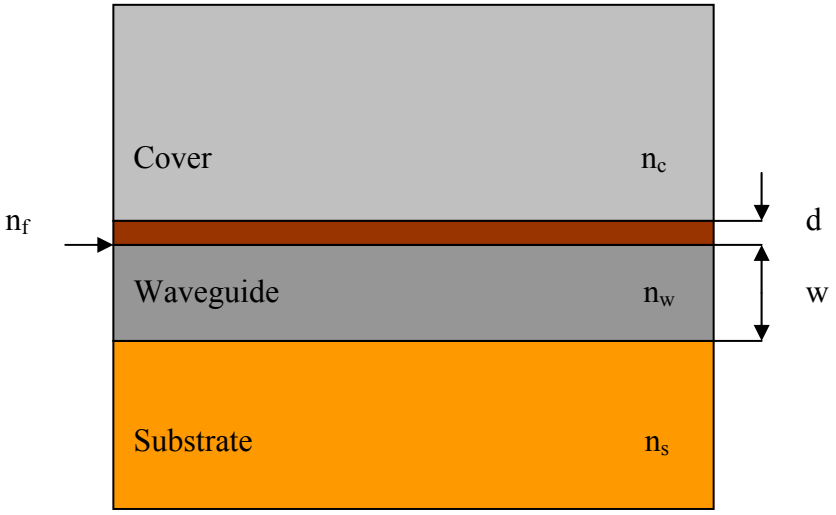

Figure (2-5): Schematic representation of a surface sensor

By starting the analysis with the normalized characteristic equation for the surface sensing case:

$$\frac{2\pi w n_w}{\lambda}\sqrt{\frac{1-\frac{1}{\alpha_s}}{1+x_s^{\,2}}} - \arctan\alpha_s x_s - \arctan\alpha_c\left(1-\delta\right)x_c - m\pi = 0 \tag{2-30}$$

where for TE modes:

$$\delta = \frac{2\pi}{\lambda} d\left(\varepsilon_f - \varepsilon_c\right) \tag{2-31}$$

and for TM modes:

$$\delta = \frac{2\pi}{\lambda} d\left(\varepsilon_f - \varepsilon_c\right) \frac{\varepsilon_{eff}\left(\frac{1}{\varepsilon_c} + \frac{1}{\varepsilon_f}\right) - 1}{\sqrt{\varepsilon_{eff} - \varepsilon_c}} \tag{2-32}$$

The sensitivity S of a surface sensing structure is defined as the rate of change of the model effective index N_{eff} with respect to the dielectric load term that is defined as:

$$\eta = \frac{2\pi}{\lambda} d\left(\varepsilon_f - \varepsilon_c\right) \quad , \tag{2-33}$$

$$S = \frac{\partial N_{eff}}{\partial \eta} = \left(\frac{\partial \eta}{\partial N_{eff}}\right)^{-1}, \tag{2-34}$$

$$S_{TE} = \frac{\sqrt{1 - \frac{1}{\alpha_s}}}{\sqrt{\frac{1}{\alpha_s} + x_s^{\,2}}\left(1 + x_c^{\,2}\right)\left[\arctan x_s + \arctan x_c + m\pi + \frac{1}{x_c} + \frac{1}{x_s}\right]}, \tag{2-35}$$

and

$$S_{TM} = \frac{\left(p\frac{x_c^{\,2} + \frac{1}{\alpha_c}}{1 + x_c^{\,2}} - 1\right)\left(\frac{1}{\frac{1}{\alpha_c} + \alpha_c x_c^{\,2}}\right)\sqrt{\frac{1 - \frac{1}{\alpha_c}}{\frac{1}{\alpha_c} + x_c^{\,2}}}}{\vartheta} \tag{2-36}$$

where:

$$\vartheta = \arctan \alpha_s x_s + \arctan \alpha_c x_c + m\pi + \frac{\left(1 + x_s^{\,2}\right)}{\alpha_s x_s\left(\frac{1}{\alpha_s^{\,2}} + x_s^{\,2}\right)} + \frac{\left(1 + x_c^{\,2}\right)}{\alpha_c x_c\left(\frac{1}{\alpha_c^{\,2}} + x_c^{\,2}\right)} \tag{2-37}$$

and,

$$p = \frac{\varepsilon_w}{n_f^{\,2}} + \alpha_c \tag{2-38}$$

For maximum surface sensitivity for TE modes:

$$\left[\arctan x_c + \arctan x_s + m\pi + \frac{1}{x_c} + \frac{1}{x_s}\right]\left(3 + \frac{1 - \frac{1}{\alpha_s}}{\frac{1}{\alpha_s} + x_s^{\,2}}\right) - \frac{1}{x_c^{\,3}} - \frac{1}{x_s^{\,3}} = 0 \tag{2-39}$$

and for TM modes:

$$\left(p\,\frac{\frac{1}{\alpha_s} + x_s^{\,2}}{1 + x_s^{\,2}} - 1\right)\left\{\left(\frac{1 - \frac{1}{\alpha_c}}{1 - \frac{1}{\alpha_s}}\right) x_s\left[\frac{1}{x_c}\left(2 - \frac{1}{x_c^{\,2}}\right) + 2\Gamma\alpha_c\right] + \frac{\alpha_c\left(\frac{1}{\alpha_c^{\,2}} + x_c^{\,2}\right)}{\alpha_s x_s^{\,2}\left(\frac{1}{\alpha_s^{\,2}} + x_s^{\,2}\right)^2}\left(\frac{2x_s^{\,2}}{\alpha_s^{\,2}} - 3x_s^{\,2} - \frac{1}{\alpha_s^{\,2}}\right)\right\} - x_s.$$

$$\left[\frac{1}{\frac{1}{\alpha_s} + x_s^{\,2}} + \frac{p\left(1 - \frac{2}{\alpha_s} - x_s^{\,2}\right)}{\left(1 + x_s^{\,2}\right)^2}\right]\left(\frac{1}{\alpha_c^{\,2}} + x_c^{\,2}\right)\vartheta\alpha_c = 0 \tag{2-40}$$

where,

$$\Gamma = \vartheta - \frac{1}{x_c\alpha_c}\left(\frac{1 + x_c^{\,2}}{\frac{1}{\alpha_c^{\,2}} + x_c^{\,2}}\right) \tag{2-41}$$

The normalized waveguide thickness achieving maximum sensitivity can be obtained as before in the homogeneous sensitivity:

$$\frac{n_w w}{\lambda} = \frac{1}{2\pi}\sqrt{\frac{1+x_s^{\,2}}{1-\frac{1}{\alpha_s}}}\left[\arctan\alpha_s x_s + \arctan\alpha_c x_c\right] \tag{2-42}$$

By taking all considerations above into account during the design of a monomode waveguide which operates with signal wavelength 633 nm (in the visible range) the strip-loaded waveguide shown in figure (2-6) was designed.

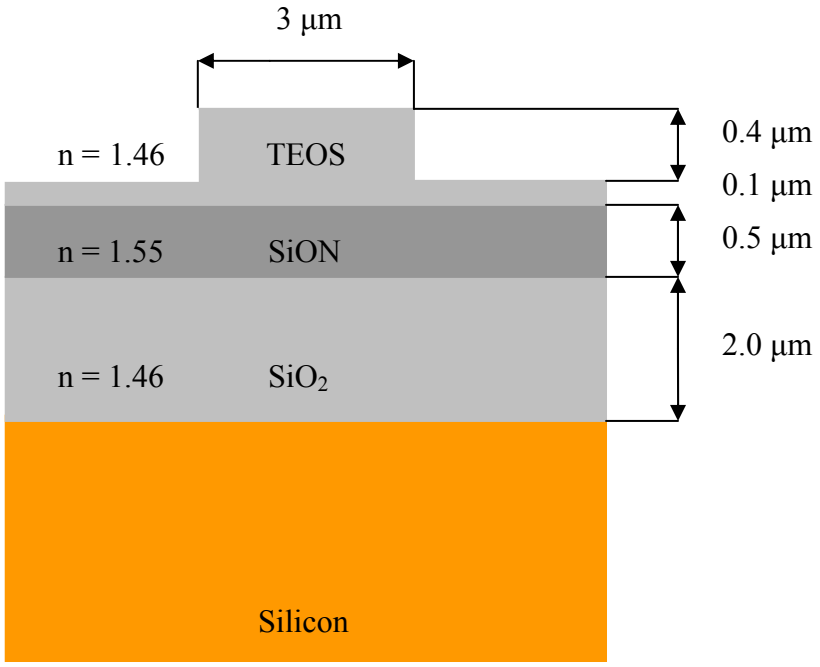

Figure (2-6): Schematic cross section and target design parameter of a strip-loaded waveguide

2.3 Design of Mach–Zehnder interferometer (MZI)

The Mach–Zehnder interferometer (MZI) is one of the work-horses in the field of IO chemical sensors. On the one hand because of its performance and on the other hand because it is relatively simple to implement its basic structure in integrated optics and to provide it with a chemo-optical interface layer. And indeed many papers have been published in which it is shown that an IO MZI loaded with a certain type of interface enables the determination of low concentrations of certain chemicals.

The IO MZI sensor will be treated in greater detail in order to illustrate the approach which is needed to develop stable, reproducible IO chemical sensing systems

with high resolution and low detection limit, for the market demands of applications such as determining contaminant concentrations in food or protein concentrations in health care. First the principle of the IO MZI sensor will be explained. Next an approach will be given for arriving at an MZI implementation, which shows a very high resolution of the refractive index measurement and finally some other interesting MZI implementations will be discussed.

The structure of the IO MZI consisting of two monomode waveguides is given in figure (2-7) [51]. At the input side the mode is excited by coherent monochromatic light from e.g. a fiber. Next the modal power P_{in} is equally divided into two parallel branches by a Y-splitter, and after traveling these branches the branches merge again at a second Y-junction, where the modes from both waveguides interfere with each other. Their phase difference, $\Delta\varphi$, defines the power of the mode in the output waveguide P_{out}.

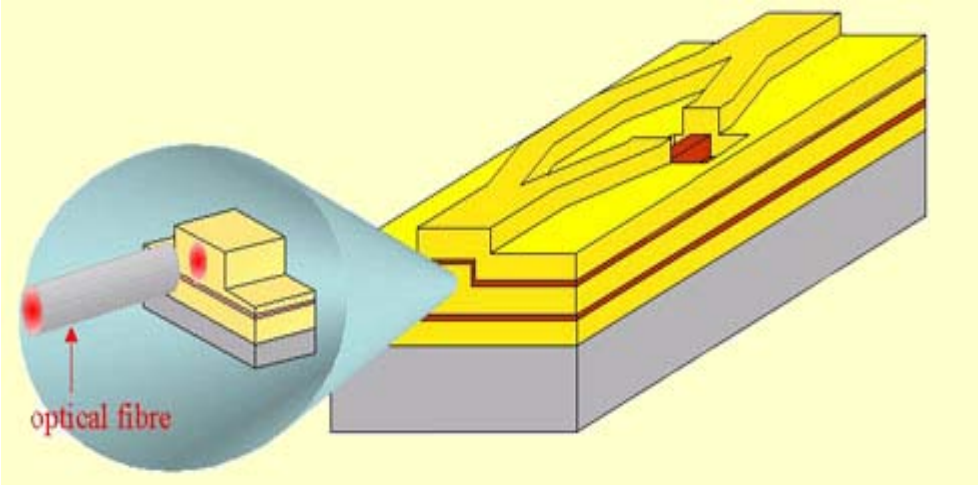

Figure (2-7): Mach – Zehnder interferometer (MZI) [51].

Assuming a lossless MZI device with symmetrical Y-junctions it can be derived that:

$$P_{out} / P_{in} = (1 / 2) (1 + \cos \Delta\varphi) \qquad (2\text{-}43)$$

Using the previous equation, the transfer function of the MZI, i.e., the power ratio P_{out} / P_{in}, is depicted as a function of $\Delta\varphi$ in figure (2-8).

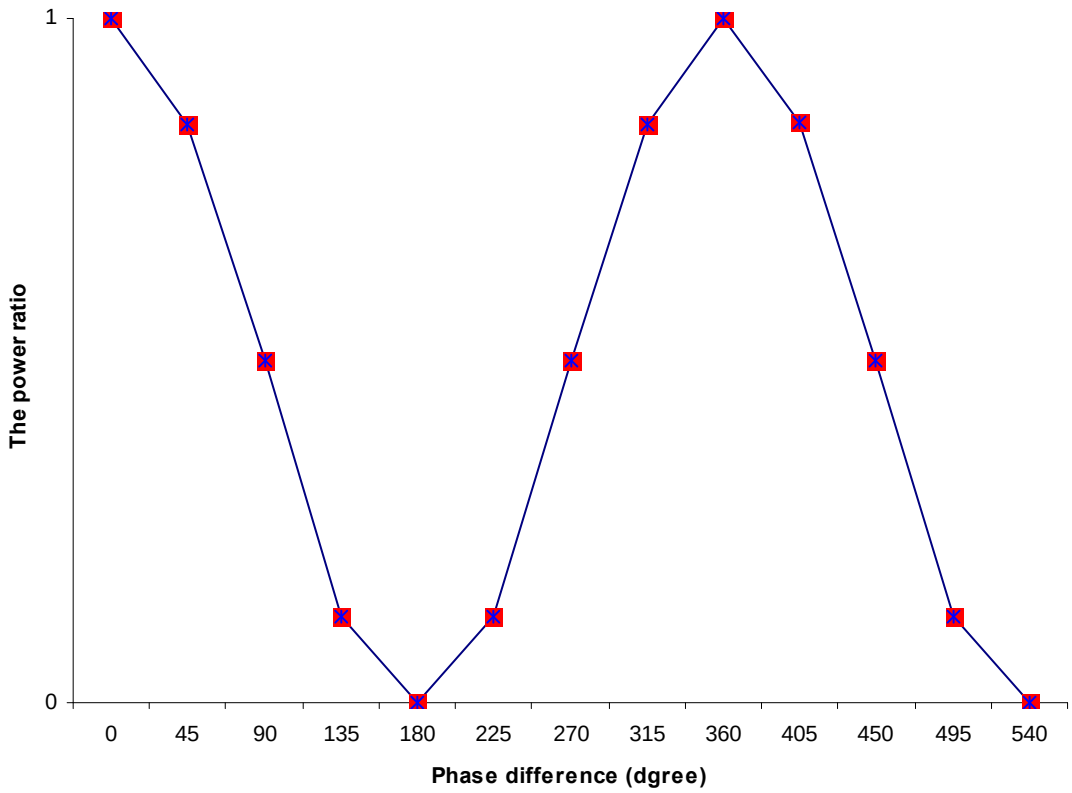

Figure (2-8): Plot of the transfer function of the MZI versus the phase difference Δφ

Such an MZI device can be applied for many purposes. By applying an electro-optical material and electrodes in one of the branches, the MZI can be used as an on/off modulator, while if it was provided with one or more additional input channels and if opto-optical materials were inserted it could also function as an optical transistor or a logic function. For sensing, however, one applies locally (within the so-called sensing window) on the top of one of the branches (the sensing branch) a chemo-optical layer. The MZI used as a sensor utilizes the transduction chain:

$$\Delta C \rightarrow \Delta n \rightarrow \Delta N_{eff} \rightarrow \Delta\varphi \rightarrow \Delta\,(P_{out} / P_{in}) \qquad (2\text{-}44)$$

where Δx denotes a change of the parameter x.

In all IO sensors a change of the value of the measurand (ΔC) affects the optical properties or position of one or more of the materials forming the waveguide. The extent of this change depends on the value of the measurand. The effects of these changes on modal parameters are in most cases not only nearly proportional to the change of optical properties but also to the fraction of the modal power which propagates through that material, and in fact it is this fraction which interrogates with the material. The most relevant optical properties which may be influenced are the refractive index, the absorption coefficient or the emission properties (e.g.

luminescence) of one of the materials. A change of the refractive index (Δn) expresses itself as a change of two parameters: the real part of N_{eff} and the field profile. A change of an absorption coefficient manifests itself in the imaginary part of N_{eff} and hence in the modal attenuation. Some of the absorbing material may show luminescent properties: part of the absorbed power is emitted as photons of another wavelength. In general the major part of the emitted power leaves the system as free space radiation, while a minor part is captured by the waveguide generating a new mode of another wavelength.

Changes of the (complex) refractive index distribution in a region which is relevant for the waveguide can be caused by physical (e.g. thermo-optical, electro-optical, mechano-optical) or chemo-optical cross effects and in addition by partial substitution of one material by another one [52]. For obtaining large sensitivities it is preferred that all waveguide materials show the relevant cross effect in order to utilize the modal power most effectively; in addition, it would be advantageous if all these materials possessed large cross coefficients.

The third step in the transduction chain can be quantified by the expression:

$$\Delta\varphi = \Delta N_{eff}\, L\, (2\pi/\lambda_0) \qquad (2\text{-}45)$$

where L is the interaction length (the length of the channel section provided with the interface or simply the sensor area) and λ_0 is the vacuum wavelength of the monochromatic light source.

Using the inverse transfer functions the concentration change can be derived from the change of the output power. This sounds simple, but in fact a too simple picture has been presented; reality is more unruly: many other physical phenomena appear to interfere in such a transduction chain: the perturbing factors. Maximizing resolution implies on the one hand maximizing all transfer functions and hence maximizing all partial sensitivities, such as $(\partial N_{eff} / \partial n)$, $[\partial (\Delta\varphi) / \partial N_{eff}]$ and $[\partial (P_{out} / P_{in}) / \partial (\Delta\varphi)]$ but on the other hand minimizing the effects of all perturbing factors.

Starting with maximizing the sensitivities, it can be immediately concluded that $[\partial (P_{out} / P_{in}) / \partial (\Delta\varphi)]$ is at maximum at the quadrature points: $\Delta\varphi = (2m + 1)\, \pi / 2$, and from (2-45) that $[\partial(\Delta\varphi) / \partial N_{eff}]$ will increase the longer the interaction length and the lower the wavelength. Both latter parameters are limited however: the first one mainly because the chip area is restricted, limiting L usually to about 1 cm; the second one as a consequence of material properties: the increase of absorption- and scatter-losses with decreasing wavelength. Hence generally a wavelength in the visible region is chosen while its precise value may depend on the requirements of the application aimed at. Also imperfectness of technology is a complicating factor. It hampers e.g. achieving perfect mirror symmetry of the Y-junctions, which had been implicitly assumed in deriving expression (2-43); also it hampers reaching the quadrature points at a preset

value (e.g. zero) of the concentration. Fortunately, these imperfections can be easily accounted for by inserting additional parameters (the visibility factor V and the phase offset $\Delta\varphi_0$ whose values have to be determined experimentally) into expression (2-43):

$$P_{out} = (P_{in} / 2) (1 + V \cos (\Delta\varphi + \Delta\varphi_0)) \qquad (2\text{-}46)$$

There are a number of perturbing factors, which will affect the $\Delta\varphi \rightarrow P_{out}$ transfer:

- Scatter light will be generated in the IO circuitry of which a part P_{scat} may be detected at the output port of the MZI
- Expressions (2-43) and (2-46) are correct if one mode of one given wavelength propagates through the system only. While launching the zeroth-order TE mode from a fiber generally also the zeroth-order TM mode is weakly excited and the power of this TM_{00}-mode has to be removed from the system
- A laser never shows a constant output: wavelength-, phase- and output power-fluctuations may occur, e.g., as a consequence of temperature fluctuations. Also mechanical instabilities can influence the P_{out} / P_{in} ratio
- Note also that if incidentally starting from $(\Delta\varphi + \Delta\varphi_0) = m\,\pi$ (m being an integer) it is unknown whether $\Delta\varphi$ is increasing or decreasing (directional ambiguity) while also near this state the partial sensitivity $[\partial P_{out} / \partial (\Delta\varphi)]$ is very low (sensitivity fading).

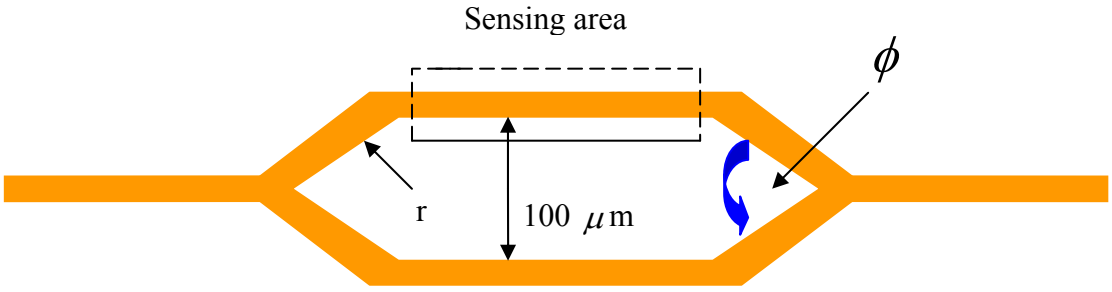

Figure (2-9): Top view of the basic configuration of an IO Mach-Zehnder Interferometer

In the integrated version of MZI, an input optical waveguide is split into two arms which, after a certain distance, recombine again in an output optical waveguide as shown in figure (2-9). Several MZI configurations were designed with varying parameters but there are some fixed principles which must be taken into consideration in each design in order to have small propagation losses. These principles are:

- The Y junction is formed with straight arms and small opening angles (i.e. 1°)
- The Y junction is shaped with circular bends with radii ranging between (200 μm to 5 mm)
- Separation between the sensor and the reference branches must exceed 50 μm to avoid coupling between modes traveling through both branches and the width of the branch is in the range of 3 μm to get monomode waveguide.
- In one arm, a (0.5, 1 or 2 mm) length and from 10 to 20 μm wide sensor area is created.
- The total length of the device is ranging between 7 to 9 mm to get a small chip area.
- The visibility signal (difference between the maximum and minimum intensity) depends on the coupling factor of the divisor and on the propagation losses of the guided mode in the interferometer arms. It must be at maximum and therefore it is important to design a divisor or Y junction with a coupling factor of 3 dB, that is, input light is equally divided in each branch of the interferometer. Moreover, propagation losses in the sensor and reference branch should be identical.

2.4 The heater design

In an optical waveguide, the optical path of the propagation light can be modified by thermal changes. A change in temperature of the waveguide by ΔT modifies the optical phase of the light traveling through it by Δφ. This is due to two effects: the variation in length of the waveguide due to a thermal expansion or contraction, and the temperature-induced change in the refractive index [54], [55].

These changes affect directly the optical phase of the light, given by:

$$\varphi = \frac{4\pi nL}{\lambda} \tag{2-47}$$

where n is the refractive index, λ is the wavelength of the light and L is the waveguide length.

The temperature effects on phase variations, $\frac{\Delta\varphi}{\Delta T}$, can be calculated by obtaining the derivative of φ with respect to temperature T, and is given by:

$$\frac{d\varphi}{dT} = \frac{4\pi}{\lambda} bL \tag{2-48}$$

where:

$$b = \left(\frac{dn}{dT} + \frac{n}{L}\frac{dL}{dT} \right) \tag{2-49}$$

The right hand terms of the last equation depend on the chemical composition of the waveguide.

As shown in figure (2-10), one design for a heater which is made from titanium and has two contacts from aluminum which will be used to inject electrical current to heat the reference arm of the MZI waveguide in order to create the required difference in refraction index that will control the propagation of light through the sensor and increase the sensitivity of the sensor.

The heater is 300 nm thick, 5 μm width, 35 μm height, 10 μm distance between vertical parts and 2 mm length. This heater will be placed at a distance equal to 3 μm away from the reference arm.

The thermal conductivity between the heater and the waveguide should be maximized, but this is normally limited by the need for sufficient optical insulation. In low-index contrast waveguides the distance between the core and the heater element must be several micrometers. Increasing the thermal conductivity around the heated waveguide makes the response faster, but it also increases the power consumption [55], [56]. This leads to a trade-off between the speed and the power consumption. In many waveguide structures the requirement for sufficient optical confinement also limits the possibility to increase the thermal conductivity between the waveguide core and the underlying substrate.

In order to calculate the total resistance of the heater to compare it with the measured value, the total length L and the cross sectional area of the heater must be calculated as shown in figure (2-11) and then the total resistance of the heater can be calculated from the next equation:

$$R = \rho \frac{L}{A} \tag{2-50}$$

where ρ, is the material resistivity of the heater. The total length of the heater is 11 mm, its cross sectional area is 1.5 pm^2, the resistivity of the titanium is $42 * 10^{-8} \Omega.m$ and hence the total resistance of the heater can be calculated as 3.08 KΩ.

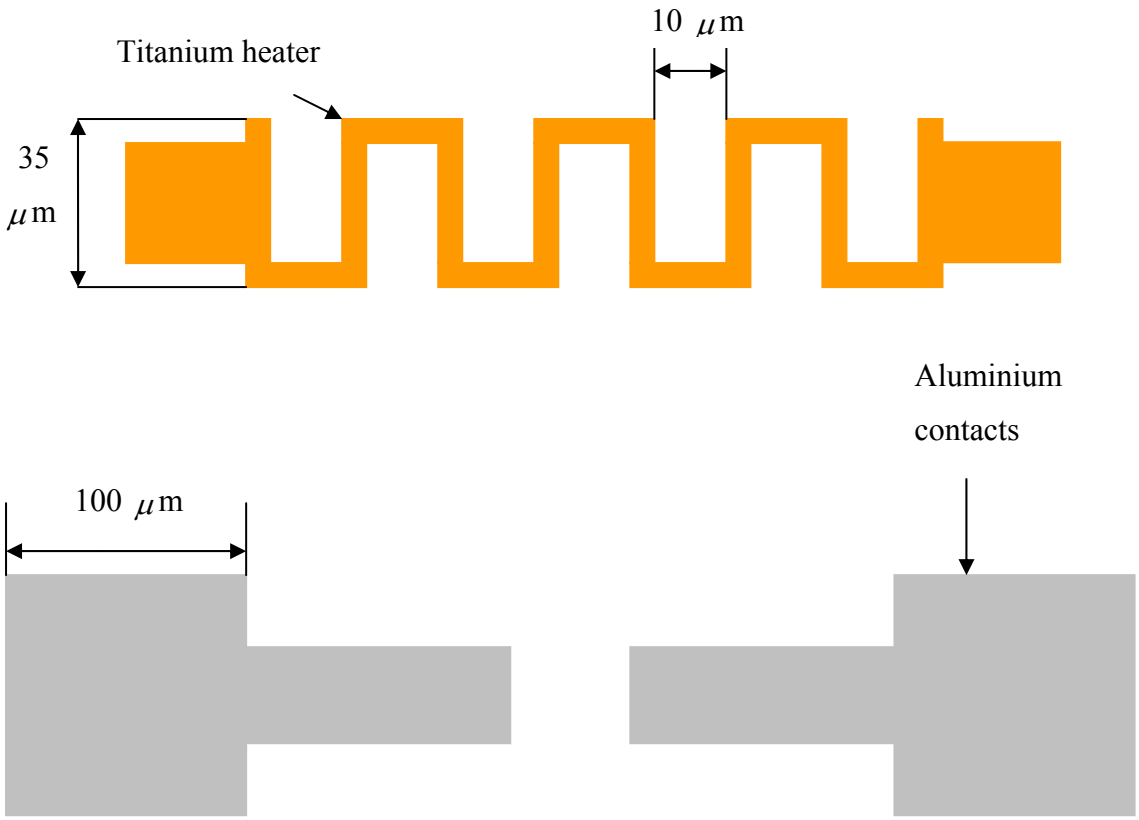

Figure (2-10): A top view of the titanium heater and the aluminium contacts

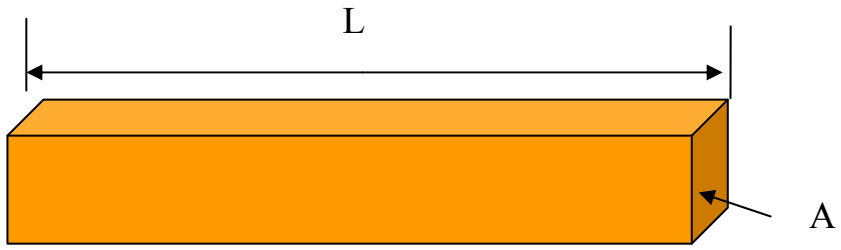

Figure (2-11). The heater as one part

With respect to the contacts, the resistivity of aluminium is $2.8*10^{-8}\Omega.m$ and the total resistance of the two contacts is 1.6 Ω and therefore the resistance of the two contacts is negligible with respect to the resistance of the heater.

Now the whole sensor is designed and is shown in figure (2-12). The next design task is transferring this sketch to the computer using Cadence program in order to fabricate the mask which will be used to fabricate the desired sensor.

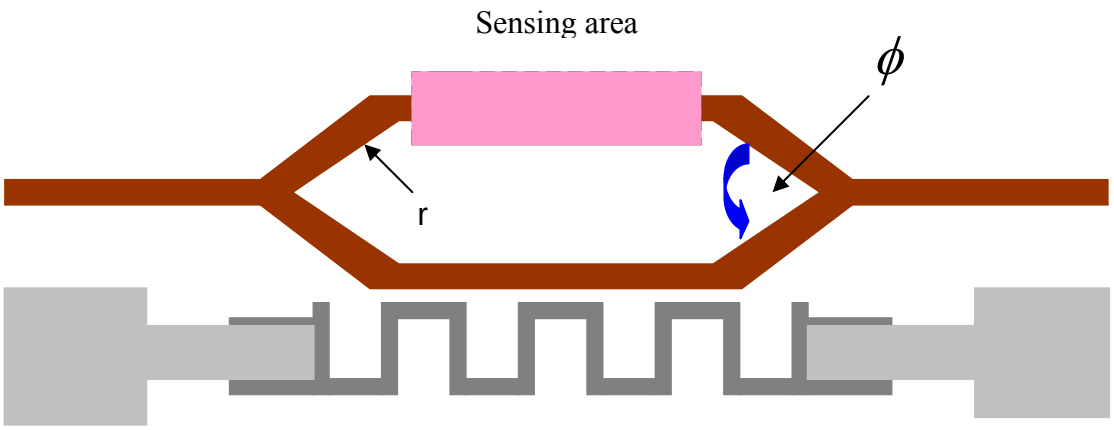

Figure (2-12): Optical waveguide based chemical sensor

3 Deposition of silicon nitride and silicon oxynitride by LPCVD

3.1 Introduction

In order to optimize the deposition processes by LPCVD to obtain high homogeneity layers of silicon nitride (Si_3N_4) and silicon oxynitride (SiON) to use them as guiding layers in optical waveguide chemical sensors the appropriate temperature and deposition rate had been chosen. Also the wafers must be distributed uniformly along the boat with leaving two free places between the wafers. These deposited layers must be suitable for both masking the local thermal oxidation and for coal etching. This process gives layers with high homogeneity and is better than the physical deposition processes.

The disadvantage of this process is that LPCVD is done at high temperatures (these high temperatures enhance deposition processes). To obtain Si_3N_4 and SiON the triethylsilane liquid ($C_6H_{16}Si$) was used instated of dichlorsilane gas because it is safe and harmless.

Three processes were done with a temperature of 740 °C, 760 °C and 780 °C. These different temperatures were chosen to help in optimizing the LPCVD process (to determine the temperature and deposition rate which give higher homogeneity layers).

3.2 Description of LPCVD process

The deposition of silicon nitride (Si_3N_4) and silicon oxynitride (SiON) was done in a three-zone oven for low pressure chemical vapor deposition shown in figure (3-1). The LPCVD is a vacuum deposition process and it is suitable for the production of thin layers. In the case of Si_3N_4, the ammonia (NH_3) and triethylsilane ($C_6 H_{16} Si$) were let to flow into the tube and reacted with each other to develop Si_3N_4 layer on the wafers as shown in the next equation:

$$4\ NH_3 + 3\ C_6 H_{16} Si \longrightarrow Si_3N_4 + \text{Secondary products}$$

In the case of SiON, additionally to NH_3 and $C_6 H_{16} Si$, oxygen O_2 also was let to flow into the tube as shown in the next equation:

$$NH_3 + C_6 H_{16} Si + O_2 \longrightarrow SiON + \text{Secondary products}$$

The quantity of gases can be adjusted by mass flow controllers. The deposition rate depends on the temperature and the pressure. At low temperatures the deposition rate is very low because more reactive gas molecules go away than deposit on the wafers. With increasing the temperature, the deposition rate increases on the surface of the wafers.

Figure (3-1): 3-zone-oven used to produce SiO_2 by thermal oxidation, TEOS decomposition, deposition of Si_3N_4 and SiON layers by LPCVD

The developed Si_3N_4 is stable mechanically and has a refractive index of (2.0 – 2.1). The developed SiON has a refractive index of (1.5 – 1.6). The boat and the carrier used to carry the wafers into the tube are shown in figure (3-2) without the wafers and in figure (3-3) with the wafers showing on it the wafers position, the direction of gas inlet (1) and the direction of gas outlet (2).

The boat is made from quartz and can carry maximum 9 wafers since there are two free places between wafers. This improves the homogeneity of the deposited layers.

Figure (3-2): The carrier (1) and the boat (2) used to carry the wafers into the tube

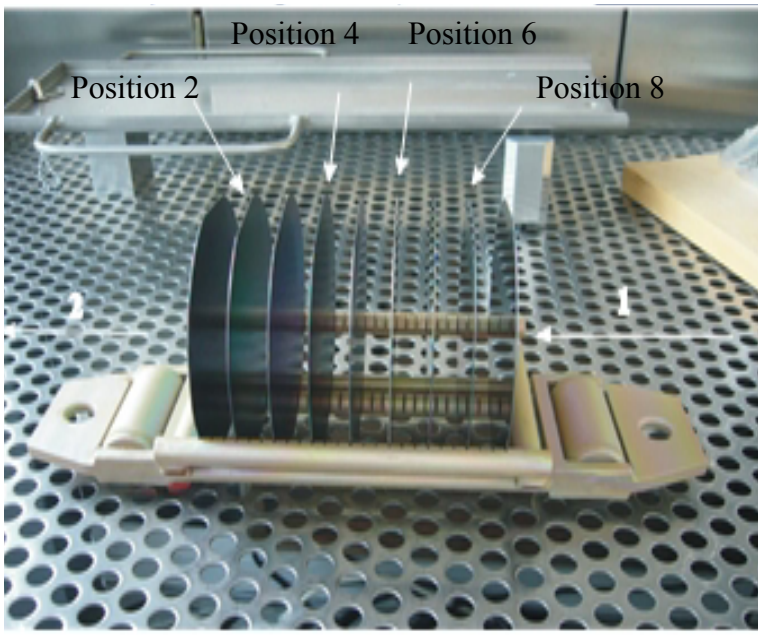

Figure (3-3): The carrier and the boat with the wafers showing the wafers position, the direction of gas inlet (1) and gas outlet (2)

The boat before going into the tube is shown in figure (3-4) where there is a second quartz carrier (1) placed above the wafers to improve the heat distribution and gas diffusion.

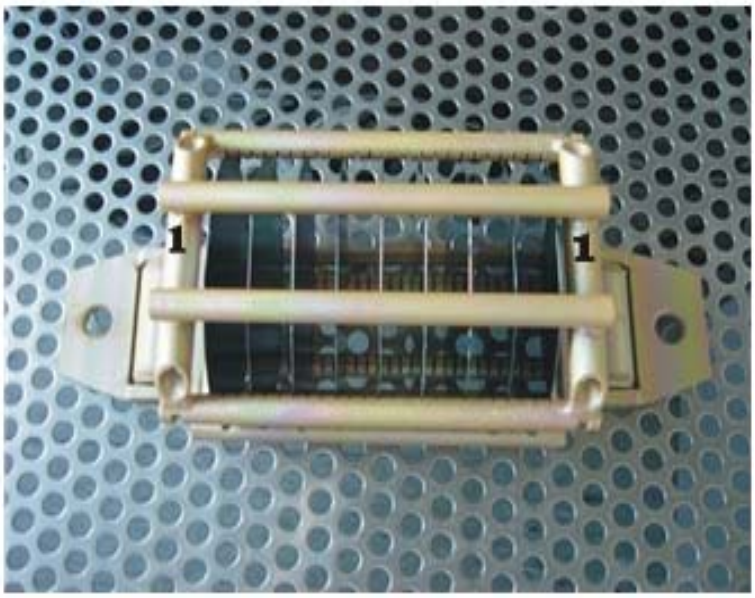

Figure (3-4): The boat with the wafers just before going into the tube

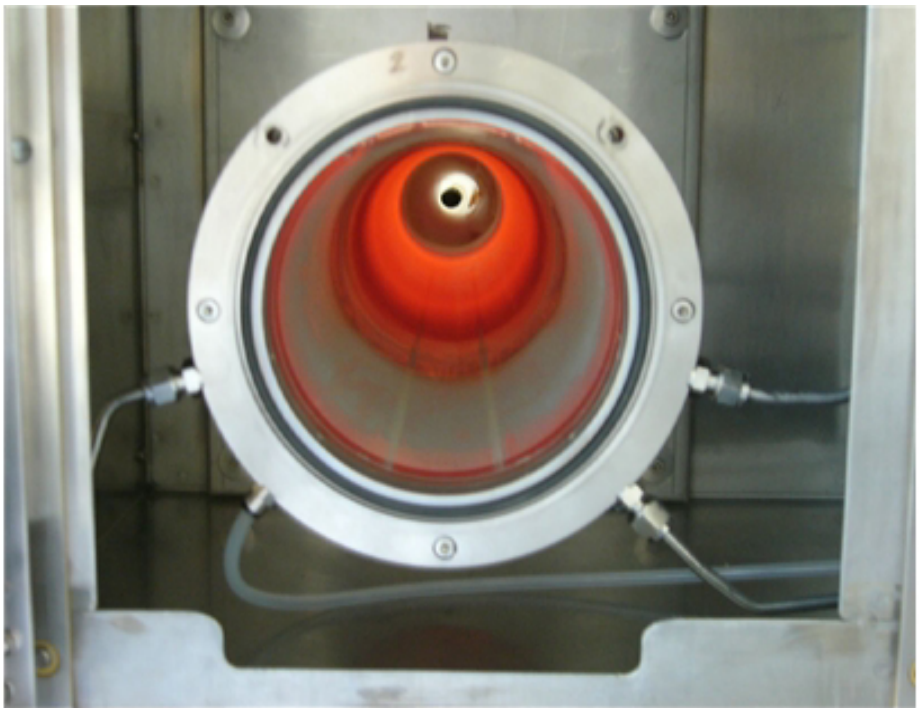

Figure (3-5): The quartz tube of LPCVD

The wafers are placed in the carrier such that their surface is toward the tube inlet hole (toward the direction of gases inlet). To improve the homogeneity of the deposited layers, the boat must be fully occupied with each deposition; therefore blind wafers are used to fill the places which have no wafers.

Then the boat is brought into the tube very slowly and very carefully since inside the tube is very hot as shown in figure (3-5) and with moving the boat quickly the wafers can be bended or broken due to the high temperature difference between inside and outside the tube. After that, the tube will be evacuated and then heated to the desired temperature and the deposition can be started.

3.3 Measuring of layer thickness and refractive index by ellipsometer

An ellipsometer which is shown in figure (3-6) enables to measure the refractive index and the thickness of semi-transparent thin films. The instrument relies on the fact that the reflection at a dielectric interface depends on the polarization of the light while the transmission of light through a transparent layer changes the phase of the incoming wave depending on the refractive index of the material. An ellipsometer can be used to measure layers as thin as 1 nm up to layers which are several microns thick. Applications include the accurate thickness measurement of thin films, the identification of materials and thin layers and the characterization of surfaces.

Figure (3-6): The ellipsometer

The principle of operation of an ellipsometer is illustrated by the schematic drawing of the ellipsometer shown in the figure (3-7) below:

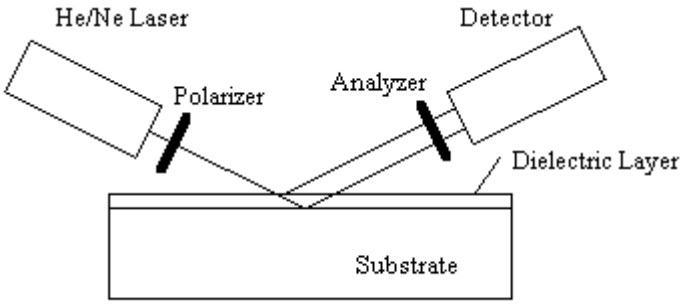

Figure (3-7): Schematic drawing of an ellipsometer

It consists of a laser (commonly a 632.8 nm helium/neon laser), a polarizer and a quarter wave plate which provide a state of polarization which can be varied from linearly polarized light to elliptically polarized light to circularly polarized light by varying the angle of the polarizer. The beam is reflected off the layer of interest and then analyzed with the analyzer. The operator changes the angle of the polarizer and analyzer until a minimal signal is detected. This minimum signal is detected if the light reflected by the sample is linearly polarized, while the analyzer is set so that only light with a polarization which is perpendicular to the incoming polarization is allowed to pass. The angle of the analyzer is therefore related to the direction of polarization of the reflected light if the null condition is satisfied. In order to obtain linearly polarized light after reflection, the polarizer must provide an optical retardation between the two incoming polarizations which exactly compensates for the optical retardation caused by the polarization dependent reflections at each dielectric interface. Since the amplitude of both polarizations was set to be equal, the ratio of the amplitudes after reflection equals the tangent of the angle of the analyzer with respect to the normal [57].

3.4 Preparation of the silicon wafers

For the deposition of Si_3N_4 and SiON 45 wafers were required (24 wafer for silicon nitride and 21 wafer for silicon oxynitride). The first step was marking the wafers on their back surfaces. This was done by a special cutter with diamond edge. After that, a cleaning process was done which remove any organic materials from the surface of the wafers. Cleaning process steps are shown in table (3-1).

3.5 Deposition process

3.5.1 Silicon nitride (Si_3N_4) deposition

The deposition was done at temperatures of 740 °C, 760 °C and 780 °C and the deposition time was 20 min. The wafer was placed at the center of the boat (position 4) during deposition.

1	Blow off with N_2	To remove small particles from the wafers
2	Ultrasonic bath	It consists of water and a wetting agent and it separates the particles which are strongly bonded with the wafers
3	Washing in DI water	To remove the wetting agent of the previous cleaning step from the surface of the wafers
4	Piranhia-acid	The acid consists of a $H_2 SO_4$ / $H_2 O_2$ solution and it solves any organic residues from the surface of the wafers
5	Washing in DI water	To remove the acid residues from the surface of the wafers
6	Drying process	At the end, the wafers are washed in DI water and they dried using N_2 in drying machine

Table (3-1): Cleaning procedures

3.5.1.1 Deposition of Si_3N_4 at 740 °C

The process parameters of this deposition are shown in table (3-2) and the results of thicknesses and refractive indices are distributed on the wafer shown in figure (3-8).

Ammonia (NH_3) flow rate	21 %
Triethylsilane ($C_6 H_{16} Si$) flow rate	97 %
Process temperature	740 °C
Process pressure	0.6 mbar
Process time	20 min

Table (3-2): Process parameters for silicon nitride deposition at 740 °C

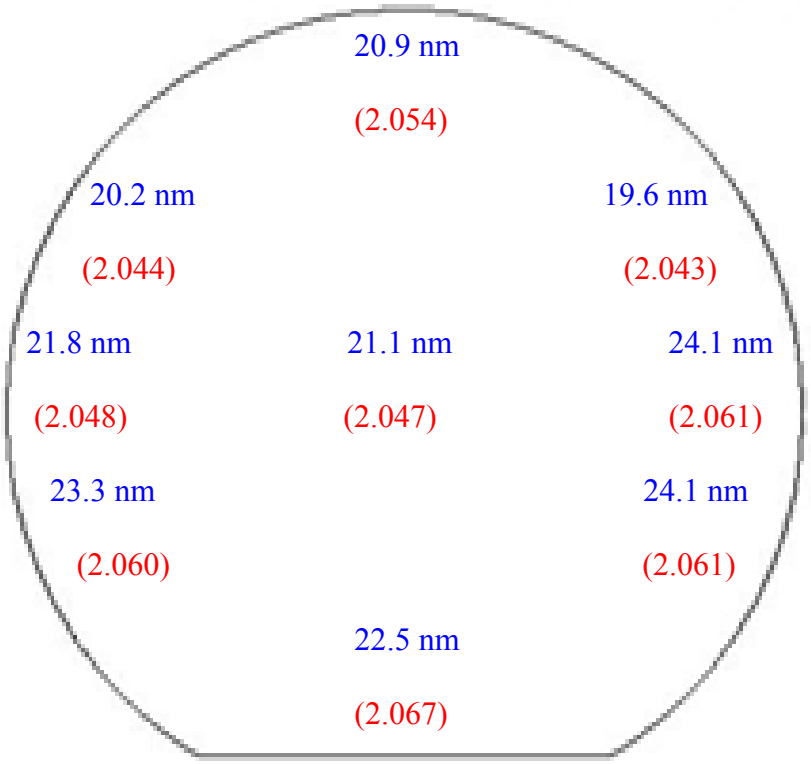

Figure (3-8): Thicknesses and refractive indices distribution at 740 °C (wafer 1)

The deposition layer has a thickness ranging between 20 nm and 24 nm. The homogeneity of the layer is not uniform since there is a thickness variation along the wafer equal to 4.5 nm (18.7 %). The layer thickness increases at the parts which the gases are moving and reacting faster. The average value for the thickness is 21.9 nm and for the refractive index is 2.054. The deposition rate was approximately 0.9 nm/min (low rate and the desired layers can not be deposited in an acceptable time).

3.5.1.2 Deposition of Si_3N_4 at 760 °C

The process parameters of this deposition are shown in table (3-3) and the results of thicknesses and refractive indices are distributed on the wafer shown in figure (3-9).

Ammonia (NH_3) flow rate	21 %
Triethylsilane ($C_6H_{16}Si$) flow rate	97 %
Process temperature	760 °C
Process pressure	0.6 mbar
Process time	20 min

Table (3-3): Process parameters for silicon nitride deposition at 760 °C

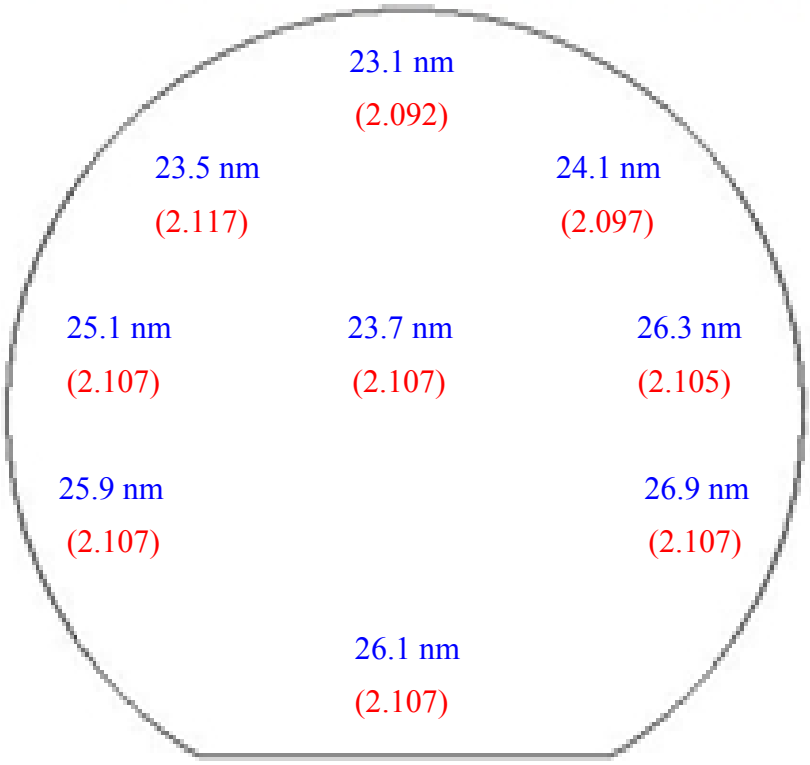

Figure (3-9): Thicknesses and refractive indices distribution at 760 °C (wafer 2)

At a temperature of 760 °C, the deposition rate increased to 1.2 nm/min. The homogeneity also improved because the thickness variation along the wafer decreased to 3.8 nm (14.1 %). The gas deposition at the edge is more than at the center of the wafer (the thickness is smaller at the center). The average value for the thickness is 24.7 nm and for the refractive index is 2.105.

3.5.1.3 Deposition of Si_3N_4 at 780 °C

The process parameters of this deposition are shown in table (3-4) and the results of thicknesses and refractive indices are distributed on the wafer shown in figure (3-10).

Ammonia (NH_3) flow rate	21 %
Triethylsilane ($C_6H_{16}Si$) flow rate	97 %
Process temperature	780 °C
Process pressure	0.6 mbar
Process time	20 min

Table (3-4): Process parameters for silicon nitride deposition at 780 °C

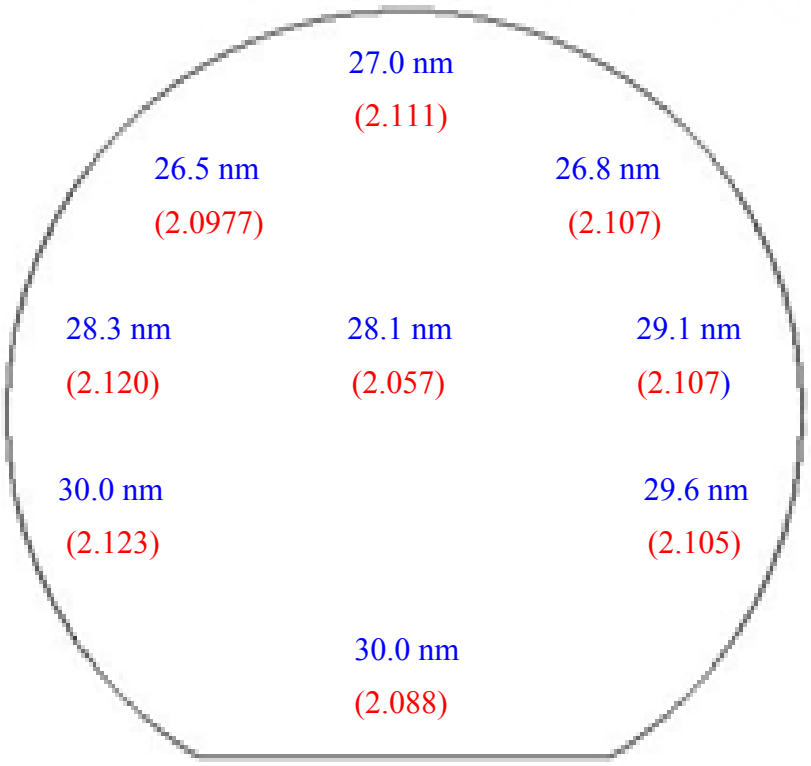

Figure (3-10): Thicknesses and refractive indices distribution at 780 °C (wafer 3)

The deposition shows the same result as the deposition at 760 °C. The thickness variation is 3.5 nm (11.7 %). The deposition rate increased to 1.5 nm/min. The average value for the thickness is 28.3 nm and for the refractive index is 2.102.

3.5.1.4 Temperature optimization

From the results of the three deposition processes, it is clear that, deposition at 740 °C is the worst one because the deposition rate is small and the thickness variation along the wafer is large (18.7 %). This deposition can not deposited thick layers at short time since the deposition rate is only 0.9 nm/min. The depositions at 760 °C and 780 °C show better results with respect to the deposition rate and the homogeneity. Therefore, the next deposition processes will be done at only 760 °C and 780 °C using three wafers in each deposition to optimize the homogeneity along the boat. The wafers will be placed at positions 2, 4 and 8 in the boat.

The results for depositions of wafers (4, 5 and 6) in the same boat at temperature of 780 °C are shown in table (3-5) and of wafers (7, 8 and 9) in the same boat at temperature of 760 °C are shown in table (3-6). It is found that the deposition rate increased at the front place of the boat (position 2). The thickness variation along the boat of wafers (4, 5 and 6) was 23.8 nm (52.3 %).

The thickness variation along the boat of wafers (7, 8 and 9) was 15.7 nm (47.43 %). The thickness variation along this boat is smaller than that of the first boat. This means that the homogeneity was improved. Hence, the deposition at 760 °C had better results and it is also preferred because the temperature is lower. Therefore, the next

depositions will be done only at 760 °C and to decrease the thickness variation along the boat at temperature of 760 °C, the temperatures of the heating zones along the tube must be optimized.

Temperature 780 °C	Wafer 4 Position 2		Wafer 5 Position 4		Wafer 6 Position 8	
Measurement No.	Thickness (nm)	Refractive index	Thickness (nm)	Refractive index	Thickness (nm)	Refractive index
1	38.4	2.066	29.2	2.115	23.0	2.098
2	42.4	2.022	31.2	2.125	25.0	2.115
3	45.5	2.076	32.0	2.016	25.0	2.107
4	41.5	2.076	30.1	1.980	23.3	2.075
5	36.0	2.044	27.9	1.966	21.2	2.057
6	35.9	2.066	28.2	1.967	21.8	2.068
7	37.8	2.057	28.5	1.967	21.5	2.063
8	39.8	2.076	29.9	1.986	23.1	2.070
9	42.7	2.081	31.1	2.006	24.5	1.966
The average	39.9	2.063	29.7	2.000	23.1	2.069
Deposition rate	1.995 nm/min		1.485 nm/min		1.155 nm/min	
Thickness vari.	7 nm (16.7 %)		4.1 nm (12.8 %)		4 nm (16 %)	

Table (3-5): The results for depositions of wafers (4, 5 and 6) in the same boat at temperature of 780 °C

The next deposition was done on wafers (10, 11 and 12) in the same boat with changing the temperatures of the heating zones along the tube. The temperature at the front zone was 720 °C, at the middle zone was 753 °C and at the back zone was 759 °C. The results of this deposition are shown in table (3-7).

By changing the temperature of the heating zones along the boat, it is found that the gas deposition decreased at front of the boat since the front temperature is low. So the temperature in the front side of the boat must be increased. The thickness variation along the boat decreased to 9.6 nm (28.6 %). The homogeneity of the individual wafers had been improved.

Temperature 760 °C	Wafer 7 Position 2		Wafer 8 Position 4		Wafer 9 Position 8	
Measurement No.	Thickness (nm)	Refractive index	Thickness (nm)	Refractive index	Thickness (nm)	Refractive index
1	29.6	2.001	22.9	2.099	18.1	2.067
2	33.1	2.046	24.3	2.078	19.3	2.068
3	32.8	2.039	24.3	2.126	19.3	2.084
4	30.4	2.026	23.4	2.104	18.7	2.017
5	27.9	1.972	21.4	2.090	17.7	2.007
6	28.2	1.976	21.9	2.092	17.4	2.047
7	28.9	1.990	22.0	2.077	17.5	1.997
8	31.4	2.019	23.5	2.100	18.8	2.047
9	33.2	2.046	24.9	2.126	19.7	2.077
The average	30.6	2.013	23.5	2.099	18.4	2.046
Deposition rate	1.530 nm/min		1.175 nm/min		0.920 nm/min	
Thickness vari.	5 nm (15.1 %)		3.5 nm (14 %)		2 nm (10.5 %)	

Table (3-6): The results for depositions of wafers (7, 8 and 9) in the same boat at temperature of 760 °C

The next deposition was done on wafers (13, 14 and 15) in the same boat with changing the temperature of the heating zones along the tube. The temperature at the front zone was 732 °C, at the middle zone was 754 °C and at the back zone was 759 °C. The results of this deposition are shown in table (3-8).

By increasing the temperature of the front heating zone, the deposition rate increased at the front of the boat. The thickness variation along the boat decreased to 5.6 nm (16.62 %). The wafers 14 and 15 have nearly the same layer thicknesses. The temperature of the front heating zone must be increased in order to improve the homogeneity of the layers.

Front: 720 °C Middle: 753 °C Back: 759 °C						
	Wafer 10 Position 2		Wafer 11 Position 4		Wafer 12 Position 8	
Measurement No.	Thickness (nm)	Refractive index	Thickness (nm)	Refractive index	Thickness (nm)	Refractive index
1	24.7	2.093	30.6	2.097	31.3	2.109
2	27.1	2.083	31.7	2.105	32.8	2.113
3	26.6	2.103	31.7	2.109	33.6	2.121
4	25.9	2.067	31.6	2.103	33.1	2.113
5	25.1	2.087	30.1	2.097	31.5	2.097
6	24.0	2.086	30.1	2.102	30.3	2.116
7	25.1	2.087	30.1	2.109	29.8	2.097
8	26.1	2.085	31.2	2.106	31.7	2.107
9	26.1	2.088	31.5	2.097	33.5	2.112
The average	25.6	2.087	30.9	2.103	31.8	2.109
Deposition rate	1.280 nm/min		1.545 nm/min		1.590 nm/min	
Thickness vari.	3 nm (11.1 %)		1.6 nm (5.05 %)		3 nm (9.0 %)	

Table (3-7): Deposition of wafers (10, 11 and 12) in the same boat with changing the temperatures of the tube to [Front zone: 720 °C, Middle zone: 753 °C and Back zone: 759 °C]

The next deposition was done on wafers (16, 17 and 18) in the same boat with changing the temperatures of the heating zones along the tube. The temperature at the front zone was 750 °C, at the middle zone was 756 °C and at the back zone was 760 °C. The results of this deposition are shown in table (3-9).

The results in this deposition had been improved. The homogeneity of wafer 16 is not optimized yet but it is increased along the boat. The thickness variation along the boat decreased to 4.8 nm (15.1 %) and this was the best result could be obtained. The homogeneity was optimized in this deposition and to test the ability of reproduction, this deposition will be repeated.

Front: 732 °C Middle: 754 °C Back: 759 °C						
	Wafer 13 Position 2		Wafer 14 Position 4		Wafer 15 Position 8	
Measurement No.	Thickness (nm)	Refractive index	Thickness (nm)	Refractive index	Thickness (nm)	Refractive index
1	28.1	2.093	32.2	2.087	32.2	2.121
2	30.3	2.101	33.3	2.117	33.4	2.146
3	31.3	2.110	33.1	2.112	33.3	2.127
4	29.0	2.087	32.6	2.116	33.7	2.117
5	29.6	2.080	31.3	2.101	30.4	2.114
6	27.5	2.090	31.0	2.103	30.9	2.116
7	28.1	2.097	30.9	2.097	30.9	2.114
8	30.2	2.107	32.7	2.114	33.1	2.118
9	30.9	2.077	33.2	2.112	33.6	2.117
The average	29.4	2.094	33.2	2.107	32.2	2.121
Deposition rate	1.470 nm/min		1.660 nm/min		1.610 nm/min	
Thickness vari.	3.2 nm (10.22 %)		2.4 nm (7.21 %)		3.3 nm (9.79 %)	

Table (3-8): Deposition of wafers (13, 14 and 15) in the same boat with changing the temperatures of the heating zones along the tube to [Front zone: 732 °C, Middle zone: 754 °C and Back zone: 759 °C]

The last deposition was repeated but with 4 wafers instead of three and the fourth wafer was placed at position 6 in the boat. The results of this deposition are shown in table (3-10).

This deposition shows the reproducibility of the process since the thickness variation along the boat is 4.7 nm (15.1 %) which is almost the same as before. The homogeneity in this deposition is sufficient for the intended purposes.

Front: 750 °C Middle: 756 °C Back: 760 °C						
	Wafer 16 Position 2		Wafer 17 Position 4		Wafer 18 Position 8	
Measurement No.	Thickness (nm)	Refractive index	Thickness (nm)	Refractive index	Thickness (nm)	Refractive index
1	27.6	2.087	29.6	1.977	30.3	2.097
2	30.2	2.095	30.6	2.023	31.6	2.104
3	30.2	2.097	31.6	2.017	31.4	2.116
4	29.3	2.077	30.3	2.017	30.3	2.106
5	27.2	2.079	28.7	2.006	29.1	2.097
6	27.0	2.083	28.4	2.006	29.0	2.087
7	27.2	2.086	30.1	2.019	28.7	2.089
8	28.9	2.084	29.0	2.096	30.8	2.099
9	30.2	2.077	30.5	2.036	31.8	2.101
The average	28.6	2.085	29.8	2.022	30.3	2.100
Deposition rate	1.430 nm/min		1.490 nm/min		1.515 nm/min	
Thickness vari.	3.2 nm (10.60 %)		3.2 nm (10.13 %)		3.1 nm (9.75 %)	

Table (3-9): Deposition of wafers (16, 17 and 18) in the same boat with changing the temperatures of the tube to [Front zone: 750 °C, Middle zone: 756 °C and Back zone: 760 °C]

3.5.1.5 Ammonia flow optimization

In the next depositions the amount of ammonia will be changed to see its effect on homogeneity and refractive index. The first deposition (wafer 23) was done with flow rate equal to 30 % (63.18 SCCM) of ammonia. The parameters of this process are shown in table (3-11) and the results are shown in figure (3-11).

It is found that the deposition rate is 1.385 nm/min, the thickness variation along the wafer is 4.6 nm (14.84 %), the average thickness is 27.7 nm and the average refractive index is 2.085.

Front: 750 °C Middle: 756 °C Back: 760 °C								
	Wafer 19 Position 2		Wafer 20 Position 4		Wafer 21 Position 6		Wafer 22 Position 8	
Meas. No.	Thick. (nm)	Refr. index	Thick. (nm)	Refr. index	Thick. (nm)	Refr. index	Thick. (nm)	Refr. index
1	27.4	2.097	28.7	1.097	29.1	2.097	28.5	2.057
2	29.0	2.112	29.9	2.083	30.1	2.119	29.8	2.069
3	29.3	2.087	29.6	2.107	30.7	2.107	30.6	2.107
4	29.0	2.100	29.3	2.100	29.7	2.107	30.3	2.060
5	26.3	2.105	27.6	2.103	27.9	2.101	27.6	2.041
6	26.3	2.087	27.4	2.100	27.9	2.088	27.4	2.048
7	26.4	2.087	27.2	2.097	28.3	2.098	26.5	2.058
8	29.0	2.087	29.2	2.104	29.6	2.090	29.5	2.060
9	29.6	2.110	29.7	2.109	30.0	2.098	31.0	2.077
AV	28.0	2.097	28.7	2.100	29.6	2.101	29.0	2.064
DR	1.400 nm/min		1.435 nm/min		1.480 nm/min		1.45 nm/min	
TV	3.3 nm (11.15 %)		2.7 nm (9.03 %)		2.8 nm (9.12 %)		4.5 nm (14.5 %)	

Table (3-10): Deposition on wafers (19, 20, 21 and 22) in the same boat with changing the temperature of the tube to [Front zone: 750 °C, Middle zone: 756 °C and Back zone: 760 °C] where AV is the average value, DR is the deposition rate and TV is the thickness variation

Ammonia (NH_3) flow rate	30 %
Triethylsilane ($C_6H_{16}Si$) flow rate	97 %
Process temperature	760 °C
Process pressure	0.6 mbar
Process time	20 min

Table (3-11): Process parameters for Si_3N_4 deposition with ammonia flow rate of 30 %

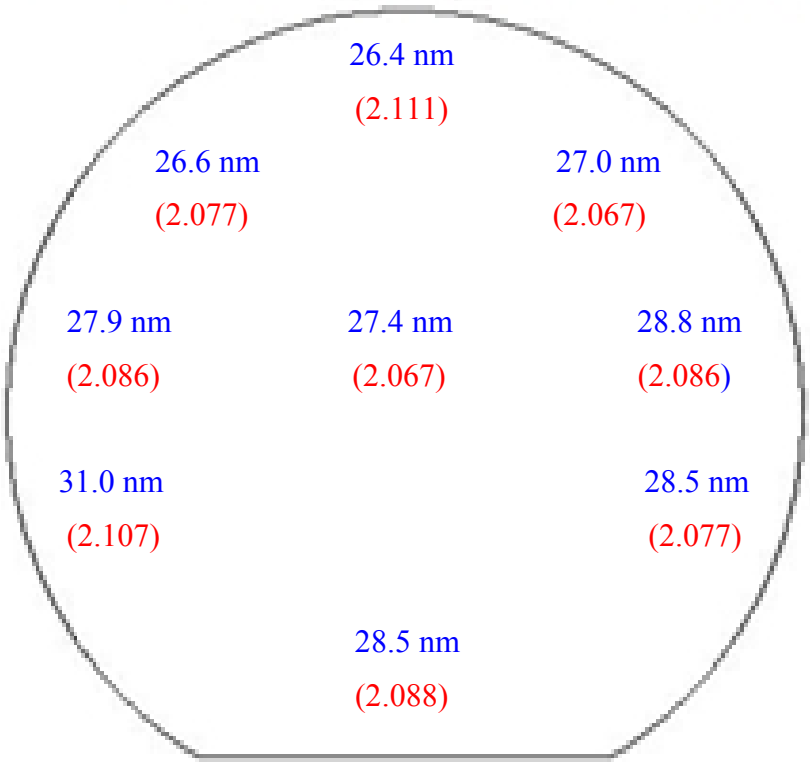

Figure (3-11): Thicknesses and refractive indices distribution of Si_3N_4 deposition with flow rate of 30 % ammonia (wafer 23)

The next deposition (wafer 24) was done with ammonia flow rate 15 % (31.59 SCCM). The parameters of this process are shown in table (3-12) and the results are shown in figure (3-12).

Ammonia (NH_3) flow rate	15 %
Triethylsilane ($C_6H_{16}Si$) flow rate	97 %
Process temperature	760 °C
Process pressure	0.6 mbar
Process time	20 min

Table (3-12): Process parameters for Si_3N_4 deposition with ammonia flow rate of 15 %

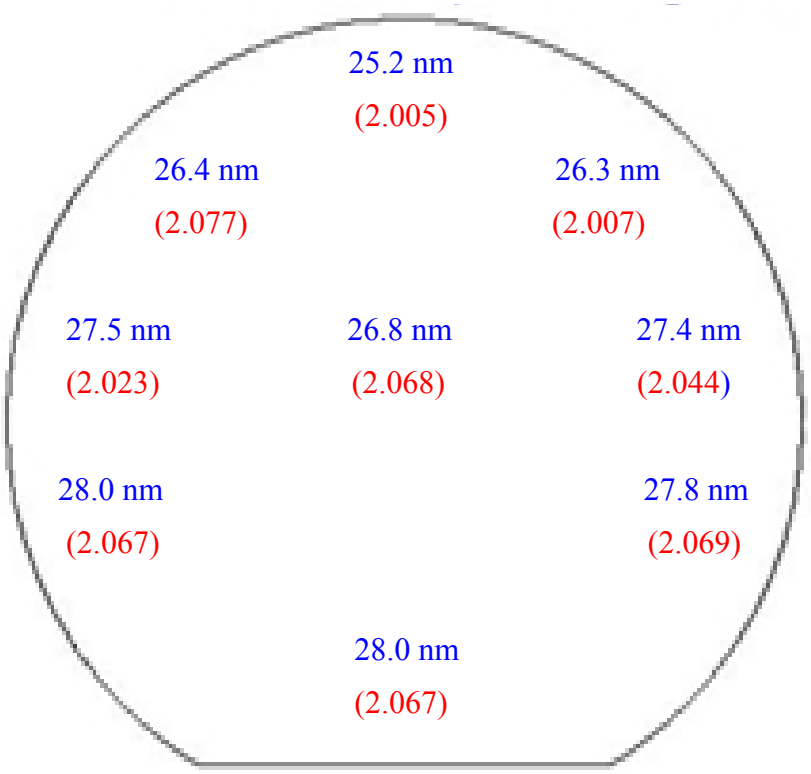

Figure (3-12): Thicknesses and refractive indices distribution of Si_3N_4 deposition with flow rate of 15 % ammonia (wafer 24)

It is found that the deposition rate is 1.35 nm/min, the thickness variation along the wafer is 2.8 nm (10 %), the average thickness is 27.0 nm and the average refractive index is 2.047.

From these results there is no much difference in the refractive index in both cases but the homogeneity is better with ammonia flow rate 15 %.

3.5.2 Silicon oxynitride (SiON) deposition

The optimized parameters which were obtained from the deposition of silicon nitride were used here to deposit silicon oxynitride in order to obtain a homogenous layer to use it as a guiding layer in the waveguide which will be used as a transducer for the desired chemical sensor. Every deposition was done with front zone temperature 750 °C, middle zone temperature 756 °C, back zone temperature 760 °C and pressure 0.6 mbar using one wafer and this wafer was placed at position 4 (the best position) in the boat.

The process parameters used in the first deposition on wafer 1 are shown in table (3-13) and the results of this deposition are shown in table (3-14).

Ammonia (NH_3) flow rate	34.66 %
Triethylsilane ($C_6H_{16}Si$) flow rate	85 %
Oxygen (O_2) flow rate	0.178 %
Process temperature	(750-756-760) °C
Process pressure	0.6 mbar
Process time	50 min

Table (3-13): Process parameters used in SiON deposition (O_2 flow rate is 0.178 %)

0.178 % of O_2	M_1	M_2	M_3	M_4	M_5	Average
Thickness (nm)	598.330	598.910	597.003	602.001	599.423	599.133
Refractive index	1.504	1.501	1.499	1.510	1.511	1.504
(Wafer 1) Deposition rate is 11.982 nm/min						

Table (3-14): The results of SiON deposition with O_2 flow rate of 0.178 %

From the results of this deposition it is found that the average refractive index (1.504). The results show that the layer is homogenous since the thickness variation along the wafer is approximately 5 nm (0.83 %) and the homogeneity is better than with silicon nitride. In the next depositions the oxygen flow rate was decreased to increase the refractive index of the silicon oxynitride with fixing the other parameters. The results of the depositions on wafers (2 – 6) are shown in table (3-15) and on wafers (7 – 11) in table (3-16).

The results show that the layers of SiON are more homogenous than the layers of Si_3N_4 since the thickness variation along the wafer in SiON is very small. From the results shown in both tables, it is clear that, the lower the oxygen flow rate the lower the deposition rate and the higher the refractive index of the silicon oxynitride. The relationship between the oxygen flow rate and the refractive index of the silicon oxynitride is shown in figure (3-13).

0.174 % of O_2	M_1	M_2	M_3	M_4	M_5	Average
Thickness (nm)	583.111	582.963	584.073	585.601	586.496	584.449
Refractive index	1.501	1.533	1.540	1.499	1.491	1.513
(Wafer 2) Deposition rate is 11.689 nm/min						
0.170 % of O_2	M_1	M_2	M_3	M_4	M_5	Average
Thickness (nm)	569.039	569.998	571.438	573.111	572.867	571.291
Refractive index	1.511	1.517	1.524	1.531	1.534	1.523
(Wafer 3) Deposition rate is 11.426 nm/min						
0.166 % of O_2	M_1	M_2	M_3	M_4	M_5	Average
Thickness (nm)	551.312	553.479	554.019	558.989	557.676	555.095
Refractive index	1.533	1.539	1.533	1.524	1.537	1.531
(Wafer 4) Deposition rate is 11.102 nm/min						
0.162 % of O_2	M_1	M_2	M_3	M_4	M_5	Average
Thickness (nm)	540.991	542.432	539.987	538.762	542.319	540.898
Refractive index	1.549	1.547	1.541	1.539	1.532	1.542
(Wafer 5) Deposition rate is 10.818 nm/min						
0.158 % of O_2	M_1	M_2	M_3	M_4	M_5	Average
Thickness (nm)	525.374	525.989	527.231	526.317	526.412	526.265
Refractive index	1.551	1.553	1.556	1.548	1.549	1.551
(Wafer 6) Deposition rate is 10.525 nm/min						

Table (3-15): The results of deposition processes of SiON on wafers (2 – 6) with decreasing the oxygen flow rate with each wafer

From figure (3-13), it can be seen that the higher the oxygen flow rate the lower the refractive index. From this figure also the required oxygen flow which gives the desired refractive index can be obtained.

0.154 % of O_2	M_1	M_2	M_3	M_4	M_5	Average
Thickness (nm)	511.931	513.702	514.678	519.317	516.321	515.190
Refractive index	1.561	1.559	1.554	1.562	1.558	1.559
(Wafer 7) Deposition rate is 10.304 nm/min						
0.150 % of O_2	M_1	M_2	M_3	M_4	M_5	Average
Thickness (nm)	501.999	503.246	504.491	504.663	506.081	504.096
Refractive index	1.561	1.564	1.572	1.577	1.570	1.569
(Wafer 8) Deposition rate is 10.082 nm/min						
0.146 % of O_2	M_1	M_2	M_3	M_4	M_5	Average
Thickness (nm)	490.081	492.783	495.141	494.938	494.777	493.544
Refractive index	1.571	1.573	1.573	1.582	1.579	1.576
(Wafer 9) Deposition rate is 9.871 nm/min						
0.142 % of O_2	M_1	M_2	M_3	M_4	M_5	Average
Thickness (nm)	482.631	480.374	484.990	485.371	481.012	482.876
Refractive index	1.574	1.591	1.592	1.599	1.582	1.587
(Wafer 10) Deposition rate is 9.658 nm/min						
0.138 % of O_2	M_1	M_2	M_3	M_4	M_5	Average
Thickness (nm)	474.321	468.031	469.781	473.073	473.146	471.67
Refractive index	1.622	1.599	1.581	1.607	1.571	1.596
(Wafer 11) Deposition rate is 9.433 nm/min						

Table (3-16): The results of deposition processes of SiON on wafers (7 – 11) with decreasing the oxygen flow rate with each wafer

Deposition of wafers (12 – 21) were done with 0.158 % oxygen flow rate at different times and the results were given graphically as shown in figure (3-14). The figure (3-14) shows the relationship between the thicknesses of the deposited layers and

the deposition times. From this figure the required time which gives the desired thickness can be obtained.

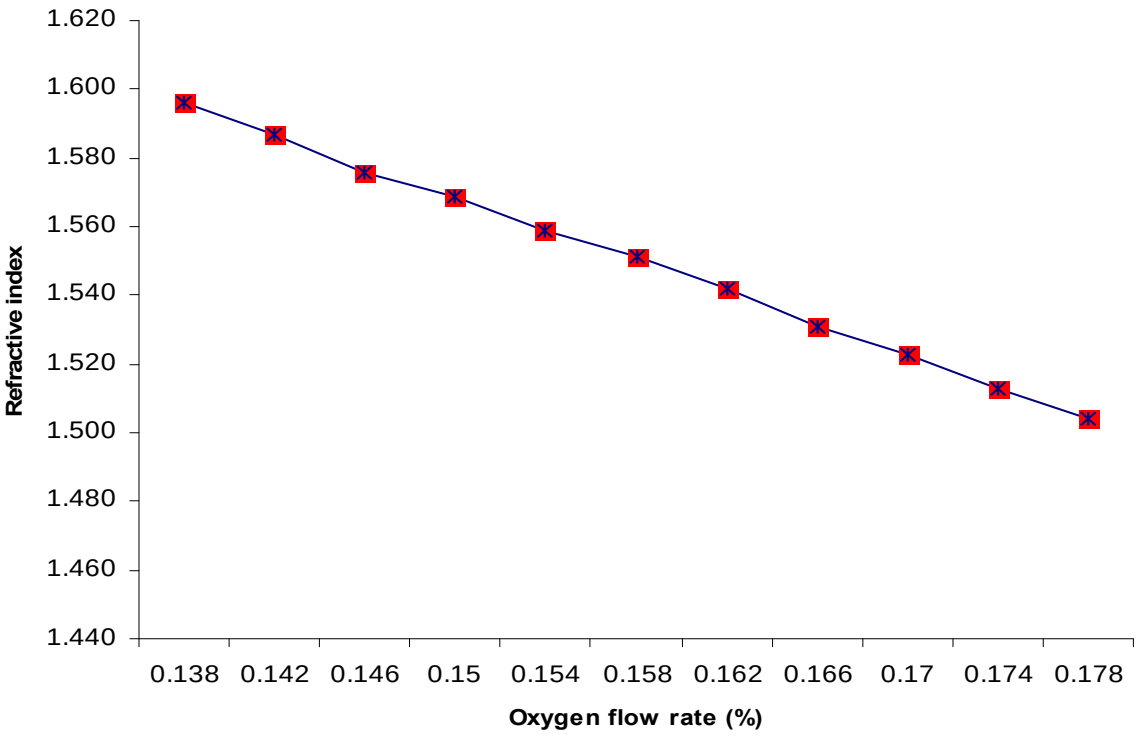

Figure (3-13): The relationship between the oxygen flow rate and the refractive index of the deposited layers

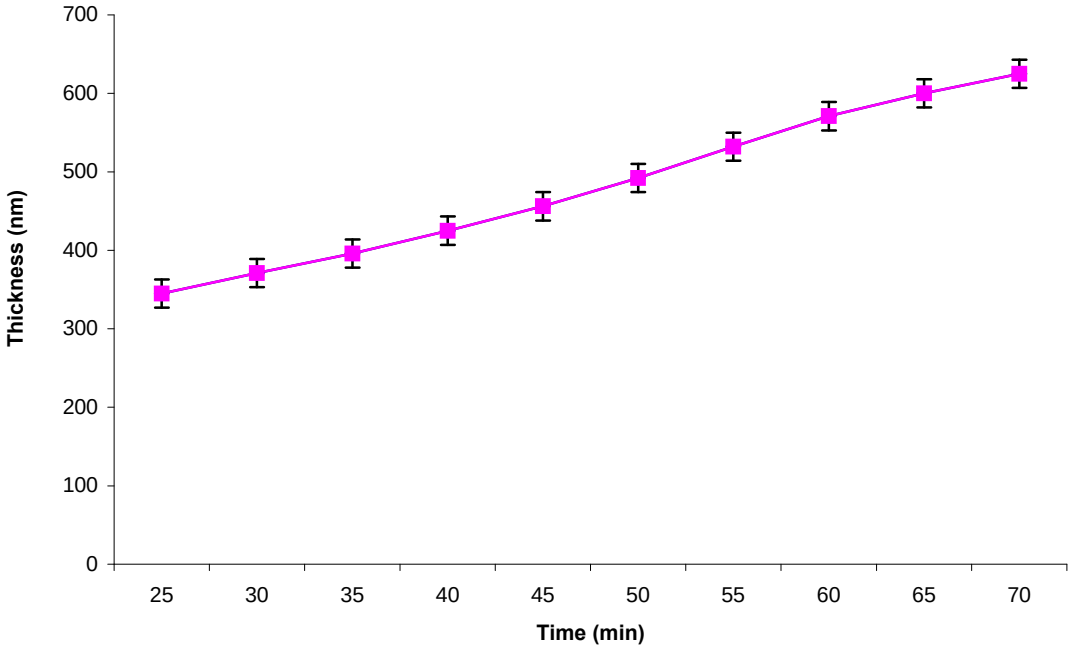

Figure (3-14): The relationship between the thicknesses of the deposited layers and the deposition times for SiON layers with flow rate of oxygen equal to 0.158 %.

4 Silicon oxynitride waveguide based ammonia sensor

4.1 Introduction

As an application of low pressure chemical vapor deposition of silicon oxynitride, the deposited silicon oxynitride layer will be used in this part as a guiding layer in the designed Mach-Zehnder interferometer waveguide which will be used as a transducer in an optical waveguide based ammonia sensor.

This sensor consists of an integrated Mach-Zehnder interferometer which has two monomode waveguides, one of them represents the reference arm and the other represents the sensing arm. A titanium heater with aluminium contacts will be integrated near to the reference arm in order to increase the sensitivity of the sensor by using the thermo-optical effect. A chemo-optical sensitive material to ammonia (its refractive index changes with changing the amount of ammonia that diffuses into it from the ambient air) will be spin coated on the sensing window in the sensing arm.

4.2 Sensor fabrication

The sensor fabrication processes are divided to three main processes which are the MZI waveguide fabrication process, the heater fabrication process and the sensitive layer fabrication process.

4.2.1 MZI waveguide fabrication

With respect to the MZI waveguide, the extensively studied structure is Si / SiO_2 / SiON / TEOS where silicon oxynitride (SiON) is used as core layer. All the information required for SiON deposition using low pressure chemical vapor deposition (LPCVD) were obtained from the last chapter. The first buffer layer is usually grown by thermal oxidation (TO) and must be at least a 2 μm thick oxide layer (the buffer layer must be thick enough to prevent absorption of the guided light by the Si substrate). Finally, a 0.5 μm Tetraethylorthosilicate (TEOS) layer will be deposited by LPCVD.

Fabrication of the waveguides was performed using our clean room facilities. The first step in the fabrication process of the device is the growth of a 2 μm thick SiO_2 lower cladding layer of refractive index 1.46 on a silicon wafer by thermal oxidation in wet atmosphere at an oven temperature of 960 °C and a water temperature 95 °C for 30

h and then oxygen for 5 min [see table (4-1)]. Figure (4-1) shows the relation between the time and the layer thickness during the oxidation process.

.

Oven temperature	960 °C
Water temperature	95 °C
Process time	30 h
Process pressure	1 atm

Table (4-1): Process parameters used in thermal oxidation

Then the silicon oxynitride SiON core layer with a refractive index 1.55 and a thickness of 0.5 μm is deposited by LPCVD at (750-756-760) °C and a pressure of 0.6 mbar. The SiON core layer of refractive index 1.55 can be deposited using flow of Ammonia (NH_3), Triethylsilane ($C_6H_{16}Si$) and Oxygen (O_2) as shown in table (4-2).

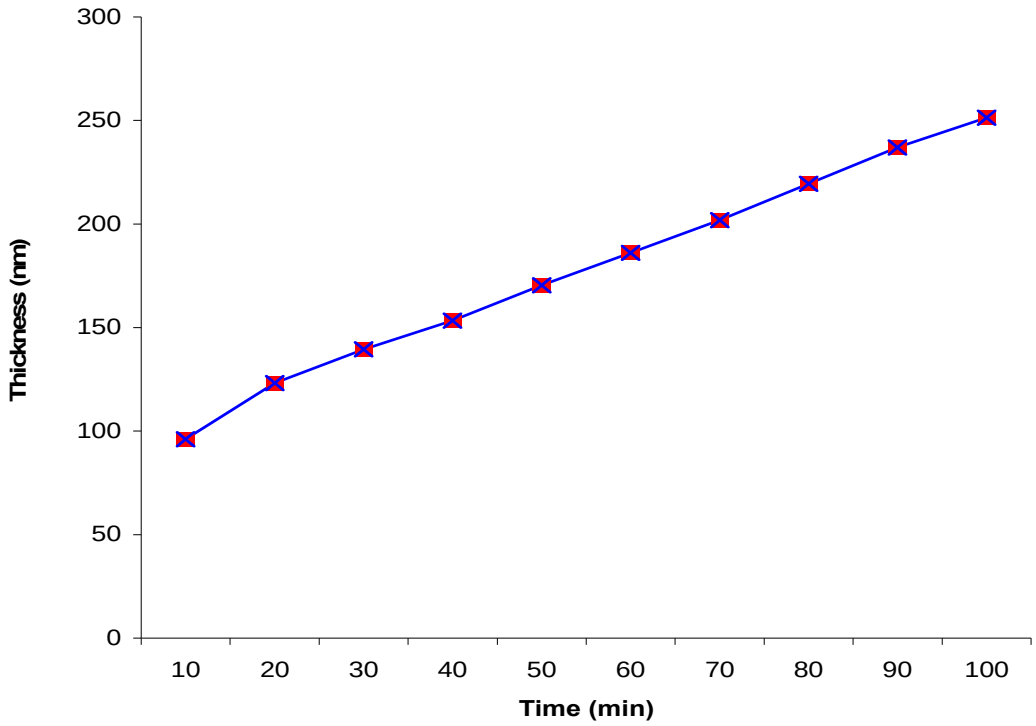

Figure (4-1): The thickness of SiO_2 layers by thermal oxidation at 960 °C / 95 °C

Ammonia (NH_3) flow rate	34.66 %
Triethylsilane (TES) flow rate	85 %
Oxygen (O_2) flow rate	0.158 %
Process pressure	0.6 mbar
Temperature	(750-756-760) °C
Deposition time	47.5 min
Deposition rate	10.526 nm/min

Table (4-2): Process parameters for SiON deposition

Finally, a 0.5 μm Tetraethylorthosilicate [$(C_2H_5)_4SiO_4$] layer with a refractive index 1.46 was deposited by LPCVD at temperature of 721 °C with pressure of 0.3 mbar as shown in table (4-3). Figure (4-2) shows the thicknesses of different TEOS layers with time.

Tetraethylorthosilicate (TEOS) flow rate	24.57 %
Process pressure	0.3 mbar
Temperature	721 °C
Deposition time	85 min
Deposition rate	5.882 nm/ min

Table (4-3): Process parameters used in TEOS deposition

After each step of the last three processes, the average thickness of film deposited on the silicon wafer is measured using an ellipsometer which also was used to calculate the refractive index of the film.

A five point scan was done on the sample, in which the laser picked up five points on the sample and measured the thickness and calculate the refractive index for each of these points. The average of the five points was then taken to get the average thickness and refractive index of the sample.

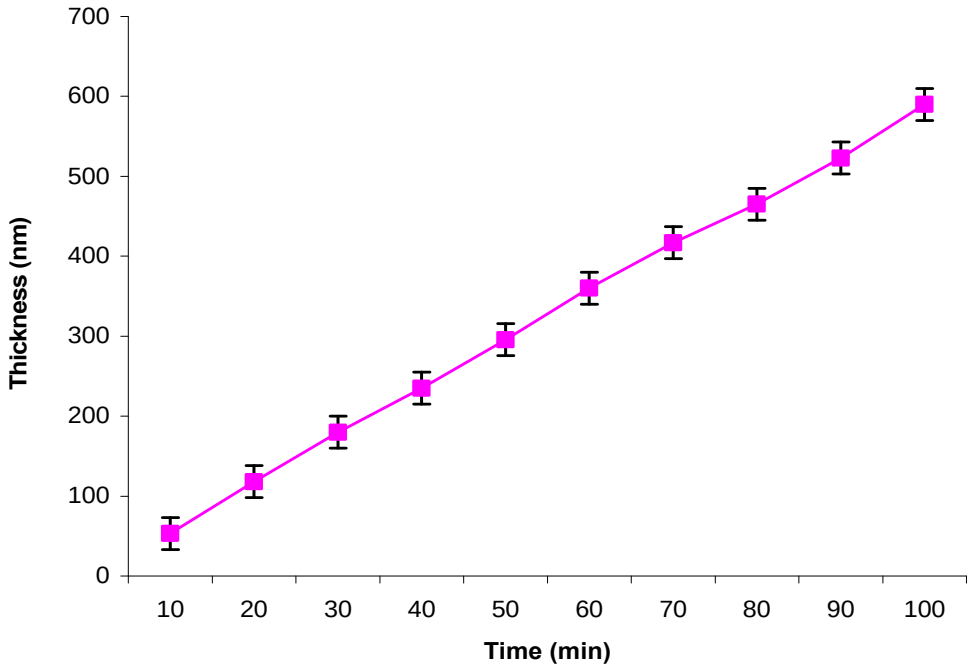

Figure (4-2): The thicknesses of deposited TEOS layers with different times

Then the photoresist was spin coated and the waveguide pattern is defined by optical contact photolithography [see table (4-4)] and transferred to the TEOS layer by reactive ion etching (RIE). This etching process is anisotropic, and it produces vertical sidewalls that guarantee precise control and good reproducibility of the geometry and, accordingly, of the effective lateral index contrast of the waveguide structure as shown in figure (4-3).

Oven	45 min	150 °C
Photoresist adhesion	5 min	N_2
Blow	5 s	1000 rpm
Low spin	7 s	800 rpm
High spin	45 s	4000 rpm
Hot plate	60 s	110 °C
UV exposure	2.5 s	Air humidity is 36 %
Development	40 s	(1 l DI water + 8 g NaOH) in H_2O [2:1]
Oven	45 min	130 °C

Table (4-4): Process parameters used in spin coating and photolithography for TEOS

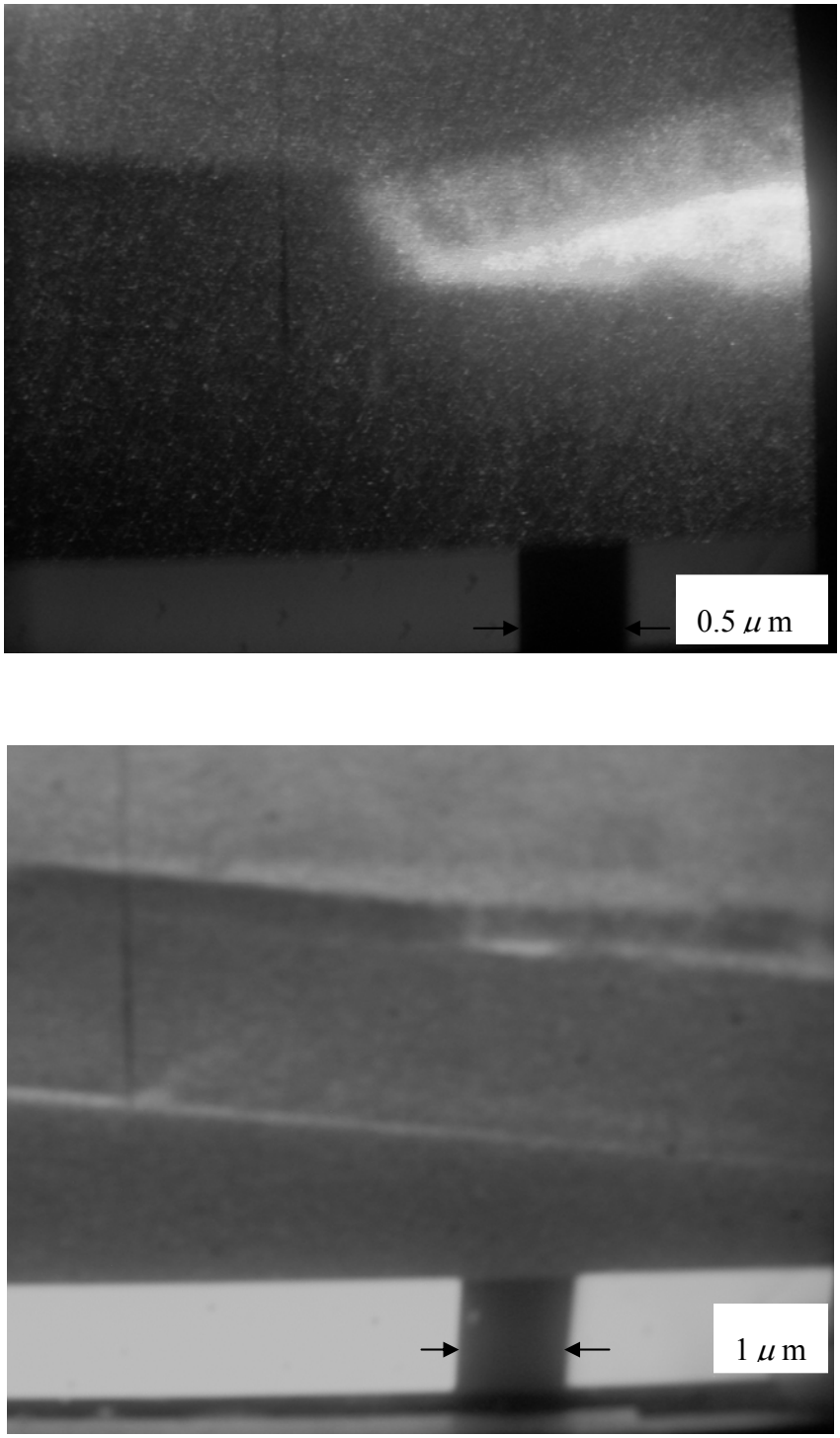

Figure (4-3): SEM images of a cross section of the waveguide revealing the resulting etch profile

This etching is done in a width of 3 μm by reactive ion etching (RIE) to form a rib of 0.4 μm in the TEOS for light confinement in the SiON film below as shown in figure (4-4).

The etching process is done using power equal to 1.4 KW, pressure equal to 25 mTorr and flow of two gases, the first is Argon (Ar) and the second is Trifluoromethane (CHF_3) as shown in table (4-5).

Argon (Ar) flow rate	51.724 %
Trifluoromethane (CHF_3) flow rate	86.3 %
Process pressure	25 mTorr
RF power	1.4 KW
Process time	23.4 min
Etching rate	17.14 nm/min

Table (4-5): Process parameters used in RIE for TEOS layer (the upper cladding)

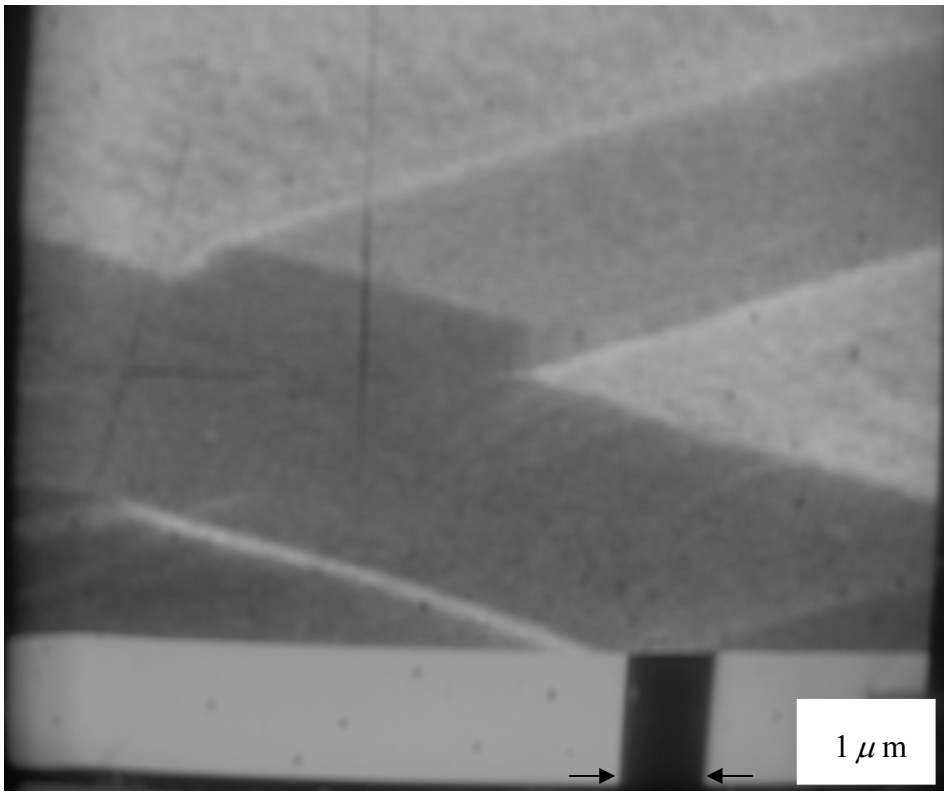

Figure (4-4): SEM image for reactive ion etching (RIE) in TEOS layer

After this, the mask had been removed and a cleaning step had been done to the wafer. The fabrication process flow for SiON planar optical waveguide, as described before, is illustrated in figure (4-5).

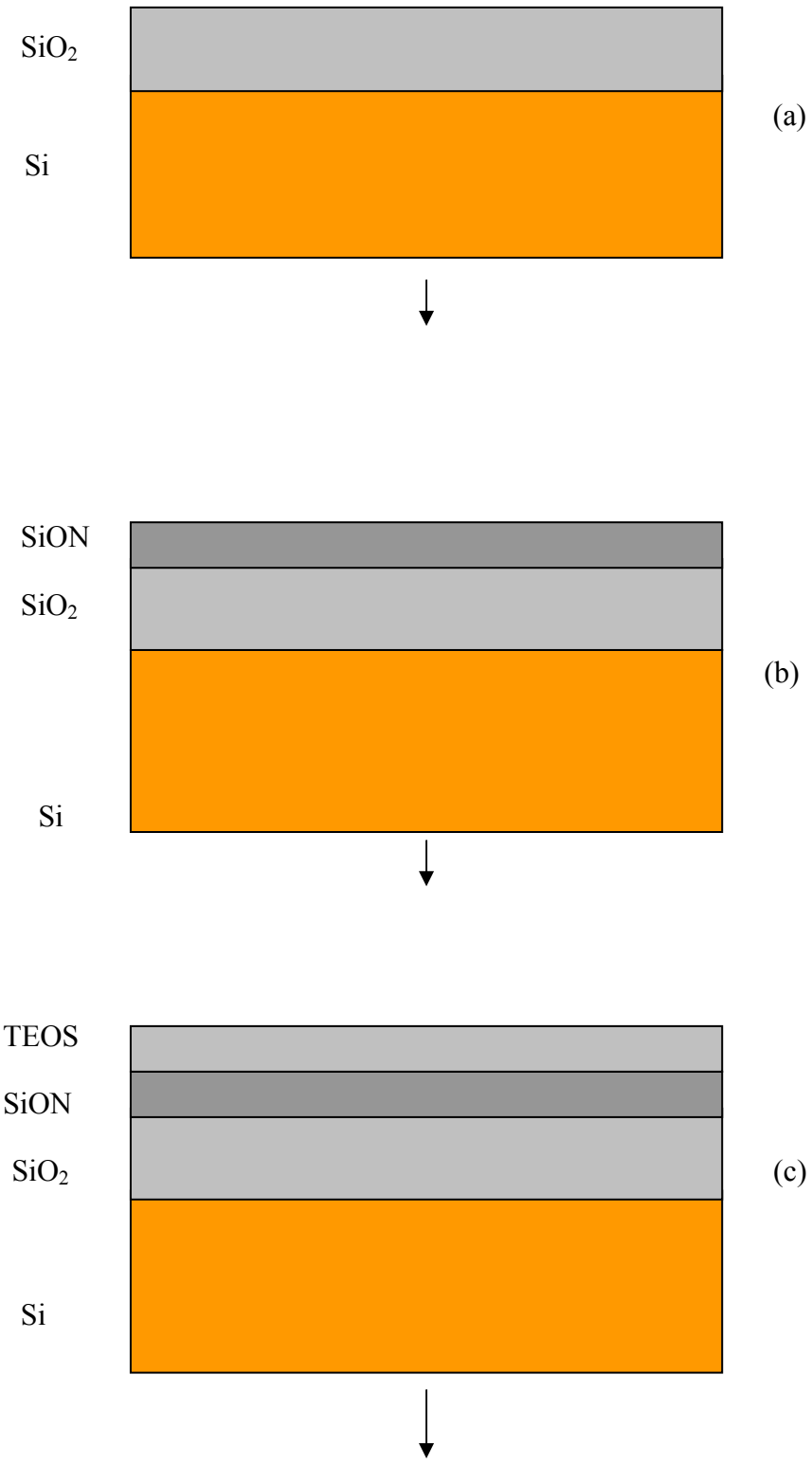
SiO2
Si
(a)
SiON
SiO2
Si
(b)
TEOS
SiON
SiO2
Si
(c)

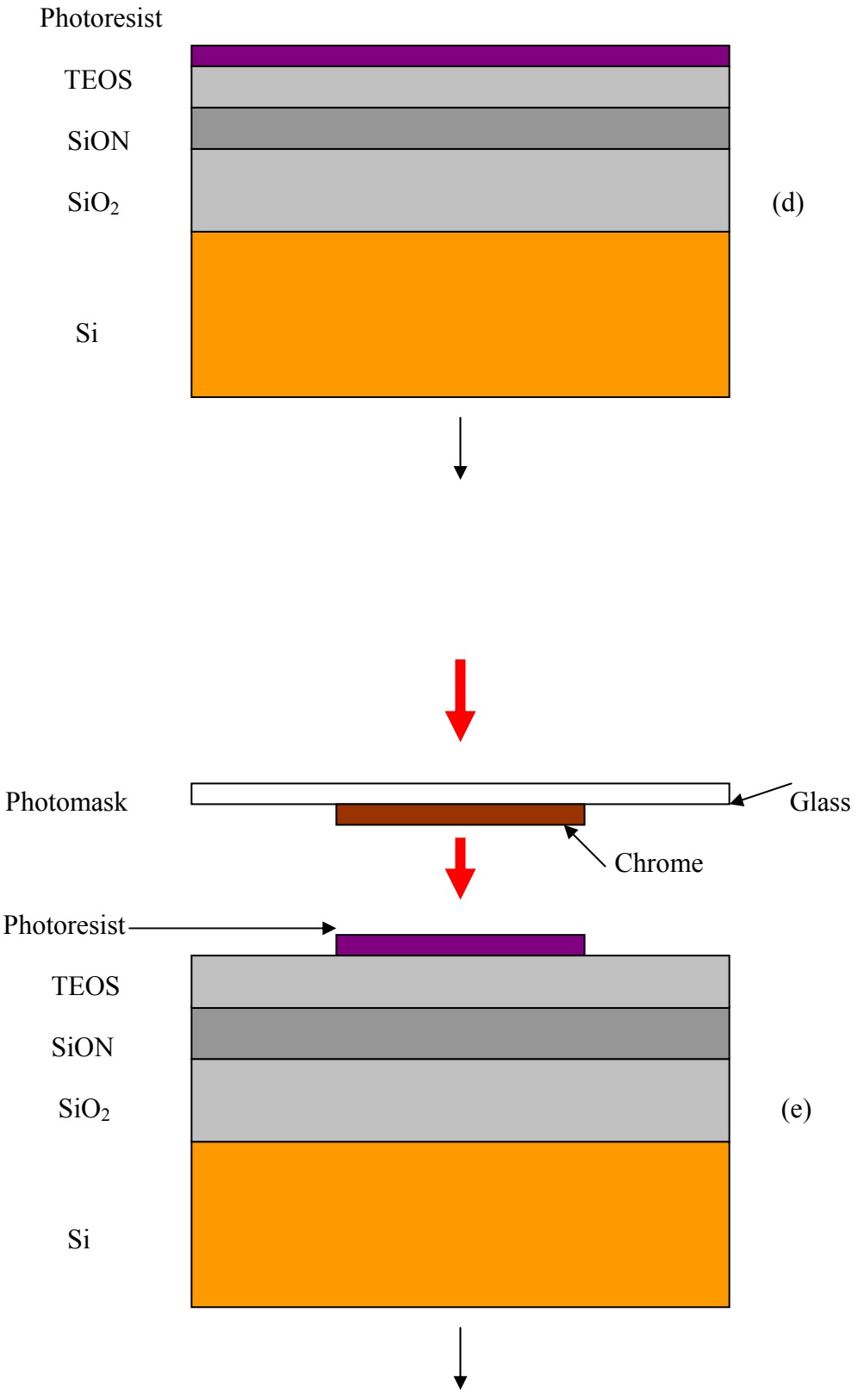
Photoresist
TEOS
SiON
SiO2
Si
(d)
Photomask
Glass
Chrome
Photoresist
TEOS
SiON
SiO2
Si
(e)

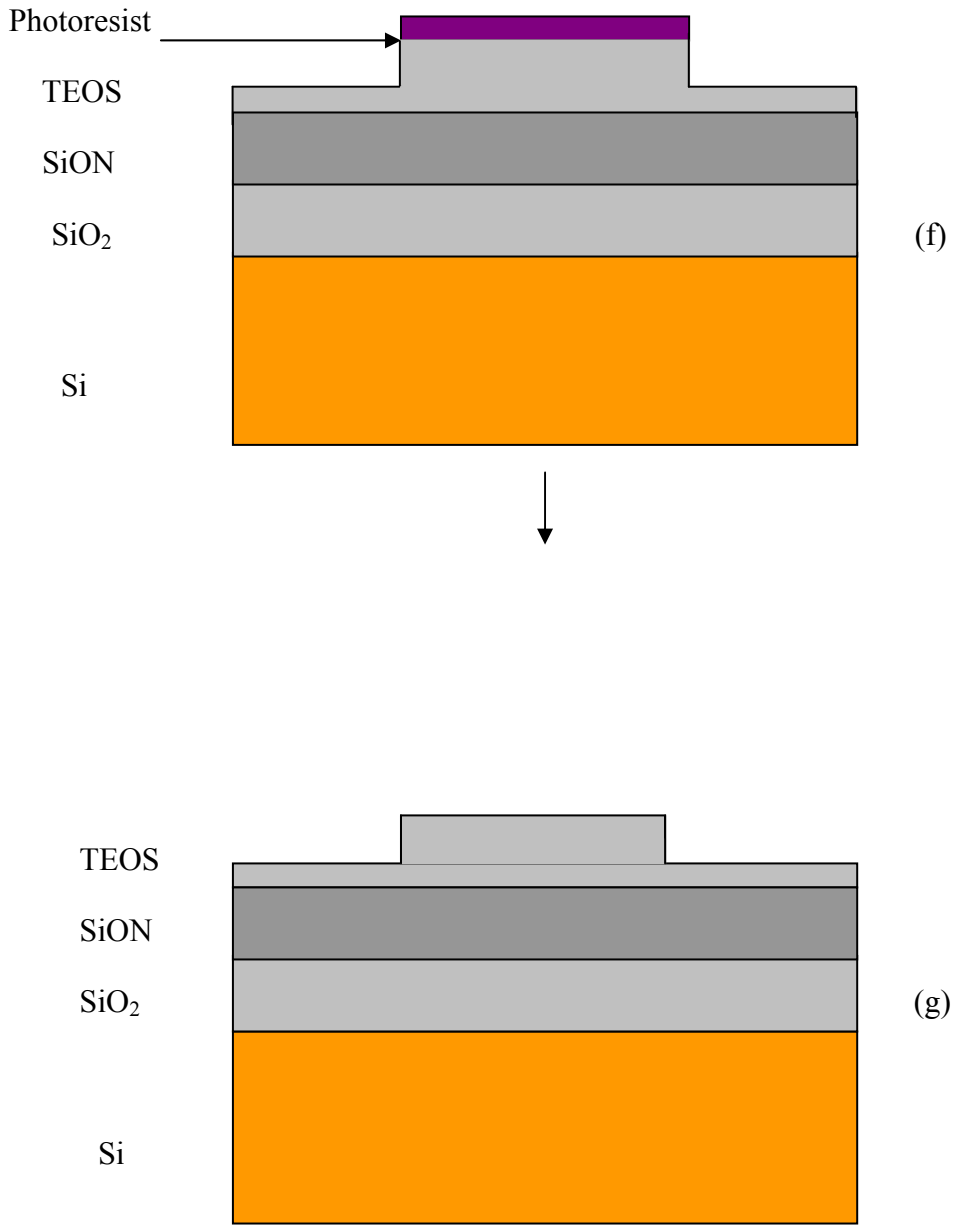

Figure (4-5): Fabrication process flow for high-refractive index contrast SiON/SiO_2 waveguide structures; (a) grown of SiO_2 layer by using thermal Oxidation; (b) depositing of SiON layer by using LPCVD; (c) depositing of TEOS layer by using LPCVD; (d) spin coating the photoresist; (e) defining the waveguide pattern by using optical contact lithography and development processes; (f) forming the rib in the TEOS by using reactive ion etching (RIE); (g) removing the mask and cleaning the wafer

Figure (4-6) shows two SEM images of the MZI waveguide structure. Figure (4-6) (a) represents a cross-section image for the waveguide structure and figure (4-6) (b) represents an image for the splitting point of the MZI waveguide.

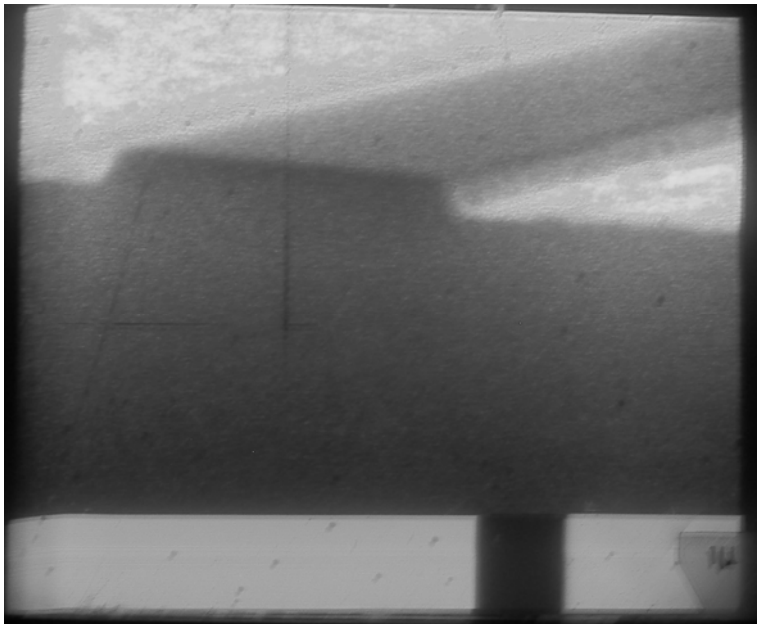

(a)

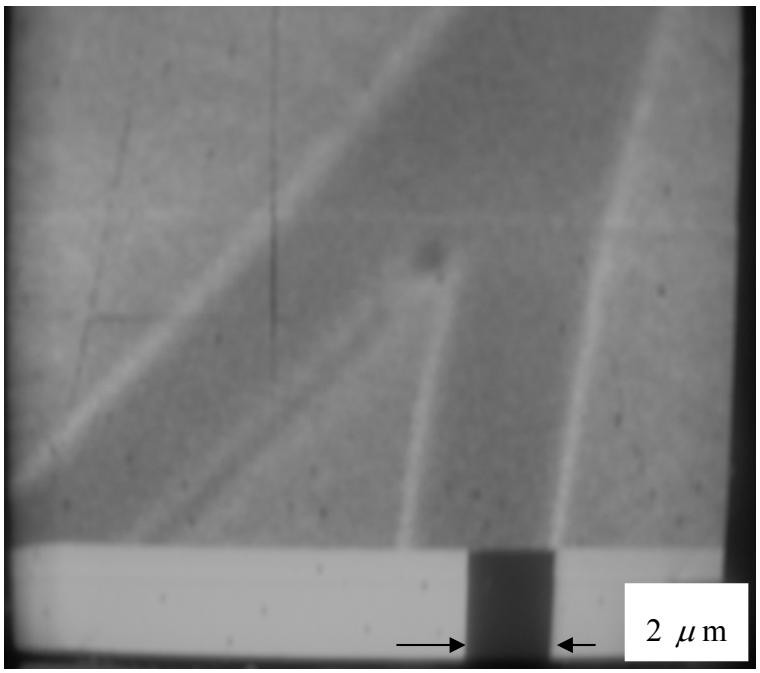

(b)

Figure (4-6): (a) Represents a SEM image for the waveguide structure; (b) Represents a SEM image for the splitting point of the MZI waveguide

Then the waveguide was tested for coupling and propagation loss. The light coming from a red He-Ne laser (633 nm) is coupled into the waveguide by means of end fire coupling and a photodiode detects the light coming out from the waveguide.

4.2.2 Heater fabrication

In order to construct the heater and its contacts the following steps were done:

- A layer of thickness equal to 300 nm of titanium was thermally evaporated on the wafer [see table (4-6)]
- After spinning the photoresist and photolithography process the titanium was wet etched using the materials shown in table (4-7). The etching rate was 50 nm/min and after that the wafer was cleaned

Power increasing	20 s until 5 % power
Wait	20 s
Power increasing	30 s until 8 % power
Delay	5 s
Rate	1 nm/s
Process time	5 min

Table (4-6): Process parameters of Titanium evaporation

DI water	300 ml
Hydrogen peroxide (H_2O_2)	180 ml
Ammonium hydroxide (NH_4OH)	60 ml

Table (4-7): The materials which were used in titanium etching

- As before, a 300 nm aluminium layer was evaporated [see table (4-8)]. After that, the photoresist was spin coated and photolithography was done. Then the aluminium was wet etched using the materials shown in table (4-9). The etching was done at temperature of 60 °C and had a rate of 1 μm/min.
- At the end, the rest of photoresist was removed and a cleaning step was done

Figure (4-7) shows a SEM image for the titanium heater with aluminium contacts. The Mach-Zehnder interferometer, the titanium heater and aluminium contacts all together can be seen in figures (4-8) and (4-9).

Power increasing	40 s until 10 % power
Wait	2 min
Power increasing	60 s until 18 % power
Delay	5 s
Rate	1 nm/s
Process time	5 min

Table (4-8): Process parameters of aluminium evaporation

1	2
840 ml Phosphoric acid (H_3PO_4) 85 % 164 ml DI water 38 ml Nitric acid (HNO_3) 65 % 3 ml Antarox	1120 ml (H_3PO_4) 224 ml DI water 50 ml HNO_3
[700 ml of (1) + 1400 ml of (2)] at 60 °C	

Table (4-9): The materials which were used in aluminium etching

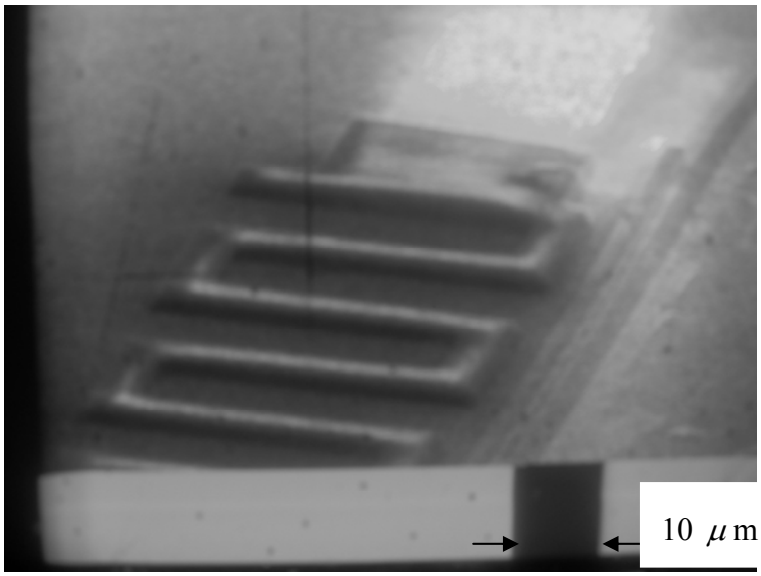

Figure (4-7): A SEM image for the titanium heater with aluminium contacts

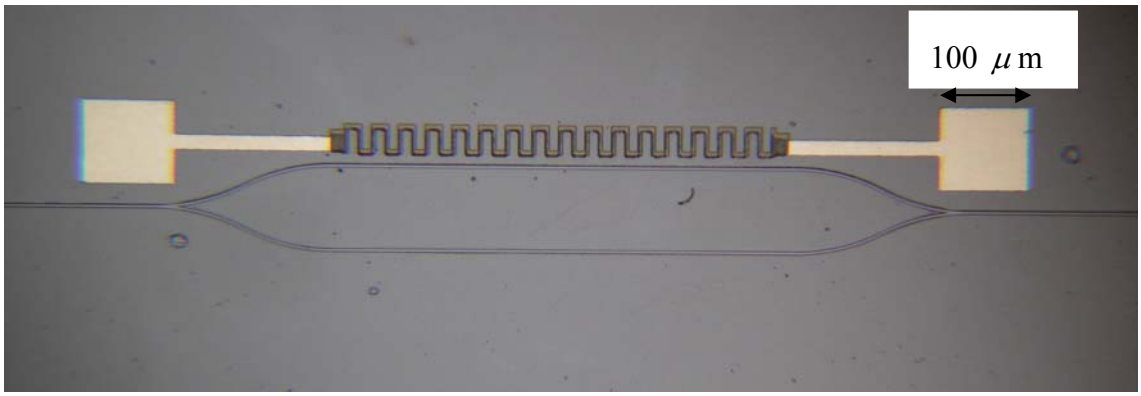

Figure (4-8): A microscopic image for the structure consisting of MZI, the heater and the contacts

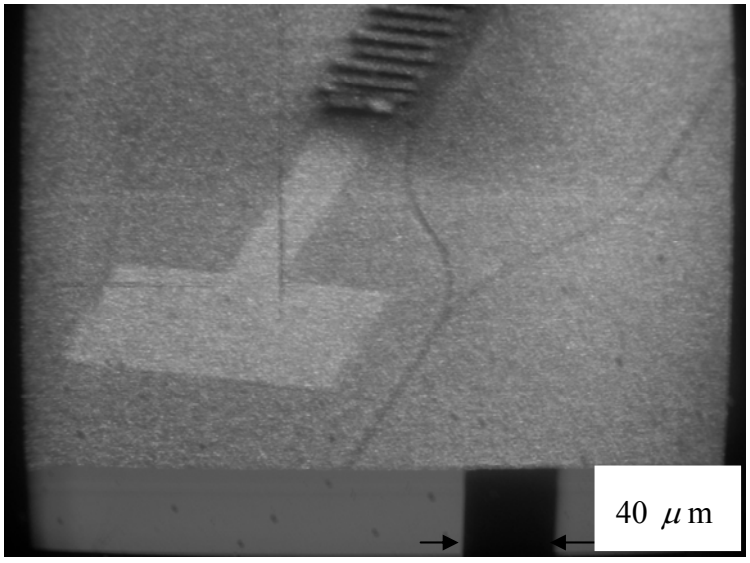

Figure (4-9): A SEM image showing the structure of the sensor

4.2.3 Sensitive layer fabrication

To build a sensor, sensitive material had to be selected that changes its refractive index in response to the presence of a targeted chemical substance, such as ammonia in ambient air. One of the choices was a thin film of polymer doped with an appropriate indicator dye. Dye-doped polymers are traditionally used in optical chemical sensors, or optodes, based on a change in optical absorption. In our case, however, the sensitive optical parameter to be measured was not the absorbance but the refractive index.

As a sensitive layer, the polymer polymethyl methacrylate (PMMA) was used, which can easily be dissolved in a number of commercial solvents and mixed with various indicator dyes. It can also easily be processed into a thin layer by spin coating. As an indicator dye that is sensitive to ammonia, Bromocresol Purple (BCP) was selected [58].

The BCP was added to a solution of PMMA at a concentration of 5.5 % weight concentration of the BCP in PMMA. The solution was filtered by a filter with 0.5 µm pore size. Then it was spin coated at 4000 rpm for 60 s to give a layer thickness 200 nm [see figure (4-10)] and backed on a hot plate for 60 s at 180 °C.

The following defines is the photolithography process. A UV lamp exposed the samples for 3 min. The UV beam is aligned on the pattern from the mask. After all the samples were exposed to UV, the samples were developed using methylisobutyl ketone (MIBK) in isopropanol (IPA) [1:3 MIBK to IPA] for 30 s. Following the development process, the samples were rinsed with DI water (de-ionized water). Baking the samples in a convection oven at 95 °C for 30 min [see table (4-10)]. The final thickness of the PMMA-BCP layer was close to 200 nm and its refractive index was 1.48.

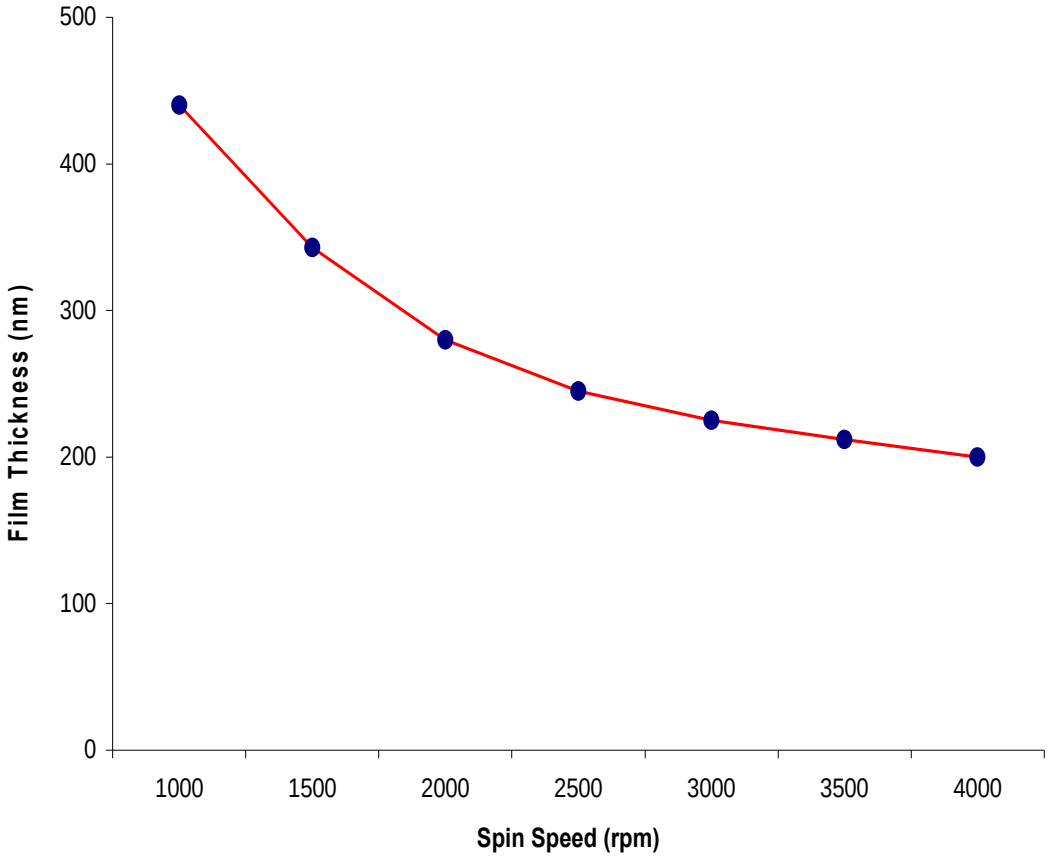

Figure (4-10): The film thickness vs. spin-speed of the sensitive layer

Oven	45 min	150 °C
For layer adhesion	5 min	N_2
Blow	5 S	1000 rpm
High spin	60 S	4000 rpm
Hot plate	60 S	180 °C
UV exposure	3 min	Air humidity 39 %
Development	30 S	[1:3 MIBK to IPA]
Oven	30 min	95 °C

Table (4- 10): Process parameters used in fabricating the PMMA-BCP sensitive layer

4.3 Experimental results

The results are split into three main areas of study. The first is studying if the waveguide has an expected behavior concerning insertion losses, propagation losses, wavelength response and light confinement.

The second is studying the modulation of light using thermo-optical effect by the heater in order to increase the sensitivity.

The third is studying the detecting of ammonia by studying the change in intensity of the output port of the MZI.

4.3.1 Waveguide characterization

If the cladding layers are properly tuned, both in refractive index and thickness, losses have a minimum at the operating wavelength (633 nm). If there were any variation of these parameters, minimum losses will shift from the operating wavelength.

Using end-fire coupling as in the experimental setup shown in figure (4-11), losses in test waveguides were measured. The losses sharply increase as waveguide gets narrower. It has to be taken into account that total losses here include attenuation and

insertion losses. Care has been taken to minimize injection losses due to modal mismatch, reflections and edge defects or irregularities. The insertion loss measurements have been calculated equal to 1.4 ± 0.2.

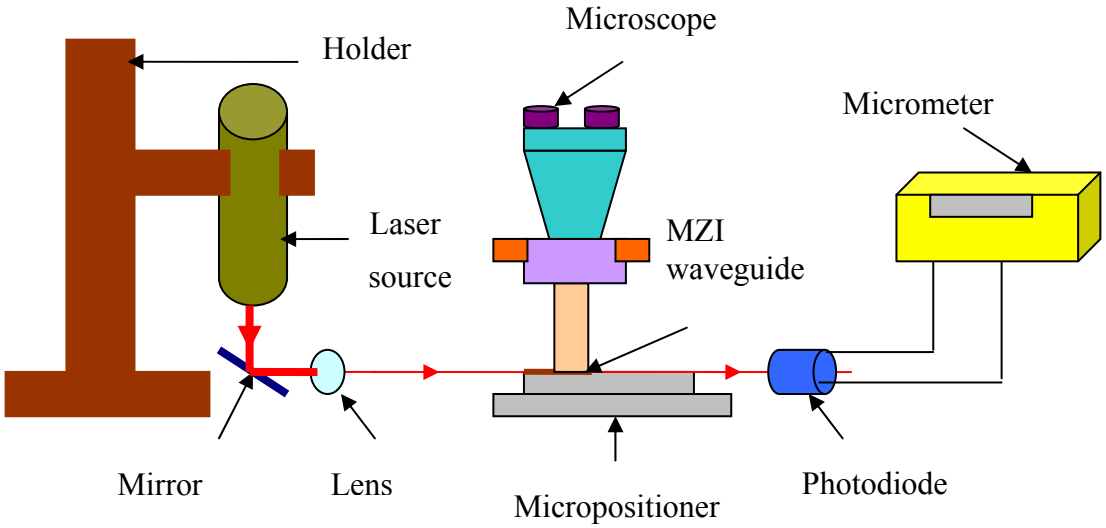

(a)

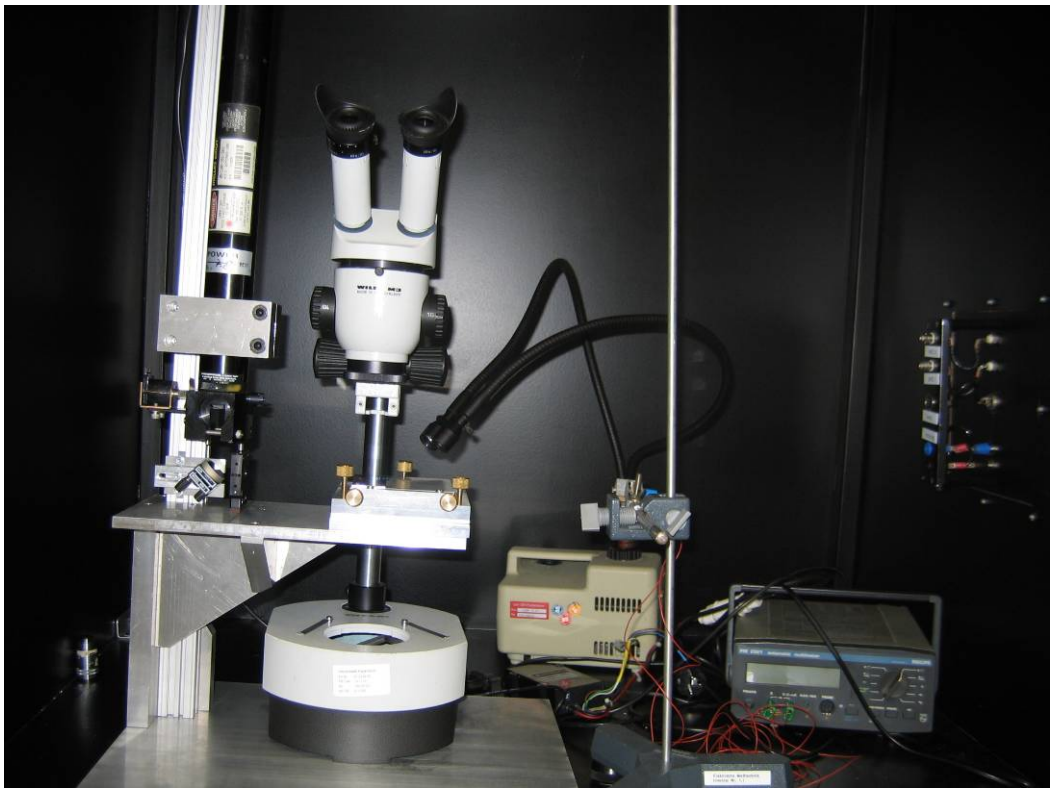

(b)

Figure (4-11): Experimental setup for coupling light to the waveguide by using end fire method (a) Sketch; (b) Real image

Propagation loss measurements have been performed by measuring the intensity of the transmitted light in waveguides at different lengths. From the fit results a propagation loss coefficient of about 1.5 ± 0.3 dB/cm. These losses are independent on the coupling losses. Figure (4-12) shows the normalized intensity with respect to the horizontal direction of the waveguide.

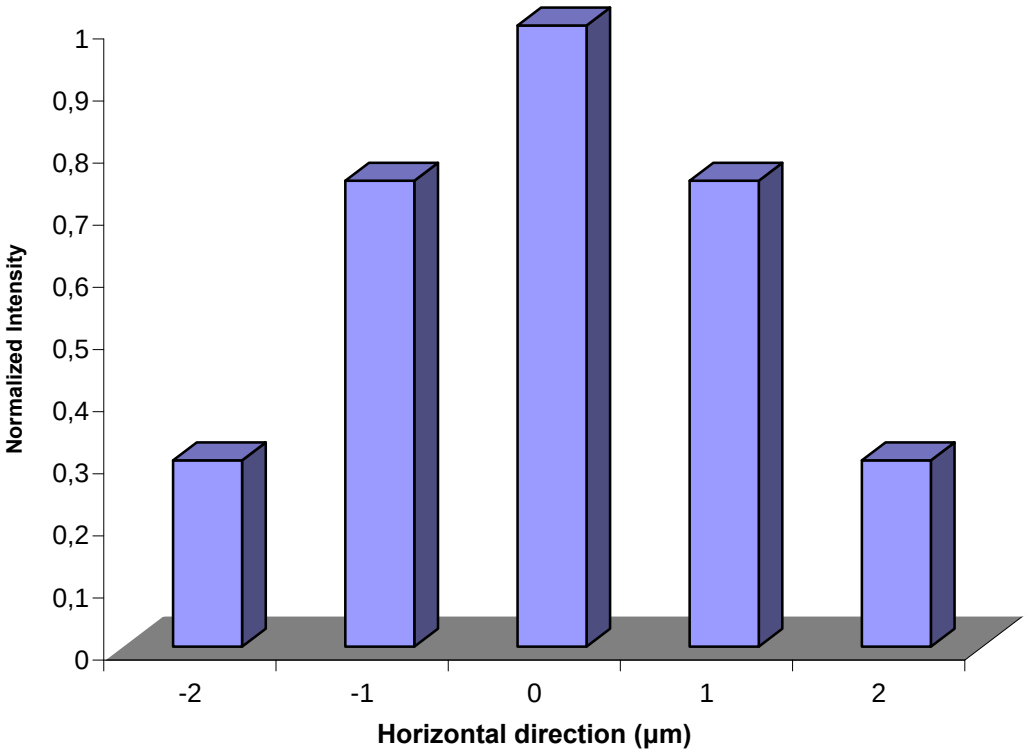

Figure (4-12): The normalized intensity vs. the horizontal direction

4.3.2 Light modulation

By heating near the reference arm of the MZI waveguide using the metal heater (titanium heater) the refractive index of the reference arm will change, and hence, there will be a phase difference between the two optical branches, and hence, the output intensity will be changed, and the heating process is done by using a voltage controlled power supply. In general, this power is inversely proportional to the response time. The response time of this device was calculated to be in the range of several milliseconds.

If the phase change of the waves in the two arms is reaching π , the optical output power will be zero. The phase change $\Delta\varphi$ can be expressed as follows [59], [60]:

$$\Delta\varphi = \frac{2\pi}{\lambda}\frac{dn}{dT}\Delta TL \tag{4-1}$$

Where λ is the wavelength of the transmitted light, dn/dT is the thermo-optic coefficient of the silicon substrate, ΔT is the temperature difference between the two waveguides and L is the heater length.

Taking into consideration the high thermal conductivity of the silicon substrate (150 W/mK) and the small distance between the heater and the reference arm of the Mach-Zehnder interferometer (3 μm) and knowing that the thermo-optic coefficient for the SiON-based waveguide is equal to $1.2\times10^{-5}\ {}^{\circ}c^{-1}$, the transmitted light wavelength is 633 nm and the heater length is 5.5 mm long, the temperature difference required to give the different phase difference between the signals traveling in the two arms of Mach-Zehnder interferometer can be calculated. Then a temperature difference of 5 $^{\circ}C$ is needed for having a phase difference equal to π (zero output optical power) and a temperature difference of 10 $^{\circ}C$ is needed for having a phase difference equal to zero (2π) and this gives maximum output optical power.

For most materials, the resistivity changes with temperature. If the temperature range is not too large, the resistivity is a linear function of the temperature.

As the temperature of the heater is varied, its resistance changes due to:

- The temperature dependence of the resistivity
- The thermal expansion of the heater

For titanium, which is used here as a heater, the thermal expansion effects can be neglected in comparison with the resistivity change. Since only the change in resistance of the material is important, the overall resistance of the heater has a similar dependence on the temperature:

$$R = R_0\left[1+\alpha\left(T-T_0\right)\right] \tag{4-2}$$

where α is the temperature coefficient of resistance (TCR) and has a value of 0.0038 $^{\circ}K^{-1}$ for titanium (the material of the heater), T_0 is the reference temperature, T is temperature of interest, R_0 is the resistance at reference temperature and R is the resistance at temperature of interest where the influence of the temperature on the resistance of the heater is plotted in figure (4-13). According to the plot, the resistance is almost linearly increasing at this temperature interval.

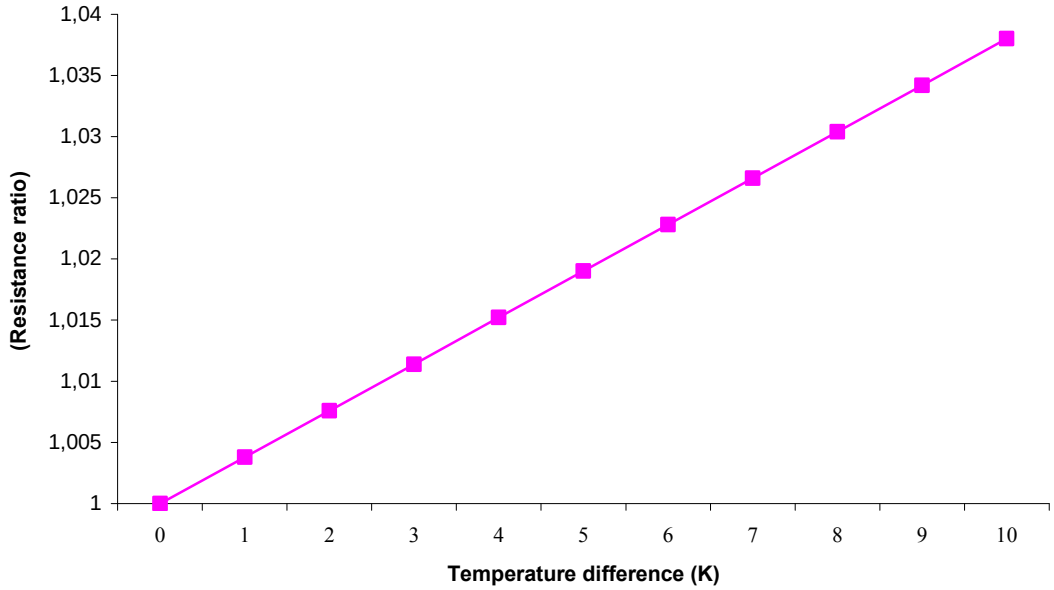

Figure (4-13): The resistance ratio (R/R_0) as a function of temperature difference ($T - T_0$) for the titanium heater

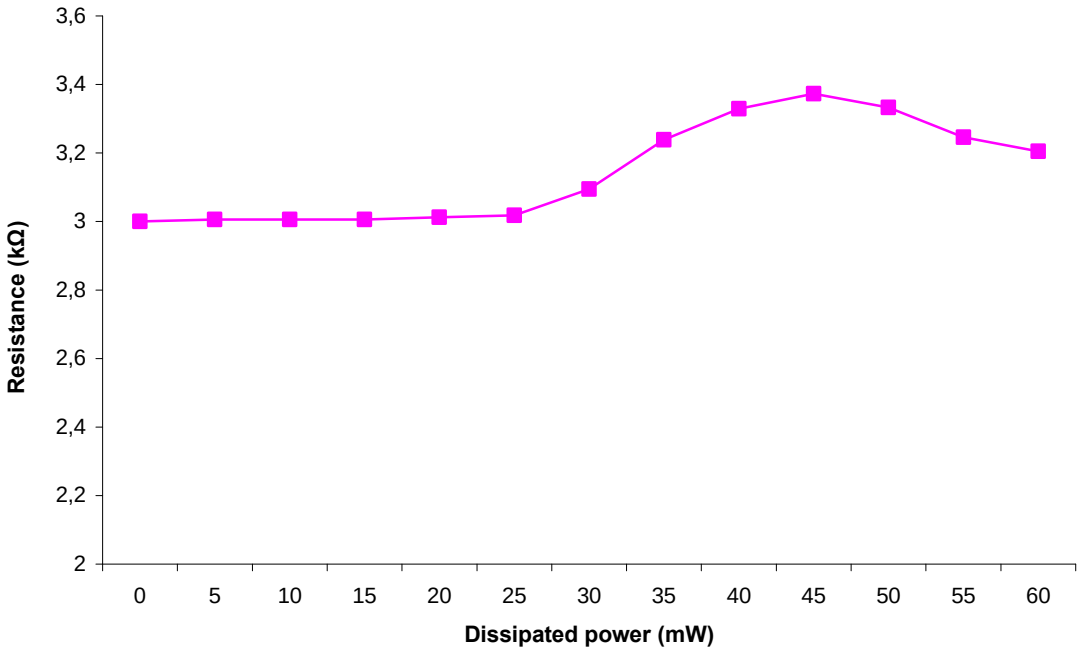

Figure (4-14): Resistance of the heater against the dissipated power

However, changes in the resistance of the heater are observed during heating as shown in figure (4-14). The resistance increases rapidly when more than 25 mW is

dissipated. Heating above 60 mW is destructive (the heater can not withstand more than 60 mW).

Figure (4-15) shows the effect of applying the heating power on the transmission intensity of the light at 633 nm wavelength. As the power is increased, there is an increase in transmission that peaks at 7 mW (constructive interference). A destructive interference in the Mach-Zehnder device was achieved at 39 mW as indicated by the transmission minimum. The maximum sensitivity was achieved at 24 mW.

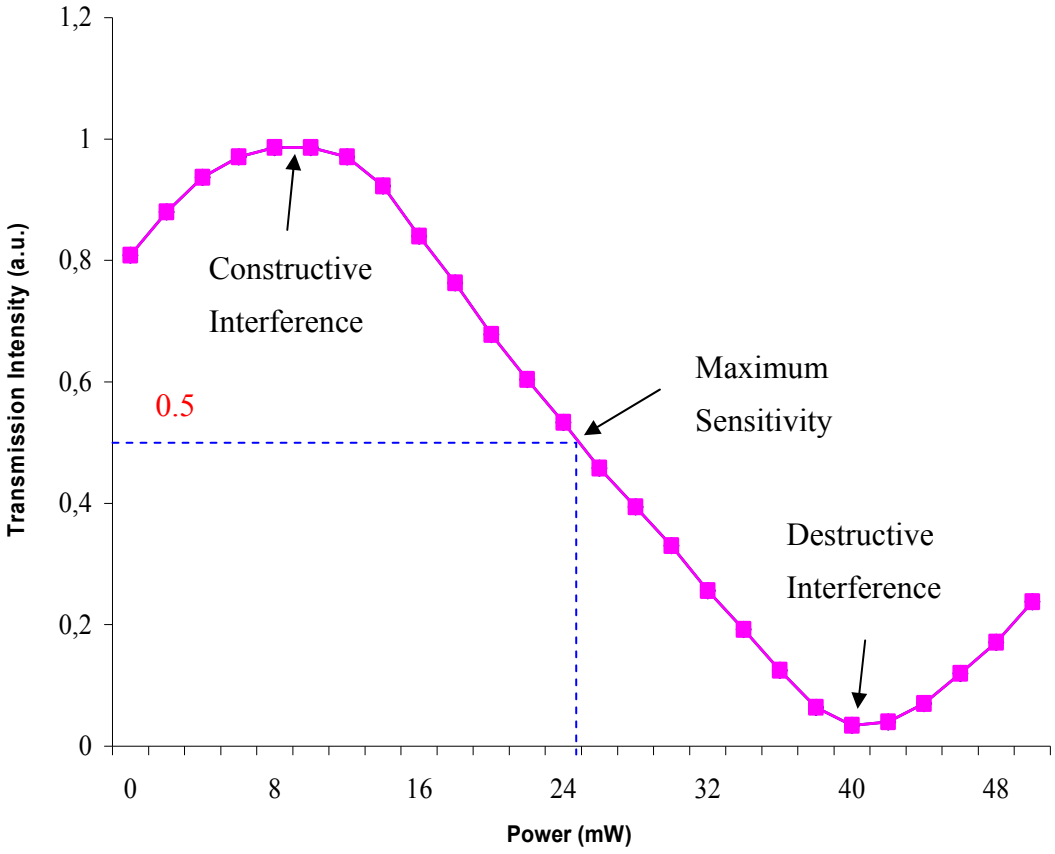

Figure (4-15): Transmission intensity against electrical heating power

4.3.3 Ammonia sensing

The sensor under study relies on detection of a refractive index change at the ammonia sensitive layer. This device falls into the so-called evanescent field sensing technology wherein an electric field penetrates into the layer above the waveguide and serves as a probe beam. The reversible reaction has associated with a refractive index change to which the evanescent field is quite sensitive.

When the sensitive layer was exposed to ammonia a change in its absorption was observed. An initially almost colorless film appeared to be yellow (the absorption increase) after exposure and it was accompanied by an increase in the refractive index at 633 nm of maximum value equal to 0.004 [as shown in figure (4-16)], originating a change in the effective refractive index of the guided mode and, therefore, in the MZI sensor output.

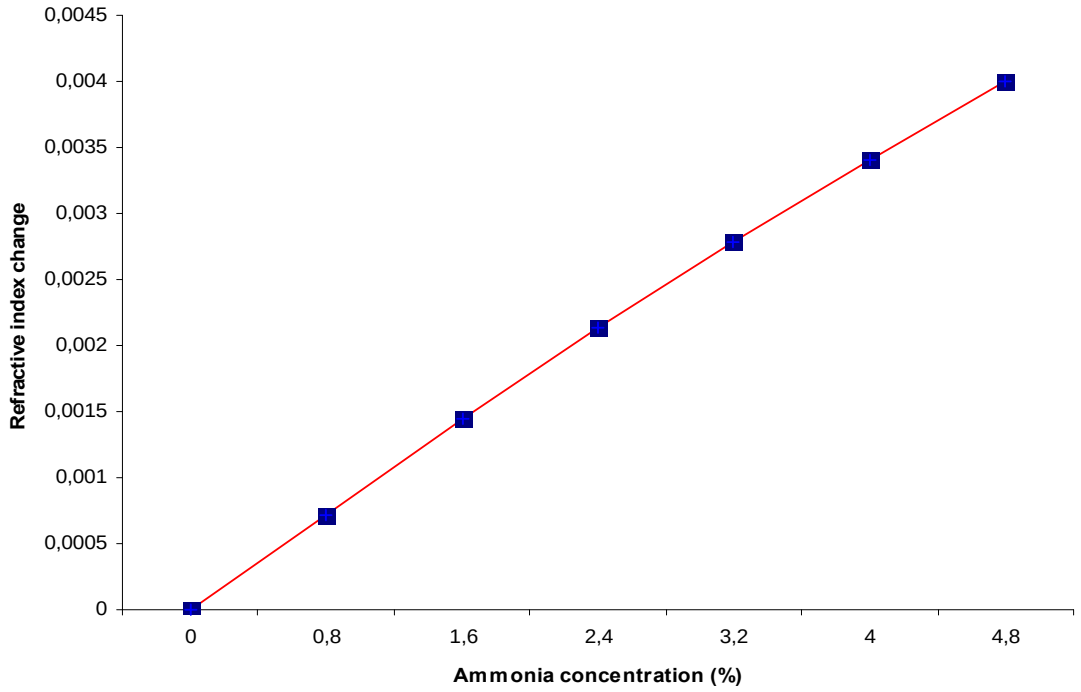

Figure (4-16): The calculated refractive index change in the sensitive layer during exposure to ammonia

The experimental setup shown in figure (4-17) is used for ammonia detecting measurements. It consists of an external red He – Ne laser source, single mode silicon optical fiber is used to couple the light directly into the waveguide inside the box, lens for light beam converging, glass box with 7 holes (one of them is used to pump the ammonia into the box, the second hole is used to pump the nitrogen into the box, the third hole is used to pump the gases out the box, two holes are used to connect the wires of the heater to the power supply and the last two holes are used to connect the photodiode to the micrometer), mass flow controller to control the ammonia concentration, photodiode to detect the light coming at the output port of the Mach-Zehnder interferometer, microscope, micrometer, micropositioner and power supply. All measurements were made at room temperature.

The hole which is used to pump the gases out the box is located at the opposite side of the inlet tube which is used to pump the ammonia into the box so that ammonia flows parallel to the sensitive surface. The gas must flow parallel to the surface to minimize sample vibrations.

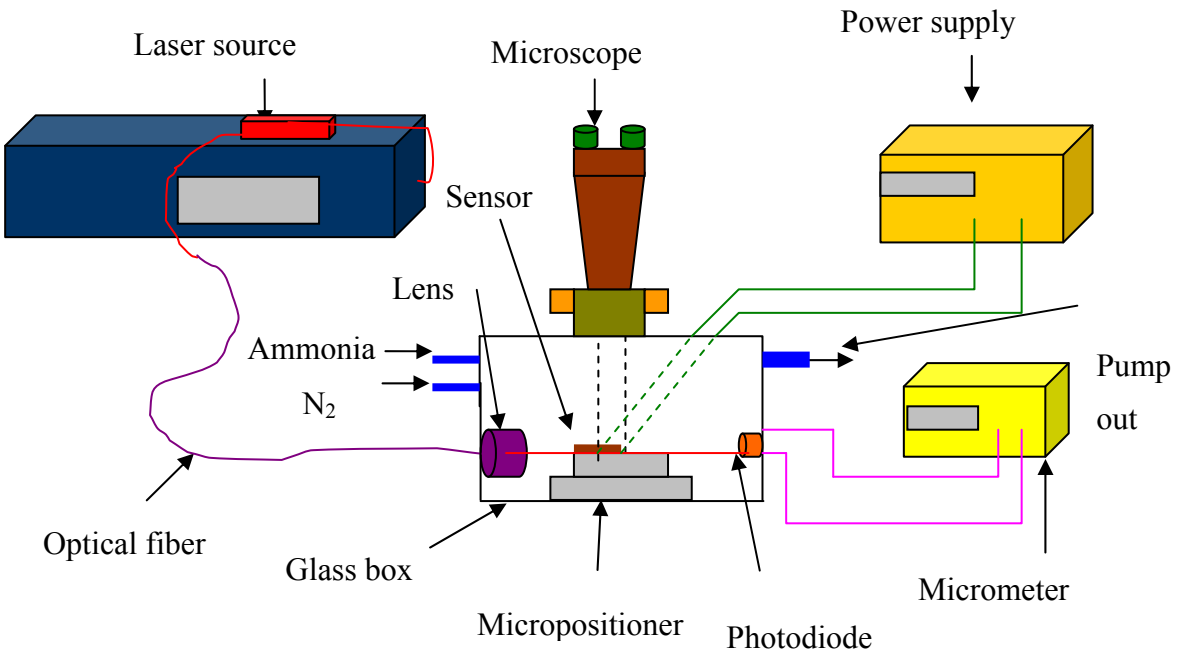

(a)

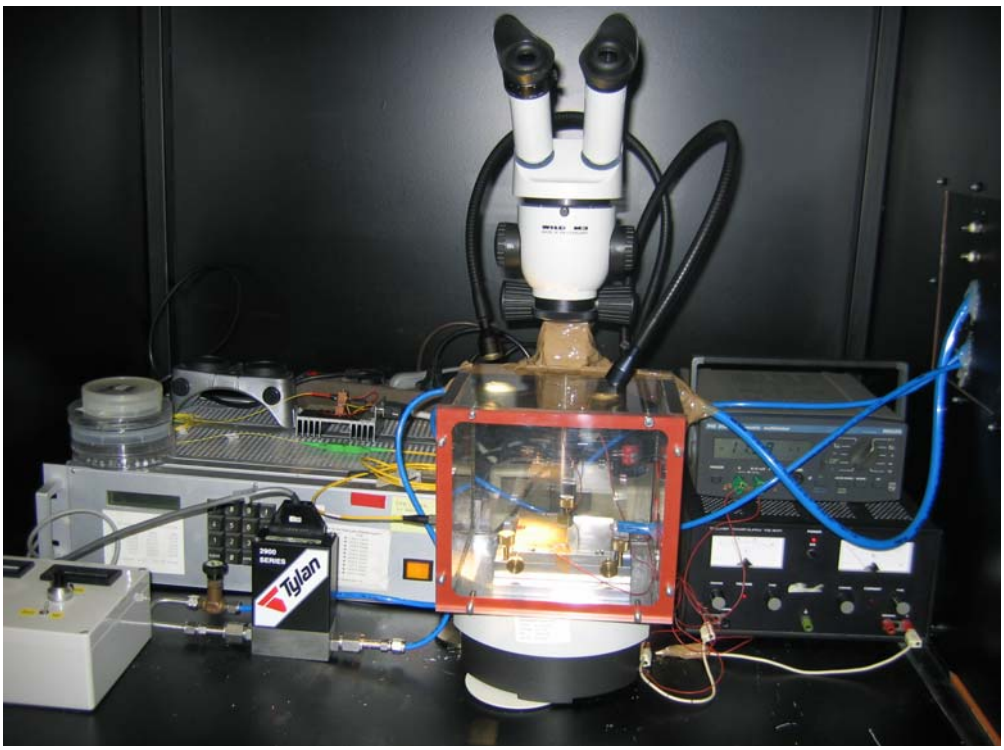

(b)

Figure (4-17): The experimental setup used for ammonia sensing measurements; (a) sketch; (b) image

Light from an external laser source was coupled into the input port of the Mach-Zehnder interferometer through a single mode optical fiber by using a lens, a microscope objective and a micropositioner. The intensity at the output port was detected by using a photodiode and a micrometer.

An electrical power equal to 24 mW (which gives maximum sensitivity) was given to the heater for thermal tuning. And then, the glass box was closed carefully and ammonia was pushed into the box. The total length of the sensitive layer was exposed to the ammonia stream.

The recovery time is large in the case of ammonia with dry air and acceptable with wet air. The best way to test the sensor is mixing the ammonia with air and with extra water vapor and transfer the mixture into the glass box which initially had been filled with air at atmospheric pressure (the higher relative humidity in the air the shorter the time required for recovering change in the refractive index of the sensitive layer after exposure).

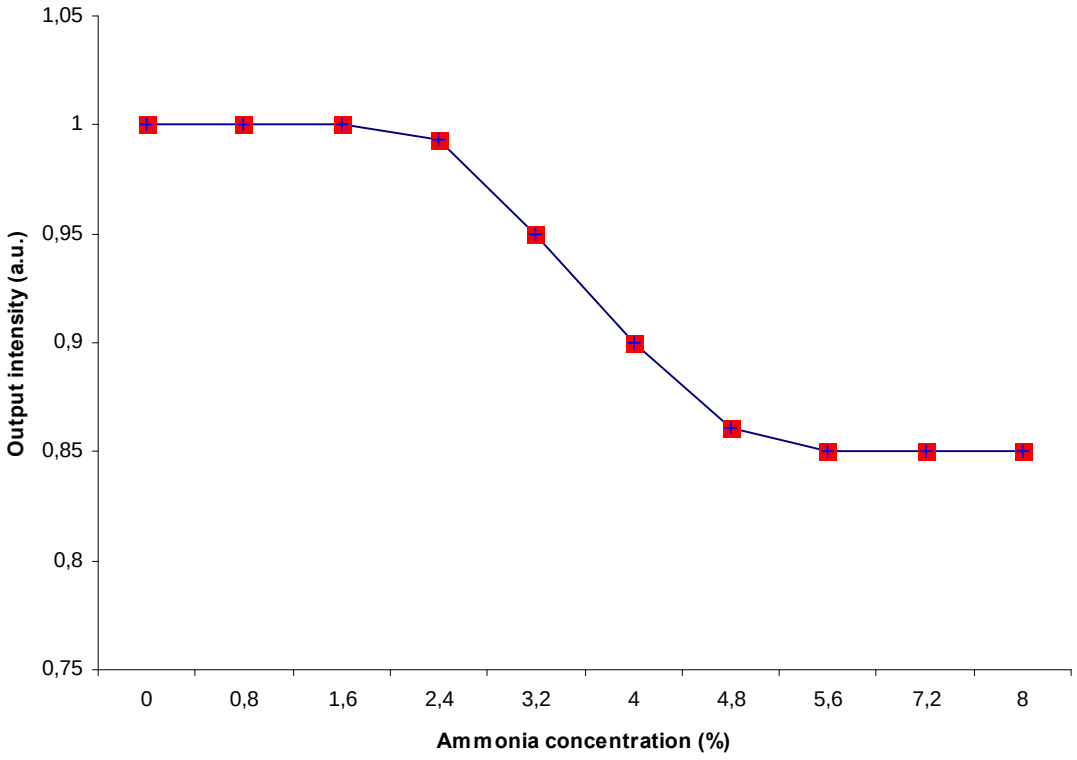

Figure (4-18): Calibration plot for the sensor response represented by the output intensity as a function of ammonia concentration

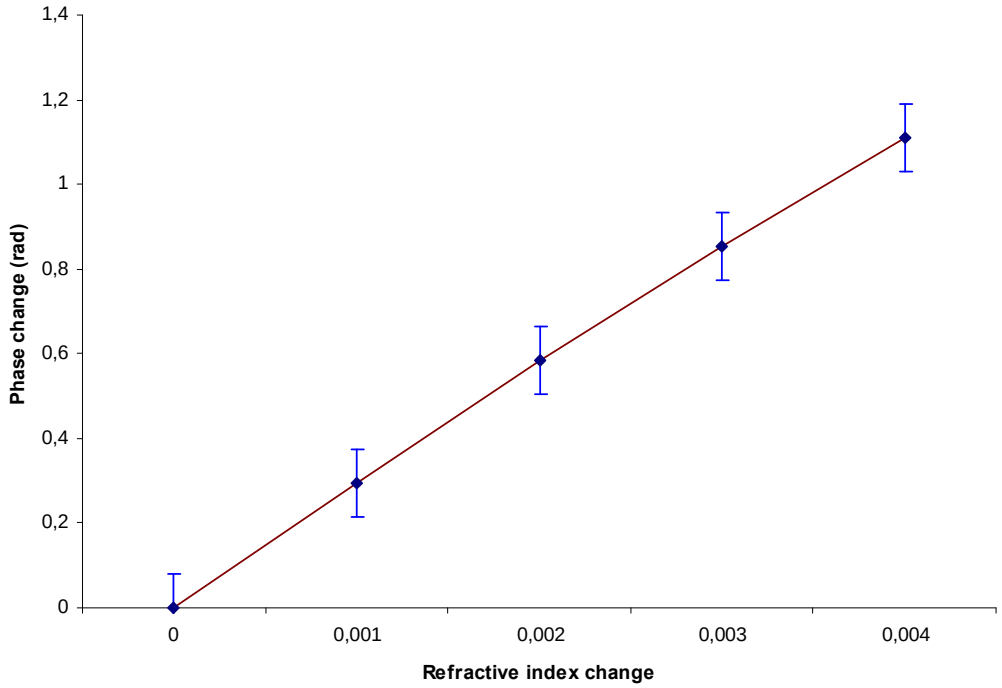

Figure (4-19): The phase change $\Delta\varphi$ as a function of the change in the refractive index of the sensitive layer

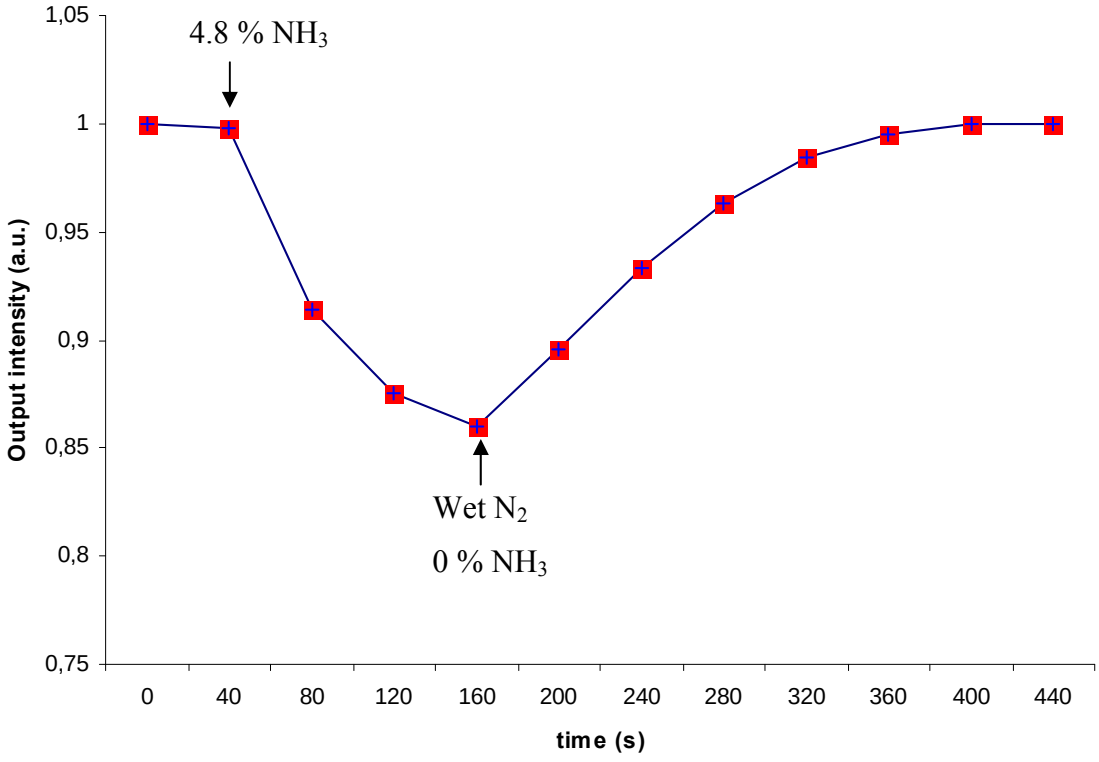

Figure (4-20): The sensor response as a function of response time

Figure (4-18) shows the sensor response represented by the output light intensity of the MZI as a function of the ammonia concentration. From this figure, the sensitivity of the sensor could be calculated to be close of 2.4 % (ammonia concentration below 2.4 % could not be detected).

The calculated phase change $\Delta\varphi$ between the light beams propagating in the two MZI arms as a function of the change in the refractive index of the sensitive layer is shown in figure (4-19).

With respect to the response and recovery times, it was found that the response time is close to 120 sec and the recovery time is close to 240 sec as shown in figure (4-20).

5 Conclusions

Low pressure chemical vapor deposition was optimized. This optimization is concerning with the deposition rate and the homogeneity of the layers. The deposition at 740 °C was not good because the deposition rate was small and the thickness variation along the wafer was large (18.7 %). This deposition can not deposit thick layers at short time since the deposition rate was only (0.9 nm/min). The deposition at 760 °C was the best because it had better results and it is also preferred on deposition at 780 °C since the temperature is lower. To decrease the thickness variation along the boat at a temperature of 760 °C the temperatures of the heating zones were optimized. The front zone temperature was optimized to 750 °C, the middle zone temperature was optimized to 756 °C and the back zone temperature was optimized to 760 °C. The homogeneity of the silicon nitride was better at an ammonia flow rate of 15 % than at an ammonia flow rate of 30 % but there was no much difference of the refractive index in both cases. The thickness variation along the boat was optimized to 15.1 % in the case of silicon nitride and the deposited layers on the wafers were mechanically stable. In the case of silicon oxynitride the homogeneity was better than with silicon nitride since the thickness variation along the wafer with silicon oxynitride was 0.83 %. It is found that the higher the oxygen flow rate the higher the deposition rate and the lower the refractive index of the silicon oxynitride.

An optical microsensor based on silicon microelectronics technology was developed. It makes use of an integrated Mach-Zehnder interferometer configuration fabricated with a silicon oxynitride waveguide. The main function of this sensor was the detection of ammonia gas. The sensor consisted of an integrated MZI and an integrated titanium heater with aluminum contacts. The titanium heater was integrated near one arm from the two arms of MZI (the reference arm) and on the second arm (sensing arm), a sensing window was created. A chemo-optical sensitive material to ammonia (PMMA-BCP) was spin coated on the sensing window in the sensing arm.

Due to total internal reflection at the waveguide interfaces, light coupled into the waveguide core is confined and guided. The coupled light processes an evanescent field distribution that decays exponentially into both the substrate and cover layers.

Interaction of a target analyte with the chemo-optical selective coating on the sensing window produces a phase change in this guided optical wave. The phase delay introduced to the guided wave as a result of interaction with a target analyte is easily detected by means of an optical circuit known as an interferometer such as Mach-Zehnder interferometer.

For sensing applications, waveguide structure must verify two conditions: it has to be monomode and it should show a high surface sensitivity. To obtain a single mode behavior, large attenuation losses for the higher order modes must be done by calculating the parameters of the waveguide carefully using beam propagation method

(BPM). Concerning the second condition, sensitivity increases by increasing the strength and the distribution of the evanescent field. In this work, designing the monomode silicon oxynitride waveguide was done using imaginary distance beam propagation method (ID-BPM).

The planar monomode MZI waveguide structure was fabricated using standard technology (Si / SiO_2 / SiON / TEOS) and had been designed in order to obtain a high intensity of the evanescent field close to the waveguide surface (high surface sensitivity).Silicon oxynitride with low optical losses can be made with good uniformity and reproducibility of refractive index and layer thickness.

As a sensitive layer, a PMMA film is doped with bromocresol purple (BCP), an indicator dye, that causes the index of refraction of the film to vary with the amount of ammonia that diffuses into the film from the ambient air.

This thesis was developed in five chapters which covered a literature review on the low pressure chemical vapor deposition and its application in optical waveguide based chemical sensors. The first chapter was an introduction. The second chapter was the theoretical considerations concerning the design of the sensor. The third chapter was optimization of low pressure chemical vapor deposition of silicon nitride and silicon oxynitride. The fourth chapter was concerning the sensor fabrication and the experimental results. The last chapter was the conclusions of this study.

The integrated optical device used here may serve as a key component of integrated optical sensors, and can be produced at low cost. By directly attaching the light source and the detectors to the integrated optical device, a very compact sensing element will be obtained. Alternatively, optical fiber may be coupled to the input port of the device. In this case, the electronic and optoelectronic components can be placed at some distance from the actual sensor head.

The sensor can be used as low cost component of a distributed optical network of chemical sensors for monitoring presence of hazardous air pollutants in the exhaust of aircraft / spacecraft propulsion.

In this sensor, ammonia concentration below 2.4 % could not be detected by this sensor while the response and recovery times were in the range of 120 and 240 sec respectively.

By making use of larger numbers of dye molecules per unit volume of polymer will result in a stronger change in the refractive index and correspondingly in more phase change between the two light beams of MZI for the same concentration of ammonia and hence increase the sensitivity. The sensitivity of the sensor may further be improved by increasing the interaction length.

This sensor has a very important advantage, that this sensor can be used to detect different chemical gases by removing the sensitive material after measurements, and spin coating another material which can be used to detect another gas. Therefore, the device can be used again for other applications.

As a future work, more work is needed to enhance the sensor sensitivity and response.

Abbreviations

Ar	Argon
BCP	Bromocresol purple
BPM	Beam propagation method
CHF_3	Trifluoromethane
$C_2H_{16}Si$	Triethylsilane
$(C_2H_5)_4SiO_4$	Tetraethylorthosilicate
CVD	Chemical vapor deposition
DCS	Dichlorosilane
DI	De-ionized
EIM	Effective index method
Fe_2O_3	Iron oxide
FD-BPM	Finite difference beam propagation method
FE-BPM	Finite element beam propagation method
FET	Field-effect transistor
FFT-BPM	Fast Fourier transform beam propagation method
He-Ne	Helium-neon
H_2O_2	Hydrogen peroxide
H_3PO_4	Phosphoric acid
HNO_3	Nitric acid
IC	Integrated circuits
ID-BPM	Imaginary distance beam propagation method
InP	Indium phosphide
IO	Integrated optics
IO MZI	Integrated optical mach-zehnder interferometer
IPA	Isopropanol
ISFET	Ion sensitive field effect transistor
$LiNbO_3$	Litium niobate
LOCOS	Local-oxidation-of-silicon
LPCVD	Low pressure chemical vapor deposition
MIBK	Methylisobutyl ketone

MOSFET	Metal-oxide-semiconductor field-effect transistor
MZI	Mach-zehnder interferometer
NH_3	Ammonia
NH_4OH	Ammonium hydroxide
O_2	Oxygen
OIC	Optical integrated circuits
OLIVE	Oil-latching interfacial-tension variation effect
PECVD	Plasma enhanced chemical vapor deposition
PML	Perfect matched layer
PMMA	Polymethyl methacrylate
PMMA-BCP	Polymethyl methacrylate-bromocresol purple
RIE	Reactive ion etching
SAFET	Surface accessible field effect transistor
SAW	Surface acoustic wave
SGFET	Suspended gate field effect transistor
Si	Silicon
Si_3N_4	Silicon nitride
SiO_2	Silicon dioxide
SiON	Silicon oxynitride
SnO_2	Tin oxide
SOI	Silicon-on-insulator
TCR	Temperature coefficient of resistance
TE	Transverse electric
TEOS	Tetraethylorthosilicate
TES	Triethylsilane
TIR	Total internal reflection
TM	Transverse magnetic
TO	Thermal oxidation
UV	Ultraviolet

References

[1] G. T. Roman, "Process characterization of LPCVD silicon nitride and the consequential fabrication of low stress microcantilevers", CNF, Cornell University, 2003.

[2] http://www.timedomaincvd.com/CVD_Fundamentals/films/SiN_properties.html, 02.05.2007.

[3] http://galileo.phys.virginia.edu/outreach/8thgradesol/InternalReflectionFrm.htm, 20.03.2007.

[4] P. V. Lambeck, "Integrated optical sensors for the chemical domain", Meas. Sci. Technol. 17, PP. R93 – R116, 2006.

[5] http://www.monos.leidenuniv.nl/smo/index.html?basics/light.htm, 07.01.2007.

[6] R. Ulrich, "Theory of the prism–film coupler by plane wave analysis", J. Opt. Soc. Am., 1970.

[7] T. Tamir and S. T. Peng, "Analysis and design of grating couplers", Appl., Phys., Vol. 14, PP. 235 – 254, 1977.

[8] O. Mitomi, K. Kasaya and H. Miyazawa, "Design of a single–mode tapered waveguide for low loss chip–to–fiber coupling", IEEE, J. Quantum Electron, Vol. 30, PP. 1787 – 1793, 1994.

[9] W. Göpel and J. N. Zemel, "Sensors: A comprehensive survey in chemical and biochemical sensors", Weinheim, Germany: VCH-Verlagsgesellschaft, vol. 2/3, 1991.

[10] J. Janata, "Principles of chemical sensors", New York: Plenum, 1989.

[11] J. Janata, and R. J. Huber, "Solid state chemical sensors", San Diego, CA: Academic, 1985.

[12] A. Hierlemann, O. Brand, C. Hagleitner and H. Baltes, "Microfabrication techniques for chemical / biosensors", IEEE, Vol. 91, No. 6, PP. 839 – 863, June 2003.

[13] A. L. Spetz, "Chemical sensor technologies", S-SENCE / IFM, Linköping University, Sweden, 2006.

[14] R. P. H. Kooyman and L. M. Lechuga, "Immunosensors based on total internal reflectance", in handbook of biosensors and electronic noses, E. Kress-Rogers. Ed. Boca Raton, FL: CRC, 1997.

[15] P. V. Lambeck, "Sensors actuators", B 8, PP. 108 – 116, 1992.

[16] H. Porte, V. Gorel, S. Kiryenko, J. P. Goedgebuer, W. Daniau and P. Blind, "Imbalanced Mach-Zehnder Interferometer in micromachined silicon substrate for pressure sensor", Journal of Lightwave Technology, Vol. 17, No. 2, PP. 229 – 233, February 1999.

[17] F. Prieto, B. Sepulveda, A. Calle, A. Llobera, C. Dominguez, A. Abad, A. Montoya and L. M. Lechuga, "An integrated optical interferometeric nanodevice based on

silicon technology for biosensor applications", Nanotechnology 14, PP. 907 – 912, 2003.

[18] F. Prieto, L. M. Lechuga, A. Calle, A. Llobera, and C. Dominguez, "Optimized silicon antiresonant reflecting optical waveguides for sensing applications", Journal of Lightwave Technology, Vol. 19, No. 1, PP. 75 – 83, January 2001.

[19] P. Äyräs, S. Honkanen, K. M. Grace, K. Shrouf, P. Katila, M. Leppihalme, A. Tervonen, X. Yang, B. Swanson and N. P eyghambarian, "Thin film chemical sensors with waveguide Zeeman interferometery", Pure Appl., Opt. 7, PP. 1261 – 1271, 1998.

[20] J. F. McAleer, P. T. Moseley, J. O. Norris, and D. E. Williams, "Tin dioxide gas sensors", Journal Chem. Soc., Faraday Trans. I; Vol. 83, PP. 1323-1346, 1987.

[21] P. N. Bartlett, P. B. M. Archer and S. K. Ling-Chung, "Conducting polymer gas sensors, part 1: fabrication and characterization", Sensors and Actuators B, vol. 4, PP. 365-372, 1991.

[22] Y. Nakatani, M. Matsuoka and Y. Iida, "γ-Fe_2O_3 ceramic gas sensor", IEEE Trans. on Components, Hybrids and Manufacturing Tech., Vol. CHIMT-5, No. 4, December 1992.

[23] K. Ihokura and J. Watson, "The stannic oxide gas sensor: principles and applications", CRC Press: Ann Arbor, Michigan, PP. 2-7, 1994.

[24] P. Bergveld, "Development of an ion-sensitive solid-state device for neurophysiological measurements," IEEE Trans Biomedical Eng., Vol. 17, PP. 70-71, January 1970.

[25] K. I. Lundstrom, M. S. Shivaraman and C. M. Svenson, "A hydrogen-sensitive Pd gate MOS transistor", Journal App Physics, Vol. 46, No. 9, PP. 3876-3881, September 1975.

[26] M. Stenberg and B. Dahlenback, "Surface-accessible FET for gas Sensing", Sensors and Actuators, Vol. 4, PP. 273-281, 1983.

[27] M. Joseowics and J. Janata, "Suspended gate field effect transistor modified with polypyrrole as alcohol sensor", Anal Chem., Vol. 58, PP. 514-517, 1986.

[28] I. Lundstrom and C. Svensson, "Gas-sensitive metal gate semiconductor devices", Solid Sate Chemical Sensors, Jiri Jonata and Robert J. Huber, Eds, Academic Press: New York, PP. 2-50, 1985.

[29] H. D. Wiemhofer and W. Gopel, "Fundamentals and principles of potentiometric gas sensors based upon solid electrolytes", Sensors and Actuators B, Vol. 4, PP. 365-372, 1991.

[30] G. Hoetzel and W. Weppner, "Potentiometric gas sensors based on fast solid electrolytes", Sensors and Actuators, Vol. 12, PP. 449-453, 1987.

[31] J. Janata, "Principles of chemical sensors", Plenum Press: New York, Chapters 2, V3, and 5, 1989.

[32] C. Nylander, "Chemical and biological sensors", J. Phys. E: Sci. Instrum., Vol. 18, PP. 736 – 750, 1985.

[33] T. Koster and P. V. Lambeck, "An integrated optical platform for absorptive sensing of chemical concentrations using chemo-optical monolayers", J. Meas., Sci., Technol., PP. 1230 – 1238, 2002.

[34] J. Tschmelak, G. Proll and G. Gauglitz, "Optical biosensor for pharmaceuticals, antibiotics, hormones, endocrine disrupting chemicals and pesticides in water: assay optimization process for estrone as example", Talanta, Elsevier Science BV, PP. 313 – 323, 2005.

[35] K. Tiefenthaler and W. Lukosz, "Sensitivity of grating couplers as integrated-optical chemical sensors", J. Opt., Soc., Am., Vol. 6, No. 2, PP. 209 – 216, 1989.

[36] O. Parriaux and G. Veldhuis, "Normalized analysis for the sensitivity optimization of integrated optical evanescent wave sensors", J. Lightwave Technol., PP. 573 – 582, 1998.

[37] G. Veldhuis, O. Parriaux, H. J. W. M. Hoekstra and P. V. Lambeck, "Sensitivity enhancement in evanescent optical waveguides sensors", J. Lightwave Technol., PP. 677 – 682, 2000.

[38] J. V. Lith, "Novel integrated optical sensing platforms for chemical and immuno-sensing", PhD Thesis, Uni. of Twente, Enschede, The Netherlands, 2005.

[39] J. Comley, "Label-free detection; new biosensors facilitate broader range of drug discovery applications", Drug Discovery World winter, 2004.

[40] C. Malins, A. Doyle, B. Maccraith, F. Kvasnik, M. Landl, P. Simon, L. Kalvoda, R. Lukas, K. Pufler and I. Babusik, "Personal ammonia sensor for industrial environments", J. Environ. Monit., PP. 417 – 422, 1999.

[41] F. Ay, "Silicon oxynitride layers for applications in optical waveguides", Master Thesis, Bilkent Uni., September 2000.

[42] G. J. Valdhuis, "Bent-waveguide devices and mechano-optical switches", PhD thesis, Uni. of Twente, 1998.

[43] S. P. Pogossian, L. Vescan, and A. Vonsovici, "The single-mode condition for semiconductor rib waveguides with large cross section", Journal of Lightwave Technology, Vol. 16, No. 10, PP. 1851 – 1853, Oct. 1998.

[44] S. S. A. Obayya, B. M. Azizur, K. T. V. Grattan, and H. A. El-Mikati, "Full vectorial Finite-Element based imaginary distance beam propagation solution of complex modes in optical waveguides", Journal of Lightwave Technology, Vol. 20, No. 6, PP. 1054 – 1060, June 2002.

[45] J. Yamauchi, G. Takahashi, and H. Nakano, "Full-Vectorial beam propagation method based on the McKee-Mitchell scheme with improved finite difference formulas", Journal of Lightwave Technology, Vol. 16, No. 12, PP. 2458 – 2464, Dec. 1998.

[46] T. Fujisawa and M. Koshiba, "Full vector Finite-Element beam propagation method for three dimensional nonlinear optical waveguides", Journal of Lightwave Technology, Vol. 20, No. 10, PP. 1876 – 1884, Oct. 2002.

[47] J. Shibayama, T. Takahashi, J. Yamauchi, and H. Nakano, "Efficient time domain finite difference beam propagation methods for the analysis of slab and circularly symmetric waveguides", Journal of Lightwave Technology, Vol. 18, No. 3, PP. 675 – 687, March 2000.

[48] Y. Tsuji, M. Koshiba, and N. Takimoto, "Finite Element beam propagation method for anisotropic optical waveguides", Journal of Lightwave Technology, Vol. 17, No. 4, PP. 723 – 728, April 1999.

[49] Y. Tsuji and M. Koshiba, "Guided-Mode and Leaky-Mode Analysis by Imaginary Distance Beam Propagation Method Based on Finite Element Scheme", Journal of Lightwave Technology, Vol. 18, No. 4, PP. 618 – 623, 2000.

[50] O. Parriaux and P. Dierauer, "Normalized expressions for the optical sensitivity of evanescent wave sensors: erratum", Optics Letters, Vol. 19, No. 20, PP. 508 – 510, 1994.

[51] http://www.imm.cnm.csic.es/biosensores/mzi.htm, 23.04.2007.

[52] O. Parriaux, "Fiber optic chemical sensors and biosensors", Italy, O. Wolfbeis, Ed. (CRC, Boca Raton), Vol. 1, PP. 111-192, 1991.

[53] W. Lukosz, "Integrated optical nanomchanical devices as modulators, switches and tunable wavelength filters as acoustical sensors", Proc., SPIE, Vol. 3, PP. 402 - 406, 1992.

[54] J. Angel-Valenzuela, A. Sanchez, R. Cardoso, L. Villegas-Vicencio, D. Salazar and H. Marquez, "A fabry-perot-type integrated optical temperature transducer", Instrumentation and Development, Vol. 5, No. 3, PP. 184 – 189, 2001.

[55] E. Camargo, H. Chong and R. Rue, "2D photonic crystal thermo-optic switch based on AlGaAs/GaAs epitaxial structure", Optics Express, Vol. 12, No. 4, PP. 588 – 592, 2004.

[56] T. Aalto, M. Kapulainen, S. Yliniemi, P. Heimala and M. Leppihalme, "Fast thermo-optical switch based on SOI waveguides", Integrated Optics, Vol. 4987, PP. 149 – 159, 2003.

[57] http://ece-www.colorado.edu/~bart/book/ellipsom.htm, 01.05.2007.

[58] S. Sarkisov, D. Diggs, G. Adamovsky and M. Curley, "Single-arm double-mode double-order planar waveguide interferometric sensor", Applied Optics, Vol. 40, No. 3, PP. 349 – 359, 2001.

[59] C. Wu, P. Lin, R. Huang, W. Chao and M. Lee, "Design optimization for micromachined low power Mach-Zehnder thermo-optic switch", Applied Physics Letters 89, 121121, 2006.

[60] G. Treyz, "Silicon Mach-Zehnder waveguide interferometer operating at 1.3 μm", Electron. Lett. 27, 118-120, 1991.

List of Figures

List of tables